ATOMIC SCALE CONTROL OF SEMICONDUCTOR SURFACES FROM SOLUTION

A Dissertaion
Presented to the Faculty of the Graduate School
of Cornell University
in Partial Fulfillment of the Requirements for the Degree of
Doctor of Philosophy

by
Erik Steven Skibinski
December 2017

ATOMIC SCALE CONTROL OF SEMICONDUCTOR SURFACES FROM SOLUTION

Erik Steven Skibinski, Ph. D.

Cornell University 2017

The fundamental surface chemistry of semiconductors in ambient environments is important to many applications of semiconductor materials, yet is poorly understood. Developing an understanding of how to control semiconductor surfaces using solution-based methods is critical, both as a method to rationally control surface structure, and as a means to study surface reactions at the molecular scale in the ambient conditions relevant to applications. This dissertation shows that both silicon and metal oxide semiconductors can be controlled and studied at the atomic scale using solution-based methods. In this work, scanning tunneling microscopy (STM) was used to investigate the structure of semiconductor surfaces, surface spectroscopy was used to study the chemical composition and orientation of adsorbed molecules, and computer simulations and calculations were used to verify and provide insight into experimental results.

Using these methods, the solution-deposition of a nearly perfect organic monolayer of benzoate on atomically flat rutile (110) TiO_2 was studied. The phenyl rings of benzoate molecules on rutile (110) were found to adopt an unexpected tetrameric structure as a result of π-π interactions, resolving a controversy surrounding the bonding geometry of benzoate molecules on this surface.

In addition, the photoreactivity of TiO_2 was studied using solution-deposited monolayers of benzoate and phenylphosphinate on anatase (001) and rutile (110). The photodecomposition kinetics of these monolayers in air was monitored with *in-situ* infrared spectroscopy, and the structures of the reacted surfaces were investigated with *ex-situ* STM. In all cases studied, the photoreaction kinetics followed unusual biexponential kinetics, in which the photodecomposition rate decreases by approximately two orders of magnitude after a fraction (typically ~25%) of the molecules have reacted. This trend in reactivity is proposed to result from changes in the magnitude of band bending at the surface.

Lastly, two solution-based methods for the functionalization of Si (111) surfaces were investigated with STM, surface spectroscopy, and kinetic Monte Carlo simulations. It was found that a methoxylation process unexpectedly etches the silicon surface, and a new direct method for the fluorination of Si (111) using HF(aq) was discovered.

BIOGRAPHICAL SKETCH

Erik Skibinski was born in Schenectady, NY where he attended high school at Scotia-Glenville High School. He continued on to The State University of New York at Geneseo, where he obtained his B. S. in Chemistry, and performed research studying the cause of fluorescence intermittence in CdSe nanocrystals with Professor Jeffrey Peterson. After finishing his undergraduate studies, he went on to attend graduate school at Cornell University, where he studied the surface chemistry of semiconductors under the guidance of Professor Melissa A. Hines.

ACKNOWLEDGMENTS

I would first like to thank my advisor Professor Melissa A. Hines for her guidance, patience, insight, and inspiration. I have learned a great deal from her beyond chemical research in a wide array of topics, ranging from oral communication, programming, to machining.

Research in the Hines lab wouldn't have been the same without my comrades: Will, Anqi, DJ, Ashley, and Sara. Thank you for providing a fun and collaborative atmosphere, and for keeping the Hines lab weird.

I would also like to thank my family, Clarissa, and Pumba for their constant support and encouragement.

Finally, I would like to thank Hobbes for her insightful contributions to every group meeting.

Table of Contents

Chapter 1

Introduction

Semiconductor materials are used in a wide range of vital technologies. For example, silicon is essential to both the microelectronics and photovoltaics industries, whereas semiconducting metal oxides are used in dye-sensitized solar cells[1] and show promise in upcoming technologies such as carbon dioxide photoreduction[2] or photocatalytic environmental remediation.[3] A common aspect of these technologies is that they require precise control of the chemical composition or physical structure at the surface of the semiconducting material. The importance of surface control can be observed in the electronic properties of silicon devices, where increasing the roughness of the starting wafer from 2 to 10 Å RMS decreases channel mobility by a factor of four.[4] It can also be seen in the photocatalytic performance of TiO_2 nanocrystals, where changing the dominant exposed crystal face results in a ~375% increase in reactivity.[5] From both technological and scientific perspectives, it is desirable to obtain well-controlled surfaces using solution-phase chemistry. Despite their importance, the fundamental reactions necessary for the control of semiconductor surfaces from solution and the reactions that occur on their surface during application are poorly understood. As such, developing an understanding of how to control semiconductor surfaces from solution is critical, both as a method to rationally tailor chemical composition and structure but also as means to study fundamental surface reactions in technologically relevant conditions.

Instead of in solution, the vast majority of fundamental surface research comes from samples prepared in ultra-high vacuum (UHV). One way of producing highly controlled surfaces in UHV is to bombard them with energetic ions to remove contamination, then to anneal the sample at high temperature to flatten the surface. A well-controlled rutile TiO_2 prepared with this sputter-and-anneal method is shown in the scanning tunneling microscopy (STM) image of Figure 1.1(a). In this image, the surface is composed of atomically flat terraces, and the lines running along the surface are rows of individual undersaturated Ti

atoms. Another method employed to prepare materials for study is to directly grow them inside of an ultra-high vacuum chamber, such as in molecular-beam epitaxy.

UHV-Prepared Rutile   Solution-Etched Rutile
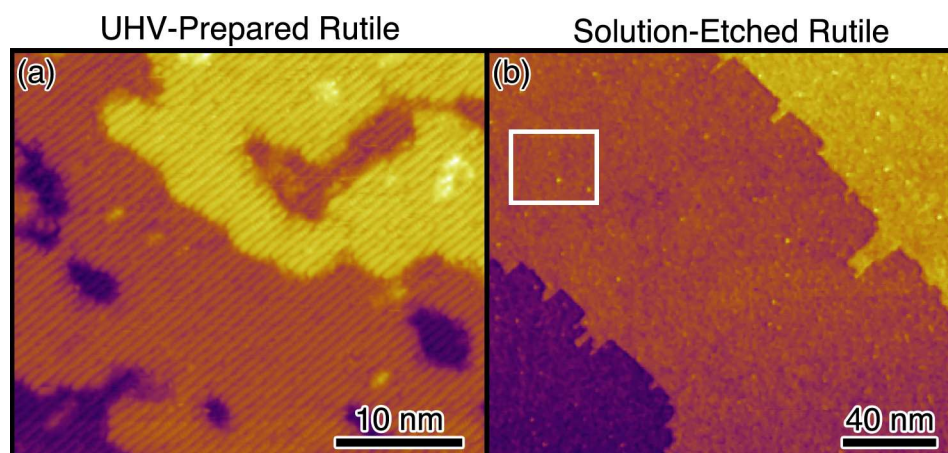
Figure 1.1(a) Scanning tunneling microscopy image of rutile (110) TiO_2 prepared through sputtering and annealing in an ultra-high vacuum chamber. (b) Rutile (110) prepared using an aqueous etchant. White rectangle is the size of STM image in (a).

Although these techniques are used to prepare the samples used in the vast majority of surface science studies and provide valuable fundamental insight, there are a number of associated drawbacks. One problem is that these ultra-high vacuum methods often result in the production of surface defect species. In the case of TiO_2, these occur in the form of highly reactive sputter induced Ti^{3+} sites composing 5 - 10% of the surface. These species are so reactive that they often dominate the observed reactivity of the material in ultra-high vacuum, yet do not survive upon exposure to air.[6] As such, they have little relevance to the properties of TiO_2 in actual applications. Another drawback is that ultra-high vacuum equipment is very expensive and can be cost-prohibitive as a production method in application.

An attractive alternative method of producing highly controlled semiconductor surfaces is to prepare them using solution-phase chemistry, such as etching, deposition, or hydrothermal growth. This approach is desirable from a technological perspective, as it is often simpler and more cost-effective than UHV methods. From a scientific perspective, solution-based methods provide an ideal opportunity to study the fundamentals of surface reactivity in ambient conditions at the atomic scale. The exquisite degree of control that can be obtained using solution-phase etching of TiO_2 is shown in Figure 1.1(b). This STM

image shows atomically flat terraces over large length scales separated by faceted, straight steps. In fact, this etched surface is even flatter over larger length scales than the surface prepared using UHV methods. Importantly, spectroscopic analysis of this etched surface shows that it is free of any reactive Ti^{3+} defect sites that would normally be present as a result of preparation in UHV.

If solution-based methods are so effective, why are they not more commonly employed in surface studies? One barrier is that there is a general perception that solution-based methods yield surfaces that are too contaminated for use with surface science techniques, such as scanning tunneling microscopy. This dissertation shows that both metal oxide semiconductors and silicon can be precisely controlled at the atomic scale using solution-based methods and that these surfaces are compatible with the techniques of surface science. By taking this approach, the surface reactivity of semiconductors can be probed under technologically relevant conditions, providing rational insight into the improvement of technologies.

One way of controlling the structure of a surface is through the formation of a self-assembled monolayer (SAM). Self-assembled monolayers are directly relevant to applications of metal oxides such as dye-sensitized solar cells[7] and organic field effect transistors.[8] Additionally, they are of fundamental scientific value as a highly controllable method for studying the interaction of molecules with surfaces. Chapter 3 describes the formation of nearly ideal SAMs of benzoate, a molecular analogue for dye molecules used in dye-sensitized solar cells, on atomically flat rutile TiO_2 prepared entirely through solution-based methods. The uniformity of these solution-prepared monolayers can be seen in Figure 1.2(a), where each small protrusion in the image is the top of an individual benzoate molecule. A combination of STM, polarized spectroscopy, and computer simulation reveal an unexpected manifestation of π-π interactions, which results in a tetrameric arrangement of benzoate molecules on the surface. This discovery resolves a controversy over the favorable structure of benzoate on rutile[9,10] and may have implications for the design of molecules used in dye-sensitized solar cells.

Solution-Prepared Monolayer   ...after 6 Minutes UV
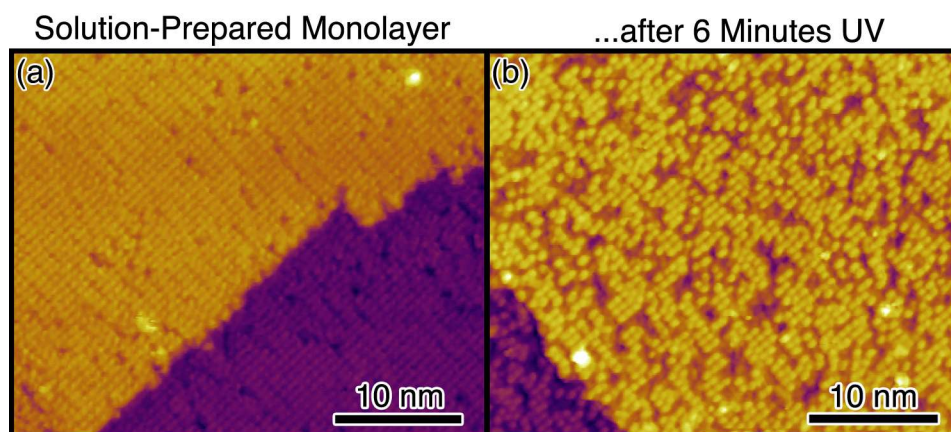
Figure 1.2 (a) Scanning tunneling microscope image of a benzoate monolayer on rutile (110) TiO_2 prepared entirely in solution. (b) An equivalently prepared benzoate monolayer after 6 min of UV irradiation in an oxygen atmosphere. A fraction of the benzoate molecules are missing as a result of photoreaction.

In addition to providing a method of controlling surface structure at the atomic scale, SAMs on metal oxides are an ideal platform for studying the photoreactivity of these materials in ambient conditions. Photocatalytic reactions on metal oxides show promise in several high profile applications such as carbon dioxide photoreduction,[2] water splitting,[11] or photodegradation of pollutants.[3] Unfortunately, these exciting technologies are not yet efficient enough for widespread use. One significant barrier to their improvement is that the fundamental reactions that occur on their surface in application are largely unknown.

Chapter 4 describes how organic SAMs on metal oxide surfaces can be used to study the photoreactivity of metal oxides at the molecular scale in ambient conditions. High quality organic monolayers are prepared in solution on both important phases of TiO_2, rutile and anatase, then exposed to UV light in either air or a pure oxygen environment. The above-bandgap radiation generates reactive electron-hole pairs, which initiate the photodecomposition of the molecules adsorbed to the surface. These reactions are monitored with either *in-situ* infrared spectroscopy or *ex-situ* STM and x-ray photoelectron spectroscopy of the reacted surface.

In all cases studied, the photodecomposition reaction displays highly unusual kinetics, in which over the first few minutes of irradiation the reactivity of the surface drops by approximately two orders of

magnitude. This behavior is seen on both rutile and anatase TiO_2 across many types of organic monolayers. Scanning tunneling microscopy of the reacted surface shows that this is not a result of heterogeneity, whereas statistical analysis of photoreacted benzoate monolayers, such as shown in Figure 1.2(b), shows that the reaction is occurring randomly across the surface.

This trend in reactivity is proposed to result from photoinduced changes in the magnitude of band bending. Upward band bending present in the initial phase of the reaction aids in charge separation and migration of reactive holes to the surface.[12] After reaction, the magnitude of the upward band bending decreases, and thus the rate of reaction decreases due to the reduce hole flux to the surface. If the exact mechanism of this seemingly ubiquitous effect can be determined, it may be possible to prevent it and thus dramatically increase the reactivity of metal oxide photocatalysts.
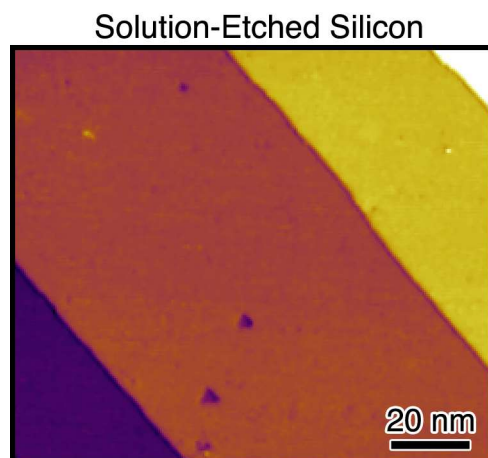
Figure 1.3 Scanning tunneling microscope image of atomically flat hydrogen-terminated silicon (111) after etching in NH_4F(aq).

In addition to metal oxide semiconductors, there are exciting technologies that require precise chemical functionalization of silicon surfaces. Approximately 30 years ago, it was discovered that silicon (111) etched in NH_4F(aq) produced a nearly perfect surface, both from a structural[13] and electronic[14] point of view. The structural perfection of this hydrogen-terminated etched silicon surface is shown in the scanning tunneling microscope image of Figure 1.3, which displays atomically flat terraces separated by

straight steps. Despite intensive research, efforts to integrate further functionality, such as biological or chemical sensitivity to this desirable surface, have largely been stymied.

The problem is that in order to maintain the electronic quality of the surface, oxidation of the silicon substrate must be strictly avoided both during functionalization and afterwards. As a result of this restriction, there are only two established methods for functionalizing hydrogen-terminated silicon,[15,16] which are prohibitively limited in their scope of surface terminations that can be produced.

Ideally, a fraction of the hydrogen-terminated surface would be replaced with a functional group that allows further reactions, such as a hydroxyl group. This would allow the integration of functionalization reactions developed for silica or glass with the desirable properties of flat silicon (111).

Michalak *et al*. recently achieved a breakthrough towards this goal,[17] in which a hydrogen-terminated silicon (111) surface was partially hydroxylated without concomitant oxidation of the underlying silicon. This was accomplished through a solution-phase preparation consisting of sequential methoxylation, fluorination, then hydroxylation of the surface. While successful, this reaction was studied only with spectroscopic methods. As such, the structural evolution of the surface during these steps was unknown.

Chapter 5 describes how during the course of investigating the mechanism of these reactions several unexpected discoveries were made. First, it was found that the methoxylation reaction unexpectedly resulted in slight etching of the surface. Even more surprisingly, the hydrogen-terminated surface can be directly fluorinated through an immersion in HF(aq). This provides an alternate method of producing hydroxylated silicon (111) free of the surface roughening induced during methoxylation.

In summary, this thesis demonstrates that semiconductor surfaces, including metal oxides, can be controlled and studied at the atomic scale using solution-based methods. This represents a step forward towards the goal of understanding the surface reactivity of these important materials in the conditions where they are actually applied and the rational design of surface structure through solution-based methods.

[1] O'Regan, B.; Grätzel, M. A Low-Cost, High-Efficiency Solar Cell Based on Dye-Sensitized Colloidal TiO$_2$ Films. *Nature* **1991**, *353* (6346), 737–740.

[2] Chanmanee, W.; Islam, M. F.; Dennis, B. H.; MacDonnell, F. M. Solar Photothermochemical Alkane Reverse Combustion. *PNAS* **2016**, *113* (10), 2579–2584.

[3] Hoffmann, M. R.; Martin, S. T.; Choi, W.; Bahnemann, D. W. Environmental Applications of Semiconductor Photocatalysis. *Chemical Reviews* **1995**, *95* (1), 69–96.

[4] Ohmi, T.; Kotani, K.; Teramoto, A.; Miyashita, M. Dependence of Electron Channel Mobility on Si-SiO$_2$ Interface Microroughness. *IEEE Electron Device Letters* **1991**, *12* (12), 652–654.

[5] Gordon, T. R.; Cargnello, M.; Paik, T.; Mangolini, F.; Weber, R. T.; Fornasiero, P.; Murray, C. B. Nonaqueous Synthesis of TiO$_2$ Nanocrystals Using TiF$_4$ to Engineer Morphology, Oxygen Vacancy Concentration, and Photocatalytic Activity. *Journal of the American Chemical Society* **2012**, *134* (15), 6751–6761.

[6] Diebold, U. The Surface Science of Titanium Dioxide. *Surface Science Reports* **2003**, *48* (5), 53–229.

[7] Bae, E.; Choi, W.; Park, J.; Shin, H. S.; Kim, S. B.; Lee, J. S. Effects of Surface Anchoring Groups (Carboxylate vs. Phosphonate) in Ruthenium-Complex-Sensitized TiO$_2$ on Visible Light Reactivity in Aqueous Suspensions. *J. Phys. Chem. B* **2004**, *108* (37), 14093–14101.

[8] Wöbkenberg, P. H.; Ball, J.; Kooistra, F. B.; Hummelen, J. C.; de Leeuw, D. M.; Bradley, D. D. C.; Anthopoulos, T. D. Low-Voltage Organic Transistors Based on Solution Processed Semiconductors and Self-Assembled Monolayer Gate Dielectrics. *Appl. Phys. Lett.* **2008**, *93* (1), 13303.

[9] Grinter, D. C.; Nickels, P.; Woolcot, T.; Basahel, S. N.; Obaid, A. Y.; Al-Ghamdi, A. A.; El-Mossalamy, E.-S. H.; Alyoubi, A. O.; Thornton, G. Binding of a Benzoate Dye-Molecule Analogue to Rutile Titanium Dioxide Surfaces. *The Journal of Physical Chemistry C* **2012**, *116* (1), 1020–1026.

[10] Guo, Q.; Cocks, I.; Williams, E. M. The Adsorption of Benzoic Acid on a TiO$_2$(110) Surface Studied Using STM, ESDIAD, and LEED. *Surface Science* **1997**, *393* (1), 1–11.

[11] Fujishima, A.; Honda, K. Electrochemical Photolysis of Water at a Semiconductor Electrode. *Nature* **1972**, *238* (5358), 37–38.

[12] Zhang, Z.; Yates, J. T. Band Bending in Semiconductors: Chemical and Physical Consequences at Surfaces and Interfaces. *Chem. Rev.* **2012**, *112* (10), 5520–5551.

[13] Higashi, G. S.; Chabal, Y. J.; Trucks, G. W.; Raghavachari, K. Ideal Hydrogen Termination of the Si (111) Surface. *Appl. Phys. Lett.* **1990**, *56* (7), 656–658.

[14] Yablonovitch, E.; Allara, D. L.; Chang, C. C.; Gmitter, T.; Bright, T. B. Unusually Low Surface-Recombination Velocity on Silicon and Germanium Surfaces. *Physical review letters* **1986**, *57* (2), 249.

[15] Linford, M. R.; Fenter, P.; Eisenberger, P. M.; Chidsey, C. E. D. Alkyl Monolayers on Silicon Prepared from 1-Alkenes and Hydrogen-Terminated Silicon. *J. Am. Chem. Soc.* **1995**, *117* (11), 3145–3155.

[16] Bansal, A.; Li, X.; Lauermann, I.; Lewis, N. S.; Yi, S. I.; Weinberg, W. H. Alkylation of Si Surfaces Using a Two-Step Halogenation/Grignard Route. *J. Am. Chem. Soc.* **1996**, *118* (30), 7225–7226.

[17] Michalak, D. J.; Amy, S. R.; Aureau, D.; Dai, M.; Estève, A.; Chabal, Y. J. Nanopatterning Si(111) Surfaces as a Selective Surface-Chemistry Route. Nature Materials 2010, 9 (3), 266–271.

Chapter 2

Experimental Methods

2.1 Tip preparation

Tungsten wire used to make scanning tunneling microscopy (STM) tips was thermally recrystallized prior to etching. This process improves the shape of the resulting tip, leading to better performance in STM.[1] A nominally 10 cm length of tungsten wire (0.125 mm, 99.95%, Goodfellow) was attached to two copper electrode feedthroughs by being clamped between two washers on each end as shown in Figure 2.1. The feedthrough flange with the wire attached was then mounted to a small vacuum chamber equipped with a turbo pump and ion gauge. Once the pressure in the chamber was below 10^{-5} mbar, the feedthrough terminals were attached to a power supply (TDK Lambda) operating in constant current mode, and the current was slowly ramped up to 3.05 A. This current was maintained for 30 min or until the wire broke (typically in ~25 min). Upon removal from the chamber, the two ends of the wire within 1.3 cm of the clamps were discarded, as they may not have reached the necessary temperature for recrystallization.
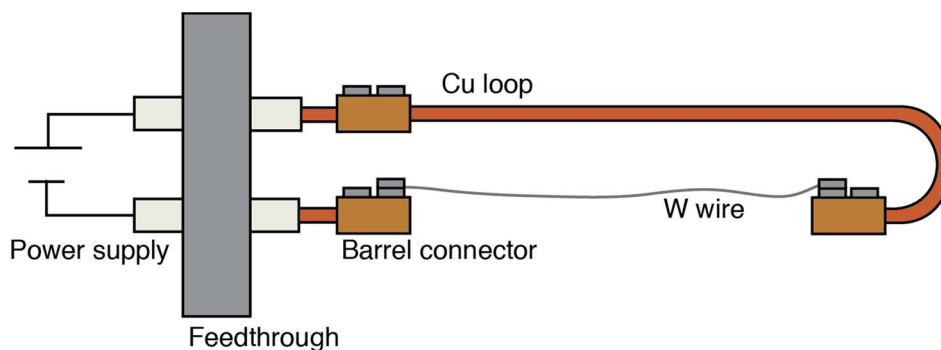
Figure 2.1: Apparatus for annealing tungsten wire. Not to scale

Recrystallized tungsten was electrochemically etched in KOH(aq) to obtain a sharp apex suitable for use in STM. The desired narrow structure is thought to form along the wire near the air/solution interface as a result of slower diffusion of OH^- into the meniscus and shielding of the wire by falling etch products. Eventually, the narrow region became too weak to support the hanging length of wire, which broke off, leaving an extremely sharp tip.[2]

To etch tips, a section of wire was crimped to provide spring force within the tip collet, then securely inserted into a tip carrier with approximately 1.7 mm protruding from the front. This length was empirically determined to consistently provide high quality tips. The leg of the tip carrier in electrical contact with the tungsten wire was attached to an alligator clip, and then half of the tungsten wire was inserted into a 2 M aqueous solution of KOH containing a circular Pt electrode as shown in Figure 2.2. A constant voltage of +2 V was applied between the tip carrier and Pt electrode, resulting in the electrochemical etching of the wire. To prevent over-etching of the tip, the differential current was monitored, and when it exceeded 64 mV (corresponding to tip drop-off) the bias on the tip was switched to -8.5 V to prevent spontaneous etching.[3]
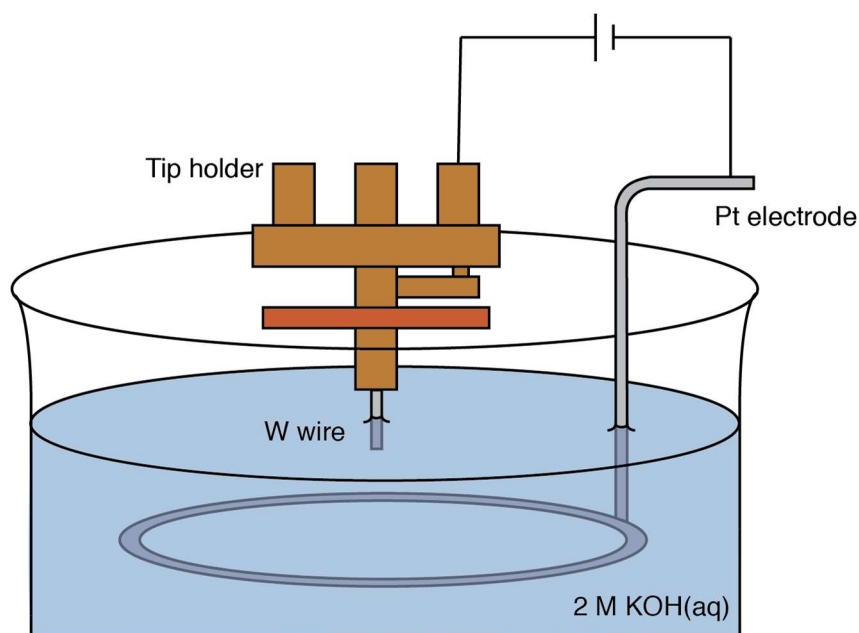
Figure 2.2: Setup for electrochemical etching of tungsten wire to make STM tips.

Etched tips were inspected with an optical microscope to insure that the apex was sharper than can be resolved optically. Acceptably sharp tips were cleaned by immersion in H_2O to remove KOH, then degreased by sequential immersion in trichloroethylene, acetone, and methanol, then rinsed in flowing H_2O.

Cleaned tips were then loaded into ultrahigh vacuum through an oil-free, turbomolecular-pumped load lock. To remove the native oxide and any surface contamination, tips were heated by electron

bombardment to a temperature >1000 °C. The tip was approached to a thoriated tungsten filament within a Wehnelt cone as show in Figure 2.3. Typically, the tip was biased at +1000 V and the filament current slowly increased until 1.2 mA of emission current was measured between the filament and tip for a period of 5 s.
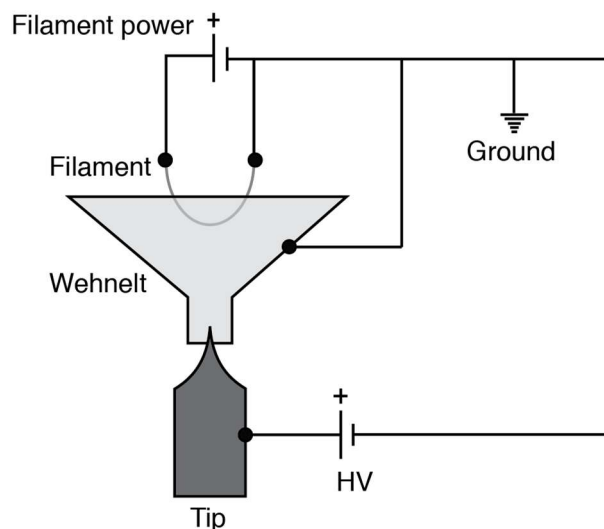
Figure 2.3 Schematic of tip flashing apparatus.

Tips were then tested for performance in STM on clean samples. If images of acceptable quality could be obtained, tips were then sometimes further conditioned by field-directed sputter sharpening.[4] This process cleans and sharpens the tip by bombardment with energetic Ar^+ ions normal to the apex of the tip. Blunting of the tip is mitigated by applying a positive bias to the tungsten tip during sputtering. The local electric field enhancement at the apex reduces the ion flux impacting the surface.

To perform field-directed sputter sharpening, tips were loaded into a specially modified tip carrier that allows the tip to be oriented in the correct direction and be biased. This special tip carrier is shown in Figure 2.4. An additional base plate was machined from a spare sample plate and spot-welded to the bottom plate of the tip carrier. This allows the tip carrier to be transported on a manipulator with the tip facing outward. The asymmetric cutout of this plate was chosen to allow proper clearance of wires on the STM piezo. Additionally, a stainless steel wire was spot-welded to the tip carrier so that it contacts the

loaded tip holder as shown in Figure 2.4. This provides the electrical connection for biasing the tip during sputtering, which would otherwise be electrically isolated.
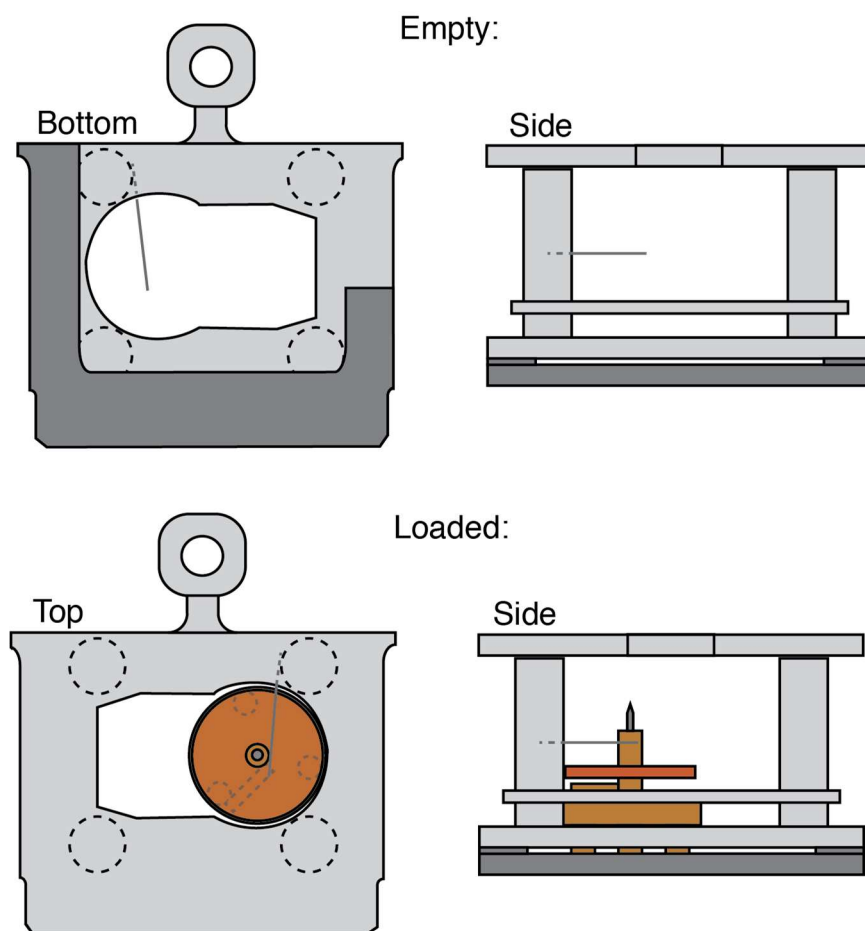
Figure 2.4: Schematic of sputtering tip carrier, both with and without a tip holder loaded. The additional plate, which allows the tip to be loaded upright and enter the manipulator is shown in dark grey.

Once loaded, tips were sputtered with a standard set of conditions. The ion pump was turned off and the main gate valve opened to allow turbomolecular pumping of the main chamber. A leak valve was used to fill the chamber to 5.5×10^{-5} mB of Ar, and the tip was positioned such that the tip apex was facing the sputter gun. Sputtering was performed with an accelerating voltage of 1.5 kV and a +150 V shielding bias applied to the tip for a period of 40 min, with a typical sputter current of ~2 μA.

Sputtering of tips can result in unintentional metal deposition on insulating materials of the tip holders, effectively grounding the tip. When this occurs, the auto-approach process will immediately stop upon

startup because the setpoint current will be detected flowing to the ground fault, instead of tunneling to the sample as intended.

To prevent this, tip holders were modified by the addition of Cu sputter shields as shown in Figure 2.5. These discs were machined from oxygen free copper, with a diameter of 5.61 mm and nominal thickness of 0.65 nm. Shields were attached to the stem of the tip holder with UHV-compatible solder, being careful to avoid the formation of any inadvertent electrical connections between the stem and body of the tip holder.
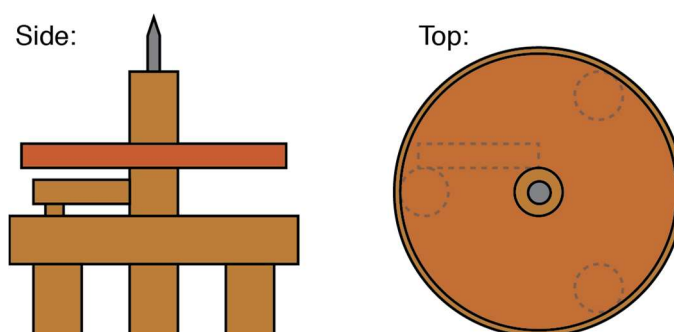
Figure 2.5: Tip holder with copper sputter shield attached.

The tip carrier for sputtering was aligned with the sputter gun by visually observing the removal of a colored tantalum oxide film attached to an equivalent tip carrier. A uniformly colored tantalum oxide film was electrochemically prepared by immersing two clean sheets of tantalum in a ~0.5 M aqueous solution of KH_2PO_4 and applying 25 VDC to the tantalum sheets for several seconds to yield a dark purple color at the anode. The oxidized sheet was then spot welded to a spare tip carrier, degreased, and loaded into UHV. Sputtering was performed on the tantalum oxide film at 1.5 keV until a region of the film was visibly removed as shown in Figure 2.6. If the ions were not incident at the correct location, positional adjustments were made until the sputtered region corresponded to the where the tip would be in a loaded tip carrier.

Figure 2.6: Example of a sputtered tantalum oxide film attached to a tip carrier used to align the sputter gun with the location of a tip.

2.2 Reflection Infrared Spectroscopy

The chemical composition and orientation of molecular adsorbates on TiO_2 surfaces were probed with reflection infrared spectroscopy. In comparison to multiple-internal-reflection infrared spectroscopy, reflection has less sensitivity, but is capable of detecting modes within the full range of the detector (650 – 4,000 cm^{-1}). In contrast, multiple internal reflection spectroscopy of TiO_2 is limited to modes above ~2,000 cm^{-1} by the multiphonon absorption of the substrate below this energy.

Reflection infrared spectroscopy samples were mounted such that the infrared beam was incident on the surface at an angle of 80° as shown in Figure 2.7. The infrared beam reflected off a gold mirror, the surface of the sample, then a final gold mirror before passing through a ZnSe wire grid polarizer and reaching a mercury-cadmium-telluride detector.
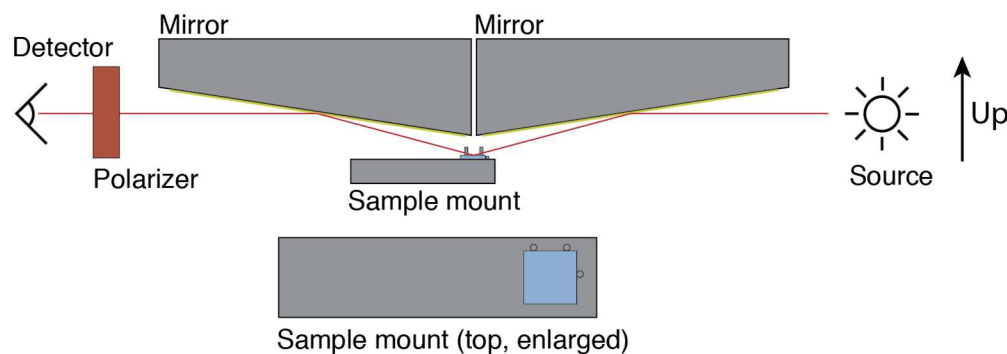
Figure 2.7: Schematic of reflection infrared spectroscopy setup. Sample crystal is shown in blue and the path of infrared beam shown in red.

An essential aspect of obtaining reflection infrared spectra on metal oxide samples was the reproducible alignment of the sample. The crystal must be replaced in the same orientation, and as close as possible to the exact position between each removal for chemical processing. Additionally, the sample must be free of any strain, such as from clips holding it in place. On the sample mount there were three protruding dowel pins, which allowed highly consistent, strain-free sample placement, even on crystals that are not perfectly square. The dowel pin in the plane of incidence protruded from the sample mount less than the typical crystal height (0.5 mm) to prevent shadowing the sample.

Additionally, it was important to minimize reflections off any surfaces of the sample mount other than the crystal. To reduce reflectivity of the sample mount, the surface was sandblasted and any surface area not occupied by sample or necessary for sample exchange was covered with black duct tape.

The interpretation of reflection infrared spectroscopy is not always straightforward, as the relative orientation of the transition dipole of the mode and the electric field of incident light can result in the formation of both positive and negative absorbances. Absorbance here is defined as $A \equiv \log(R_0/R)$ where R and R_0 are the reflected intensities with and without the presence of an absorbing species, respectively. Essentially, the molecules on the surface can act as either a reflective or anti-reflective coating.[5] The calculated sign of absorbance for adsorbates on rutile TiO_2 probed with polarized infrared light is shown in Figure 2.8(b). Here the adsorbates are assumed to have dynamic dipoles aligned along the x, y, or z directions as defined by the crystal, with z normal to the surface. At the 80° angle of incidence used in

experiment, modes along the *z* direction probed with *p*-polarized light yield negative absorbances, whereas modes parallel to the surface probed with *p*-polarized light (*x*) yield positive absorbances. Modes in the plane of the surface probed with *s*-polarized light (*y*) yield negative absorbances. The expected sign of absorbance must be carefully considered while interpreting reflection infrared spectra.
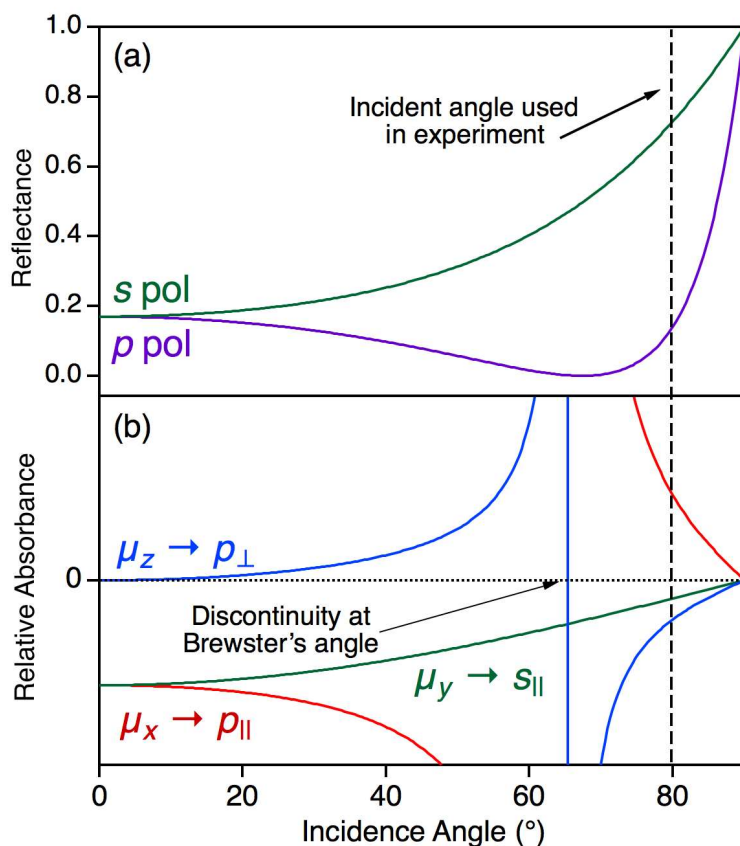
Figure 2.8: (a) The normalized reflectivity of rutile TiO_2 in *s*- and *p*- polarization as a function of incident angle. (b) The relative absorbance of infrared modes aligned along the *x*, *y*, or *z* directions probed with *s*- and *p*-polarized infrared light.

It may appear that the sensitivity of reflection infrared spectroscopy is maximized near Brewster's angle, yet this effect is balanced by the low reflectivity of the surface as shown in Figure 2.8(a).

---

[1] Greiner, M.; Kruse, P. Recrystallization of Tungsten Wire for Fabrication of Sharp and Stable Nanoprobe and Field-Emitter Tips. *Rev. Sci. Instrum.* **2007**, 78, 026104.

[2] Ibe, J. P.; Bey, P. P.; Brandow, S. L.; Brizzolara, R. A.; Burnham, N. A.; DiLella, D. P.; Lee, K. P.; Marrian, C. R. K.; Colton, R. J. On the Electrochemical Etching of Tips for Scanning Tunneling Microscopy. *Journal of Vacuum Science & Technology A: Vacuum, Surfaces, and Films* **1990**, *8* (4), 3570–3575.

[3] Guise, O. L.; Ahner, J. W.; Jung, M.-C.; Goughnour, P. C.; Yates, J. T. Reproducible Electrochemical Etching of Tungsten Probe Tips. *Nano Lett.* **2002**, *2* (3), 191–193.

[4] Schmucker, S. W.; Kumar, N.; Abelson, J. R.; Daly, S. R.; Girolami, G. S.; Bischof, M. R.; Jaeger, D. L.; Reidy, R. F.; Gorman, B. P.; Alexander, J.; *et al*. Field-Directed Sputter Sharpening for Tailored Probe Materials and Atomic-Scale Lithography. *Nat. Commun*. **2012**, 3, 935.

[5] Mielczarski, J. A.; Yoon, R. H. Fourier Transform Infrared External Reflection Study of Molecular Orientation in Spontaneously Adsorbed Layers on Low-Absorption Substrates. *J. Phys. Chem.* **1989**, *93*, 2034-2038.

Chapter 3

Solution Deposition of Self-Assembled Benzoate Monolayers on Rutile (110): Effect of π–π Interactions on Monolayer Structure[*]

Erik S. Skibinski, Anqi Song, William J. I. DeBenedetti, Amnon G. Ortoll-Bloch, and Melissa A. Hines*

Dept. of Chemistry and Chemical Biology, Cornell University, Ithaca NY 14853 USA

3.1 Abstract

High-quality, self-assembled benzoate monolayers were synthesized on rutile (110) using simple aqueous reactions. Sputtering and annealing cycles, which create surface and subsurface defects, were not needed. The monolayers were hydrophobic and remained largely contaminant free during exposures to laboratory air for tens of minutes. During this period, infrared spectroscopy showed that the monolayers did not spontaneously adsorb air-born hydrocarbons or other adventitious aliphatic species. Scanning tunneling microscopy (STM) images, infrared and x-ray photoemission spectra, Monte Carlo simulations, and *ab initio* calculations were all consistent with benzoate molecules adopting an edge-to-face ring geometry with their four nearest neighbors — a tetrameric bonding geometry. This bonding is further stabilized by a pairing interaction between adjacent benzoate molecules, a pairing that has previously been interpreted as dimerization. The coexistence of paired and unpaired regions of the monolayer is consistent with the relatively small additional energy gained by pairing and the cooperative nature of the pairing interaction. Monolayer stability is driven both by the strong bidentate bonding to unsaturated Ti atoms on the surface as well as by π-π interactions between adsorbates.

3.2 Introduction

The spontaneous formation of self-assembled monolayers from dilute solutions is of both scientific and technological importance. From a technological perspective, organic and inorganic molecules are often used to impart new functionality to a system. For example, the attachment of dye molecules with isonicotinic-acid-derived binding groups to TiO_2 nanoparticles enables the broadband visible absorption necessary for dye-sensitized solar cells. [23 – 25] Self-assembled monolayers are also widely used as passivating layers to block unwanted surface reactions, such as those that form electronic trap sites or other unwanted defects. For example, silicon surfaces terminated by a monolayer of H atoms have electronic properties rivaling those of state-of-the-art gate oxides.[26,27] From a scientific perspective, the structure of self-assembled monolayers reveals information about molecular interactions and monolayer formation — information that is necessary for the design of new monolayers with improved performance and stability.

We demonstrate the formation of near-ideal benzoate monolayers on atomically flat rutile (110) surfaces using an entirely wet chemical process. In addition to its simplicity and low cost, this procedure avoids the use of sputtering and annealing cycles, which are known to create a significant density of chemically active surface and subsurface defects, such as O vacancies and Ti interstitials.[28]

These high-quality benzoate monolayers, in combination with Monte Carlo simulations and *ab initio* calculations, reveal the structural origin of the "benzoate dimers" reported by previous researchers. Multiple scanning tunneling microscopy (STM) investigations[29–31] of benzoic acid adsorption on rutile (110) have shown the apparent pairing of benzoate monomers, whereas similar studies[32,33] found no evidence of pairing. In agreement with the latter experiments, computational investigations of potential dimer structures found no stable dimers.[34]

We show that intermolecular interactions — primarily π-π interactions that are dominated by electric quadrupole and dispersion forces — lead to the formation of a repeating tetramer structure that stabilizes the monolayer. In the lowest energy state of this structure, adjacent molecules tilt toward one another,

leading to a paired or "dimer" topography in STM. While this tilting further stabilizes the monolayer, the energetic gain from tilting is comparable to thermal energy. As a result, the solution-prepared monolayer contains both paired and unpaired regions as well as other characteristic packing defects.

This repeating tetramer is a common structural motif in aromatic crystals and monolayers. Tetramers are observed in the benzene crystal structure, and the structurally similar edge-to-face herringbone is found in organic thin films, such as pentacene[35] or para-sexiphenyl (6P),[36,37] adsorbed on amorphous substrates. This packing configuration stabilizes organic monolayers and affects their performance. For example in the case of pentacene, subtle changes in packing between the monolayer, thin-film, and bulk phases significantly affect the electronic properties of the organic layer.[35]

The structural insights gained from this study when coupled with ongoing studies of monolayer reactivity will provide the basis for rational synthesis of, for example, dual-function monolayers that provide necessary chemical functionality while also preventing the formation of electronic trap states.

3.3 Experimental and Computational

Experimental Methods. Rutile (110) samples for ultrahigh vacuum (UHV) analysis (float zone or Verneuil) were thermally reduced in UHV at 700ºC for 5 min before use, whereas samples for infrared analysis (Verneuil) were beveled at 45° for analysis in the multiple-internal-reflection geometry. Immediately prior to use, all glassware was cleaned in a 1:1:5 solution by volume of 28% NH_4OH (aq, BDG, ACS grade):30% H_2O_2 (aq, J.T. Baker, CMOS grade):ultrapure H_2O (Milli-Q) at 80ºC for 10 min then rinsed with H_2O.

Rutile (110) samples were first etched to produce an atomically smooth surface[38] terminated by a monolayer of solvated bicarbonate[39] by immersion in a 1:1:2 by volume NH_4OH:H_2O_2:H_2O solution at 80°C for 10 min followed by a H_2O rinse. This hydrophilic surface was used as a reference for all infrared spectra. Samples were then immersed in a 16 mM solution of benzoic acid (Sigma, >99%) at either 100°C or room temperature for 10 min. Both procedures produced hydrophobic, benzoate-terminated surfaces

that would become hydrophilic after as little as 5 sec re-immersion in H_2O, consistent with monolayer removal.

Samples were transferred to a UHV chamber through an oil-free load-lock or to a dry-air-purged infrared spectrometer (Nicolet 670). STM images were obtained in UHV at room temperature using recrystallized tungsten tips[40] prepared by field-directed sputter sharpening.[41] X-ray photoelectron spectroscopy (XPS) was performed with unmonochromated Mg Kα x-rays; the photoelectrons were collected at 45° or 70° from the surface normal. Either a Shirley or a Tougaard baseline was removed from all reported spectra.[42] Small energy corrections (~0.05 eV) were applied to the reported spectra using published reference energies[43] to offset mild band bending.[44] The C $1s$ and Ti $2p_{3/2}$ spectra were normalized to the maximum amplitude of the Ti $2p_{3/2}$ transition, whereas the O $1s$ spectra were normalized to the maximum amplitude of the O $1s$ spectrum. Infrared spectra were collected in the multiple-internal-reflection geometry using an MCT-A detector and a ZnSe grid polarizer (Molectron).

Computational Methods. Monte Carlo simulations of monolayer structure were performed using the Metropolis algorithm[45,46] on a 64 × 64 site lattice with periodic boundary conditions, a supercell that represented 4,096 unsaturated Ti atoms on rutile (110). Four "reactions" (state changes) were sampled: adsorption from the solution, desorption into the solution, diffusion along the Ti rows (*i.e.,* in the [001] direction), and benzoate rearrangement including 90° rotation of the phenyl ring and tristate tilting (left, center, and right) of the molecule (*vide infra*). The adsorption energy of site (*i, j*), $E_a(i, j)$, was assumed to have the form

$$E_a\left(i,j\right) = E_0 + \sum_{i\pm 1, j\pm 1} E_{\text{int}}\left(i,j;i',j'\right)$$

where E_0 is a constant, and the nearest-neighbor interaction energies, $E_{\text{int}}(i, j; i', j')$, were assumed to be dominated by interactions between the phenyl groups. These distance- and orientation-dependent interactions were extracted from *ab initio* calculations of benzene dimers performed at the MP2/6-31G* level.[47] The relative magnitudes of E_0 and the adsorption attempt frequency (*i.e.,* solution concentration)

were adjusted to yield a low but finite vacancy density at simulated temperatures, consistent with experiment.

Density functional theory (DFT) was used to model the structure of the benzoate monolayer on 4×2 periodically repeating slabs consisting of 5 TiO_2 trilayers separated by a 12.5 Å vacuum spacing with autocompensated surfaces (Supporting Information).[48] This supercell contained 8 unsaturated Ti atoms capable of adsorbing 4 benzoate molecules at saturation. During optimization, the positions of the bottommost TiO_2 layer and its terminating bridging O rows were held fixed. Calculations were performed using DFT within the generalized gradient approximation [49] (GGA) with the Perdew, Burke, and Ernzerhof (PBE) exchange-correlation functional,[50] as implemented in the Vienna *ab initio* simulation package (VASP).[51–54] The functional was corrected for long-range dispersion interactions using the zero damping DFT-D3 method.[55] Electron-ion interactions were described using the projector augmented wave (PAW) method.[56,57] Electronic states were expanded in plane waves with a kinetic energy cutoff of 400 eV and a $2 \times 2 \times 1$ Monkhorst-Pack grid of k points. Brillouin-zone integration was performed using Gaussian smearing. To make efficient use of computational resources, vibrational energies were calculated using density-functional perturbation theory without dispersion interactions on a 2-trilayer-thick slab held in the equilibrium geometry and terminated by pseudohydrogen (Supporting Information).[58,59] Reported vibrational energies are adjusted by a constant scaling factor (0.983) to correct for systematic errors.

3.4 Results

The structure of the bare rutile (110) surface is displayed in Figure 3.1. The surface displays alternating rows of unsaturated Ti atoms and bridging O atoms, both running parallel to the [001] direction.
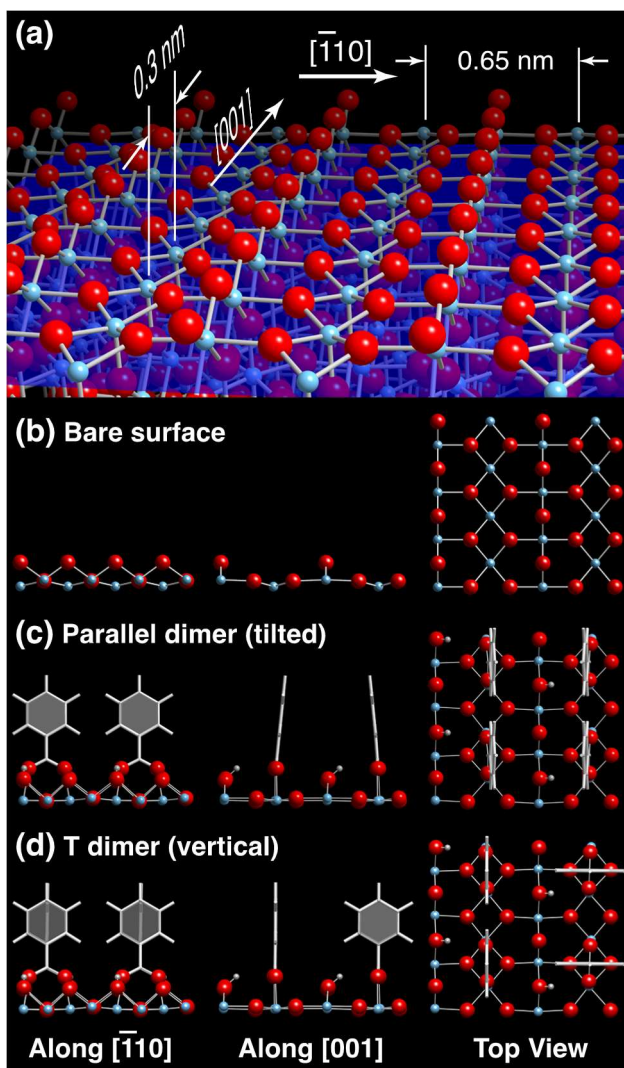
Figure 3.1: (a) Perspective view of the bare rutile (110) surface. Orthographic views of (b) the bare rutile (110) surface, (c) a possible benzoate dimer structure consisting of tilted parallel benzoate monomers, and (d) a second possible dimer structure consisting of vertical benzoate monomers in a T configuration. All geometries are minimum energy structures as determined by DFT calculations (*vide infra*). The Ti, O, and H atoms are represented by blue, red, and white balls, respectively, whereas the benzoate monomers are represented by stick figures.

STM analysis: STM images of benzoate monolayers prepared from aqueous solutions display regions of paired molecules, regions of unpaired molecules, and a variety of defect structures as shown in Figure 3.2 and Figure 3.3. Large regions of the surface display near-perfect pairing, as illustrated by Figure 3.3(a). In these regions, the bright protrusions are separated by 0.60 nm along the [001] direction, consistent with the expected bidentate bonding of benzoate. Along the [1$\overline{1}$0] direction, the paired protrusions are

separated by 0.42 nm, which is less than the expected inter-row spacing of 0.65 nm. The larger scale image in Figure 3.3(b) shows regions of pairing, identified by the characteristic interstices between the pairs, and unpaired regions. A low density of missing molecules are also observed. STM movies (Supporting Information) show little motion of the paired and unpaired regions; the interstices remain constant over hours with no apparent lengthening or shortening. In contrast, motion is observed in the vicinity of defects, including near missing molecules and staggered regions. Some regions of the surface are more disordered than others. For example, the region in Figure 3.3(c) shows many examples of staggered molecules.
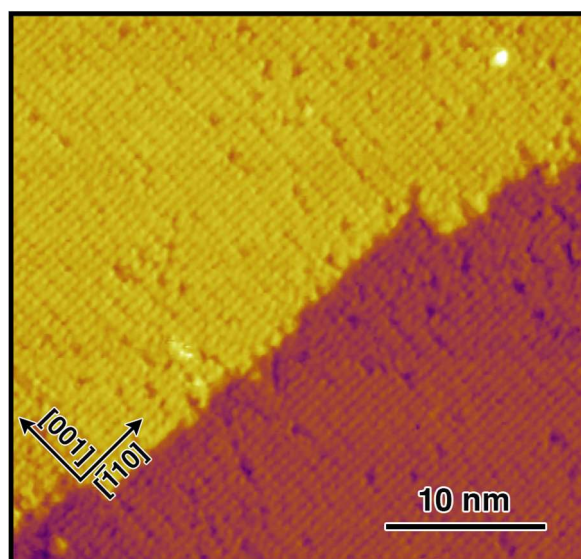
Figure 3.2: STM image of benzoate monolayer prepared from room-temperature aqueous solution of benzoic acid. The tunneling conditions were +1.80 V and 400 pA.
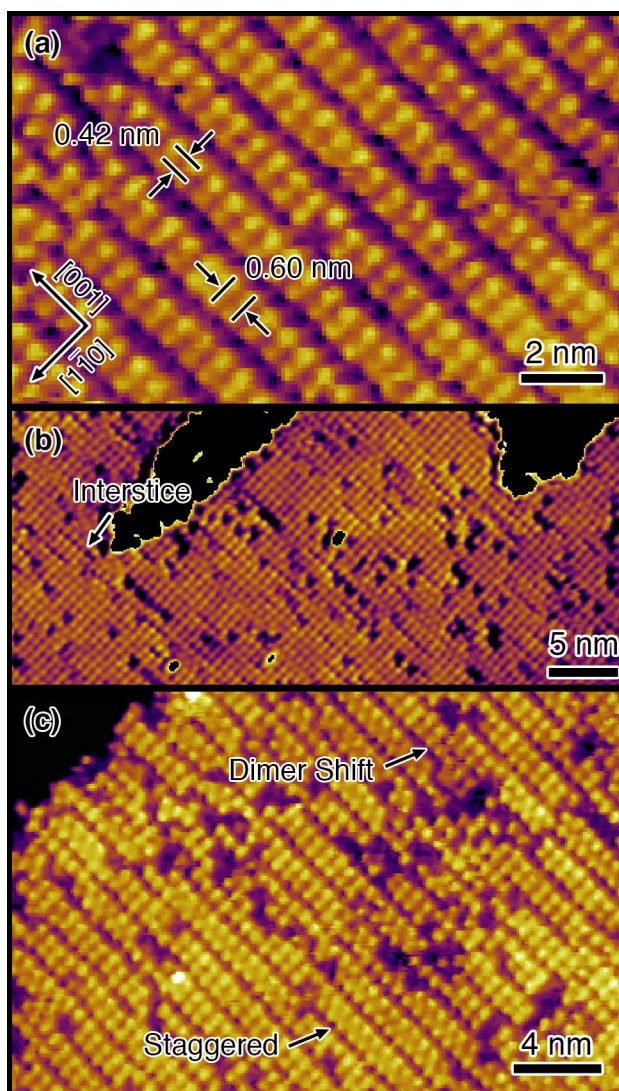
Figure 3.3: High-resolution STM images of benzoate monolayer prepared from room-temperature aqueous solutions. The tunneling conditions are given in brackets. (a) Region of near-perfect pairing [+1.80 V, 300 pA]. (b) Regions of paired and unpaired molecules, as well as defects [+1.60 V, 300 pA]. At this scale, pairing leads to characteristic interstices between the pairs. (c) Disordered region of the surface, displaying a number of characteristic defects including staggered ordering [+1.80 V, 300 pA].

Infrared spectroscopy: STM images provide little information about the conformation of individual benzoate molecules, particularly their ring orientation. In contrast, polarization spectroscopy of the aromatic C–H stretch vibration provides information on phenyl geometry, as individual C–H displacements must lie in the plane of the phenyl ring.

Infrared spectra of benzoate monolayers rule out many postulated dimer structures. Figure 3.4 shows the C–H stretch region of infrared spectra taken with *s-* and *p*-polarized light propagating along and perpendicular to the Ti rows (*i.e.,* along the [001] and [1$\bar{1}$0] directions, respectively). Only aromatic C–H stretch vibrations were observed; the intense asymmetric methylene stretch mode (~2920 cm^{-1}) characteristic of aliphatic C–H (*e.g.,* contamination) was notably absent. Without any further analysis, these spectra rule out all geometries in which the phenyl rings are face-to-face and parallel to [001] or [1$\bar{1}$0], as the C–H stretch modes in these structures would not absorb *s*-polarized light propagating parallel to [1$\bar{1}$0] or [001], respectively. One example of such a structure is given in Figure 3.1(c). Similarly, the significant differences between spectra taken in orthogonal propagation directions argue against vertical structures with equal populations of phenyl rings in two orthogonal geometries (*e.g.,* vertical benzoate dimers arranged in a T configuration as shown in Figure 3.1(d)).
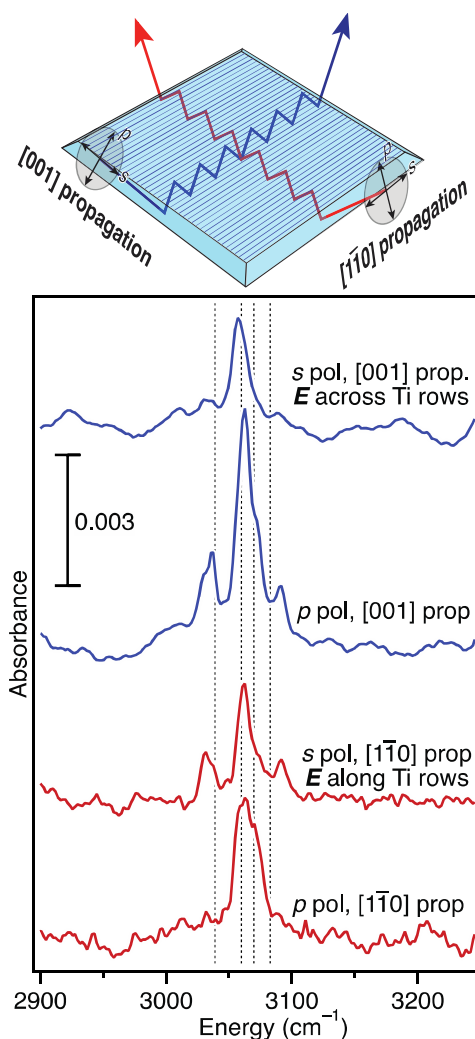
Figure 3.4: Infrared spectra of benzoate monolayer obtained with light propagating along the [001] and [1$\bar{1}$0] directions with *s*- and *p*-polarized radiation as indicated in the schematic. The lines on the top of the sketched crystal represent the Ti rows. Two different crystals were used, not the single crystal sketched. The energies of the C–H stretch modes predicted by DFT calculations of the paired tetramer geometry are indicated by vertical lines.

The sole previous infrared investigation of benzoate adsorption on rutile (110) in vacuum reported very weak, coverage-dependent O–H stretch modes at 3622 cm^{-1} and 3700 cm^{-1}. These modes were assigned to protons transferred from the acid moiety to a bridging O atom.[60] (No C–H stretch modes were reported.) We did not observe these modes. We speculate that the discrepancy may be due to the aqueous preparation, as residual H_2O H-bonded to the protonated bridging O could significantly broaden the

transition and hinder detection. Intense absorption in the rutile substrate prevented observation of modes below ~2160 cm^{-1}.

XPS analysis: The chemical identity of the monolayer was confirmed using XPS analysis. High resolution scans of the Ti $2p$ region, seen in the top panel of Figure 3.5, showed two Ti^{4+} transitions: Ti $2p_{3/2}$ at 459.3 eV and Ti $2p_{1/2}$ at 465.0 eV. Even after desorption of the monolayer, there was little evidence of Ti^{3+} defects (*e.g.,* O vacancies), which have a transition ~2 eV lower in binding energy than Ti^{4+}. The absence of O vacancies on aqueous-processed surfaces is not surprising, as surface Ti^{3+} defects are readily oxidized by even mild oxidants, such as O$_2$.[61–63] In contrast, when a sputter-damaged crystal was used, desorption of the monolayer led to the "unmasking" of Ti^{3+} defects, as shown in the inset. We attribute this unmasking to reversible charge donation from Ti interstitial defects to the monolayer.[63–67] Additional experiments exploring this phenomenon on a variety of solution-processed substrates are ongoing.
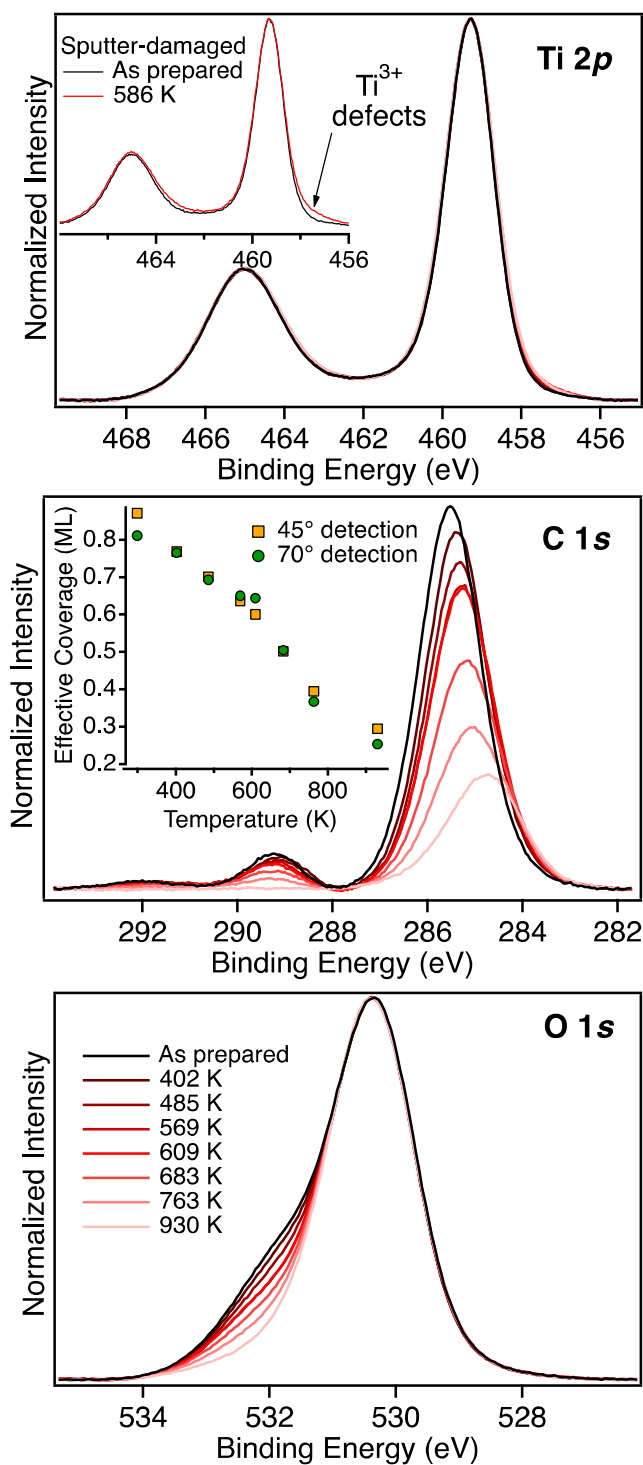
Figure 3.5: High-resolution XPS spectra of benzoate monolayers on rutile (110) detected at 70° from the surface normal showing the (top) Ti 2*p*, (middle) C 1*s*, and (bottom) O 1*s* regions as prepared and as a function of annealing temperature (20 min duration). The inset spectra in the Ti 2*p* graph are from a benzoate monolayer deposited on a sputter-damaged sample detected at 45°. The inset in the C 1*s* graph shows the effective benzoate monolayer coverage calculated from the relative areas of the Ti and C transitions using

photoelectrons collected at 45° or 70° from the surface normal. One monolayer corresponds to 7 C atoms for every two unsaturated Ti sites.

High resolution scans of the C $1s$ region, seen in the middle panel of Figure 3.5, initially showed two transitions which were assigned to carboxylate C at 289.2 eV and phenyl C at 285.5 eV. As the monolayer was heated, some of the C became graphitic (284.8 eV), while the rest desorbed. The absolute C coverage was calculated from the integrated areas of the C $1s$ and Ti $2p$ transitions as described in the Supporting Information and shown in the inset to the C $1s$ spectra. The good agreement between coverages extracted from spectra obtained at two different detection angles confirms the validity of the quantification model (Supporting Information).

High resolution scans of the O $1s$ region, seen in the bottom panel of Figure 3.5, showed two transitions that were assigned to O in carboxylate at 531.9 eV and O in TiO_2 at 530.4 eV. Consistent with the C $1s$ spectra, O associated with the carboxylate transition desorbed with heating.

The absolute benzoate coverage measured by XPS was in good agreement with STM images showing the formation of a near-complete monolayer. Approximately 75% of the monolayer desorbed with heating, while the remaining fraction was converted to graphitic C. This behavior was somewhat different than that reported for incomplete monolayers of vacuum-deposited benzoic acid, which desorbed completely without decomposition as evidenced by C $1s$ XPS.[33] We do not understand this difference, but note that the monolayers studied in Ref. 33, which were formed by electrospray deposition in UHV, were significantly less dense than the near-complete monolayers formed by solution deposition. We speculate that intermolecular interactions may influence the branching ratio between decomposition and reactive desorption.

Monte Carlo simulations: Intermolecular interactions often lead to the development of long-range structures that strain the capability of DFT simulations. For this reason, we used Monte Carlo (MC) simulations to explore potential structures and guide DFT calculations.

The assumption underlying the MC model is that interactions between adjacent phenyl groups, so-called π-π interactions, dominate interactions within the monolayer. We approximated the energetics of these

interactions using the benzene dimer intermolecular potentials calculated by Cacelli *et al.*[47] and shown in Figure 3.6(a). The nature of π-π interactions is complex, containing contributions from quadrupole-quadrupole and dispersion interactions as well as Pauli repulsion.[68,69] For simplicity, only the quadrupolar nature of these interactions is sketched in Figure 3.6(b).
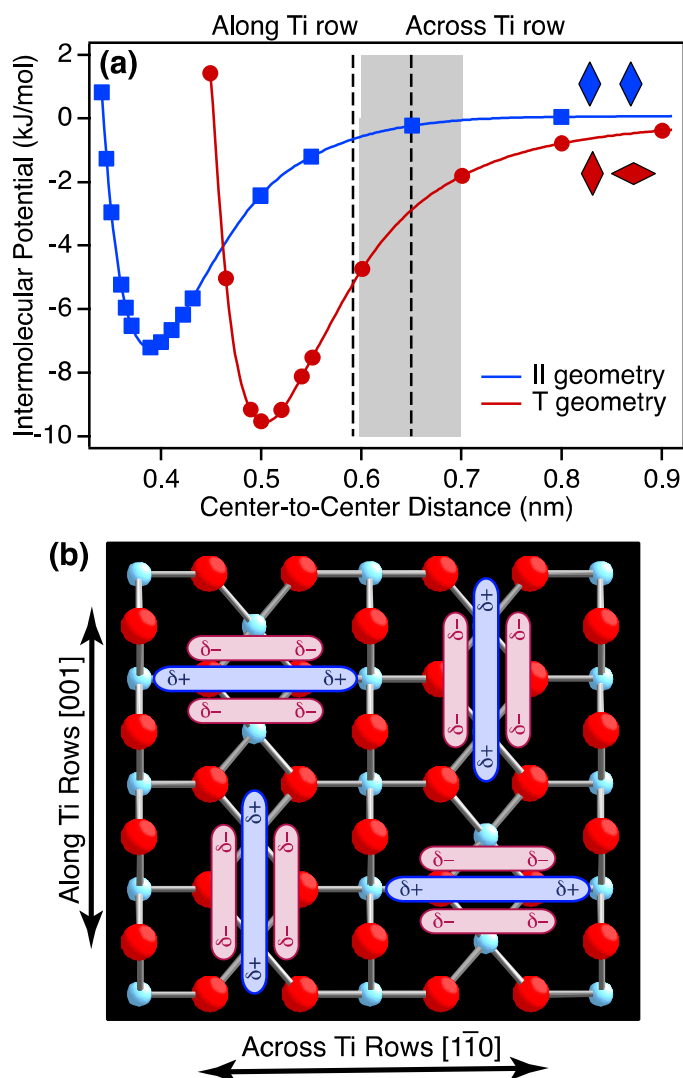
Figure 3.6: (a) Intermolecular potential of benzene dimers from Ref. 47. The vertical lines indicate the center-to-center distances for vertical molecules bonded (left) along and (right) across the Ti rows. The shaded gray band represents the range of intermolecular distances sampled by molecules tilting across the Ti rows over the range [–7°, 7°] (b) Schematic illustration of four benzoate molecules, represented as electric quadrupoles with electron density above and below the plane of the ring, bonded to rutile (110) in a tetramer configuration. The Ti and O atoms are light blue and red, respectively.

Figure 3.6 shows that at the distances relevant for adsorption on rutile (110), the monolayer is primarily stabilized by interactions between molecules in a edge-to-face or "T" geometry, with interactions between molecules along the Ti rows being the most important. Interactions between neighbors in the face-to-face or "parallel" geometry are much weaker.

If the only internal degree of freedom is the 90° rotation of the phenyl group, the MC simulations predicted the formation of a repeating tetramer structure in which all molecules adopt an edge-to-face geometry, as shown in Figure 3.7(a) and sketched in Figure 3.6(b). This structure can be rationalized in terms of electrostatics, as reorientable electric quadrupoles on a square or rectangular lattice adopt the same tetrameric ground state.[70] This structure is also consistent with the infrared adsorption data showing that C–H bonds have little polarization within the plane of the surface; however, this structure cannot explain the apparent pairing of benzoate models. Something was missing from the model.
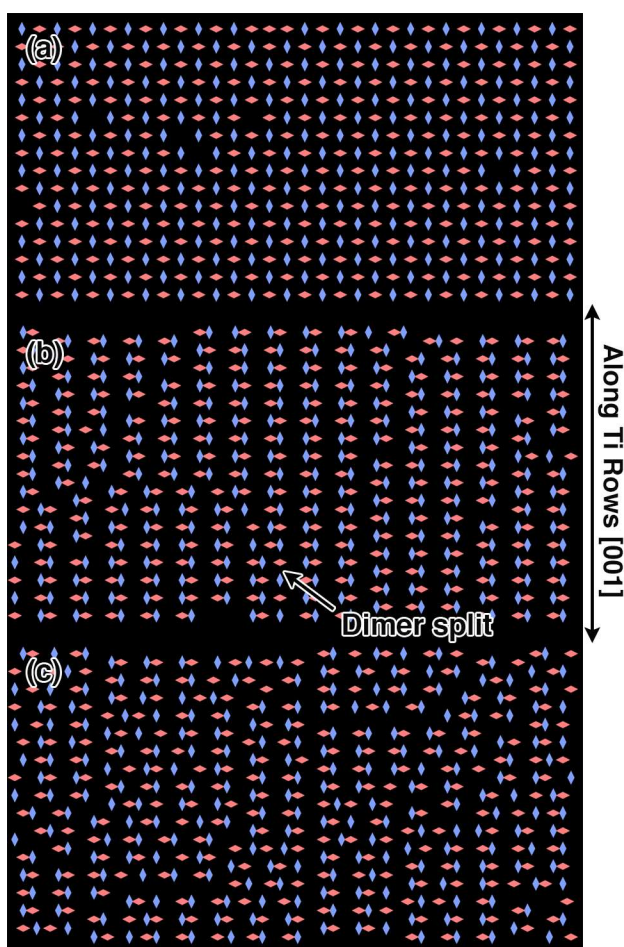
Figure 3.7: Regions of Monte Carlo simulations of benzoate monolayer structure. The long axis of each diamond represents the plane of the phenyl ring; the two colors represent the two allowed orientations. (a) When tilting is not allowed, the molecules adopt a tetramer geometry. When tilting is allowed, the molecules tend to tilt toward one another, leading to an apparent pairing. The extent of pairing is greatest at (b) low temperature, decreasing at (c) higher temperature.

The initial model neglected an important degree of freedom: tilting of the benzoate molecule about the two Ti–O bonds. Because of the long moment arm of the molecule, this tilting motion leads to significant translation of the phenyl group along the $[1\bar{1}0]$ direction (*i.e.,* across the Ti rows). For example, if two adjacent molecules each tilt 7° toward one another (*vide infra*), the center-to-center distance of the phenyl groups decreases by 0.1 nm. Neglecting the small changes in relative ring orientation, the potential energy diagram in Figure 3.6(a) suggests that this distortion would lead to significant stabilization.

Including benzoate tilting in the MC simulation, modeled as a tristate translation along $[1\bar{1}0]$ direction, led to a temperature-dependent pairing interaction. At low temperatures, the monolayer adopted a paired tetramer configuration as shown in Figure 3.7(b). Additionally, a number of "dimer shifts" are observed, similar to the defects highlighted in Figure 3.3(c). We propose that this paired tetramer is the structure of the "dimers" observed in STM images. At higher temperatures, some regions of the surface are paired, while others are unpaired, as shown in Figure 3.7(c). Within the unpaired regions, some molecules are unpaired, whereas others are paired. The unpairing transition has long-range order. This collective behavior is due to the coupling of molecules along the Ti rows. When one pair of molecules in a paired region dissociates, the energy of the monolayer increases for two reasons: the increased distance between the two unpaired molecules across the Ti rows and the increased distance of the unpaired molecules to their four nearest neighbors along the Ti rows. After dissociation of the first pair, the dissociation of an adjacent pair requires less energy, as the energy gain and loss from nearest-neighbor interactions cancels out.

DFT calculations: To test the validity of the very simple MC model and its predicted ground state structure, DFT calculations were performed on a 4×2 TiO_2 supercell containing four benzoate molecules adsorbed in a variety of configurations. The relative energies of these configurations are shown in Figure

3.8. The lowest energy state of the system is a tetramer with adjacent benzoate molecules tilted by 7°, as shown in Figure 3.8 and consistent with the MC simulations. Monolayers formed from dimerized structures, including parallel, T, and staggered parallel configurations (Supporting Information), had uniformly higher energy.
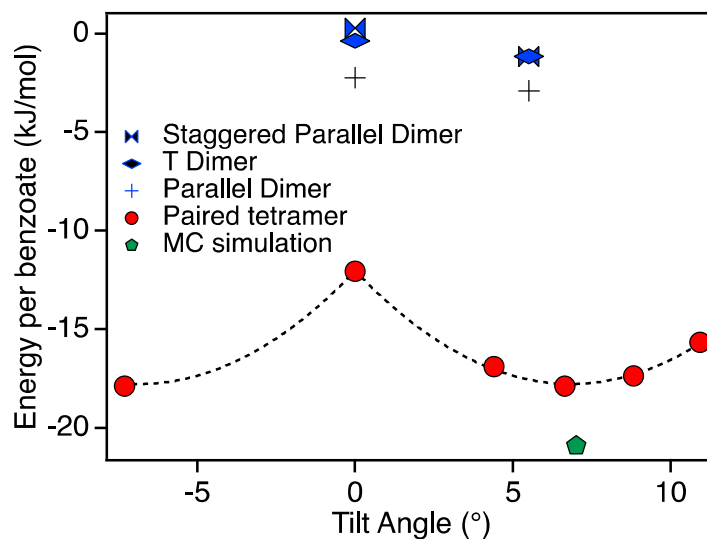
Figure 3.8: Relative energies estimated from DFT calculations of (blue) dimer and (red) tetramer monolayer configurations as a function of tilt angle from the surface normal. The three dimer configurations are shown in Supporting Information. The energy estimated from the MC simulation is shown in green for comparison. The dotted line is a polynomial fit.
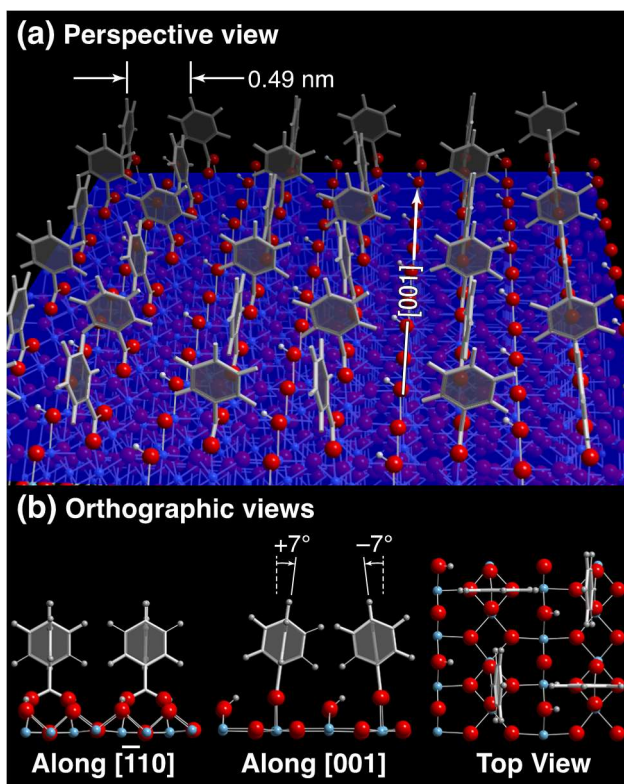
Figure 3.9: The lowest energy structure of a benzoate monolayer from DFT calculations. The benzoate monomers are arranged in a tetramer in which every phenyl ring is oriented in an edge-to-face geometry with its four nearest neighbors. Adjacent pairs of benzoate molecules tilt toward one another by 7° along the $[\bar{1}10]$ direction, leading to a 0.49 nm spacing between terminal H atoms. (a) Perspective view of multiple unit cells, and (b) orthographic views of single unit cell. The Ti, O, and H atoms are represented by blue, red, and white balls, respectively, whereas the benzoate monomers are represented by stick figures.

The intermolecular energies predicted by the MC and DFT simulations were in surprisingly good agreement, particularly given the simplicity of the MC model and the different levels of theory underlying the simulations (*i.e.,* MP2/6-31G* vs. PBE-D3). Taking the energy of the staggered dimer structure as that of a non-interacting monolayer, the DFT calculations yielded an intermolecular energy in the paired tetramer structure of –17.9 kJ/mol per benzoate molecule, whereas the MC simulations yielded –20.9 kJ/mol — a 15% difference. This good agreement suggests that interactions within the monolayer are dominated by π–π interactions between the phenyl rings.

The infrared spectrum of the benzoate monolayer was calculated using the paired tetramer geometry, as shown in Figure 3.4. The energies of the C–H stretch modes obtained from experiment and simulation are

in reasonable agreement. The absolute intensities of the experimental and simulated spectra cannot be directly compared due to uncertainties in the effective dielectric constant of the adsorbate layer, which screens transition dipoles oriented perpendicular to the surface.[71,72] The polarization dependence is analyzed in the Supporting Information.

3.5 Discussion

These experiments show that high-quality, self-assembled benzoate monolayers can be synthesized on rutile (110) surfaces using simple aqueous reactions. Sputtering and annealing cycles, which create surface and subsurface defects, are not needed. The monolayers are hydrophobic and remain largely contaminant free during exposures to laboratory air for tens of minutes. During this period, infrared spectroscopy shows that the monolayers do not spontaneously adsorb air-born hydrocarbons or other adventitious aliphatic species. Monolayer stability is driven both by the strong bidentate bonding to unsaturated Ti atoms on the surface as well as by π-π interactions between adsorbates.

Benzoate deposition is reversible. The hydrophobicity of the treated crystals can be reversed by a brief immersion in H_2O, suggesting that monolayer formation and annealing in the solution is a dynamic process with constant exchange of molecules between surface and solution. In contrast, time-dependent STM showed no indication of monolayer annealing over hour-long observations; the regions of pairing and unpairing were essentially static. Experiments on benzoate diffusion *in vacuo* are ongoing; however, we hypothesize that monolayer annealing occurs predominantly through adsorption/desorption events in solution, not surface diffusion.

The STM images, infrared spectra, MC simulations, and DFT calculations are all consistent with benzoate molecules adopting an edge-to-face ring geometry with their four nearest neighbors — a tetrameric bonding geometry. This bonding is further stabilized by a pairing interaction between adjacent benzoate molecules, a pairing that has previously been interpreted as "dimerization." This pair formation is also consistent with previous studies of the absorption of polarized x-rays.[73] The coexistence of paired and

unpaired regions of the monolayer is consistent with the relatively small additional energy gained by pairing and the cooperative nature of the pairing interaction.

Higher order multiplets, such as triplets, are occasionally seen in STM images, as noted by previous researchers.[29] In agreement with this, the MC simulations transition from pair to triplet formation if larger tilt angles are allowed. The preference for pair formation in benzoate monolayers represents a balance between the energy gain from increased $\pi-\pi$ interactions at higher tilt angles and the energy loss from reduced orbital overlap in the Ti-O bonds. We speculate that monolayers formed from longer aromatic molecules, such as phenyl benzoic acid, may form more interesting, higher order structures.

Benzoate monolayers on rutile (110) bear many structural similarities to organic monolayers on amorphous substrates, such as SiO_2, particularly the tendency for edge-to-face ring packing geometries.[35-37] The principal difference between the two is that the rutile substrate enforces a particular packing density. The most surprising finding of this study is that the monolayer structure and stabilization energy could be predicted by a very simple MC model that included little more than the surface geometry and intermolecular potential of a small-molecule analogue of the monolayer head group. This finding suggests that similarly simple models may be useful in designing new monolayers with specific functionality.

3.6 Conclusions

High-quality, self-assembled benzoate monolayers can be synthesized on rutile (110) surfaces using simple aqueous reactions. The monolayers are stable and remain contaminant free in air for tens of minutes. This stability is driven both by the strong bidentate bonding to unsaturated Ti atoms on the surface as well as by $\pi-\pi$ interactions between adsorbates. The benzoate molecules form tetramers in which each molecule adopts an edge-to-face ring geometry with its four nearest neighbors. This arrangement is further stabilized by tilting adjacent benzoate molecules toward one another, a pairing that has previously been interpreted as dimerization. The monolayer structure and stabilization energy could be predicted by a very simple model that included the surface geometry and intermolecular potential of a

small-molecule analogue of the monolayer head group. This finding suggests that similarly simple models may be useful in designing new monolayers with specific functionality.

Author Information

Corresponding Author

Melissa.Hines@cornell.edu, +1-607-255-3040

Notes

The authors declare no competing financial interest.

Acknowledgments

Supporting Information Available: The Supporting Information is available free of charge on the ACS Publications website.

STM movie of benzoate monolayer, XPS quantification of carbon coverage, information on vibrational energy calculations, structures used in DFT calculations.

References

[23] O'Regan, B.; Grätzel, M. A Low-Cost, High-Efficiency Solar Cell Based on Dye-Sensitized Colloidal TiO$_2$ Films. *Nature* **1991**, *353*, 737-740.

[24] Hagfeldt, A.; Grätzel, M. Molecular Photovoltaics. *Acc. Chem. Res.* **2000**, *33*, 269-277.

[25] Ardo, S.; Meyer, G. J. Photodriven Heterogeneous Charge Transfer With Transition-Metal Compounds Anchored to TiO$_2$ Semiconductor Surfaces. *Chem. Soc. Reviews* **2009**, *38*, 115-164.

[26] Yablonovitch, E.; Allara, D. L.; Chang, C. C.; Gmitter, T.; Bright, T. B. Unusually Low Surface-Recombination Velocity on Silicon and Germanium Surfaces. *Phys. Rev. Lett.* **1986**, *57*, 249-252.

[27] Peng, W.; DeBenedetti, W. J. I.; Kim, S.; Hines, M. A.; Chabal, Y. J. Lowering the Density of Electronic Defects on Organic-Functionalized Si(100) Surfaces. *Appl. Phys. Lett.* **2014**, *104*, 241601.

[28] Jensen, S. C.; Friend, C. M. The Dynamic Roles of Interstitial and Surface Defects on Oxidation and Reduction Reactions on Titania. *Top. Catal.* **2013**, *56*, 1377-1388.

[29] Guo, Q.; Cocks, I.; Williams, E. M. The Adsorption of Benzoic Acid on a $TiO_2(110)$ Surface Studied Using STM, ESDIAD, and LEED. *Surf. Sci.* **1997**, *393*, 1-11.

[30] Guo, Q.; Williams, E. M. The Effect of Adsorbate-Adsorbate Interaction on the Structure of Chemisorbed Overlayers on $TiO_2(110)$. *Surf. Sci.* **1999**, *433-435*, 322-326.

[31] Grinter, D. C.; Woolcot, T.; Pang, C.-L.; Thornton, G. Ordered Carboxylates on $TiO_2(110)$ Formed At Aqueous Interfaces. *J. Phys. Chem. Lett.* **2014**, *5*, 4265-4269.

[32] Grinter, D. C.; Nickels, P.; Woolcot, T.; Basahel, S. N.; Obaid, A. Y.; Al-Ghamdi, A. A.; El-Mossalamy, E.-S. H.; Alyoubi, A. O.; Thornton, G. Binding of a Benzoate Dye-Molecule Analogue to Rutile Titanium Dioxide Surfaces. *J. Phys. Chem. C* **2012**, *116*, 1020-1026.

[33] Landis, E. C.; Jensen, S. C.; Phillips, K. R.; Friend, C. M. Photostability and Thermal Decomposition of Benzoic Acid on TiO_2. *J. Phys. Chem. C* **2012**, *116*, 21508-21513.

[34] Zhao, X. I.; Bowler, D. R. DFT Studies of Adsorption of Benzoic Acid on the Rutile (110) Surface: Modes and Patterns. 2014 *arXiv:1407.1659v1 [cond-mat.mtrl-sci].* arXiv.org e-Print archive. http://arxiv.org/abs/1407.1659 (accessed May 10, 2016).

[35] Mannsfeld, S. C. B.; Virkar, A.; Reese, C.; Toney, M. F.; Bao, Z. Precise Structure of Pentacene Monolayers on Amorphous Silicon Oxide and Relation to Charge Transport. *Adv. Mater.* **2009**, *21*, 2294-2298.

[36] Hlawacek, G.; Teichert, C. Nucleation and Growth of Thin Films of Rod-Like Conjugated Molecules. *J. Phys.: Condens. Matter* **2013**, *25*, 143202.

[37] Kleppmann, N.; Klapp, S. H. L. A Scale-Bridging Modeling Approach for Anisotropic Organic Molecules At Patterned Semiconductor Surfaces. *J. Chem. Phys.* **2015**, *142*, 064701.

[38] Song, A.; Jing, D.; Hines, M. A. Rutile Surface Reactivity Provides Insight Into the Structure-Directing Role of Peroxide in TiO_2 Polymorph Control. *J. Phys. Chem. C* **2014**, *118*, 27343-27352.

[39] Song, A.; Skibinski, E. S.; DeBenedetti, W. J. I.; Ortoll-Bloch, A. G.; Hines, M. A. Nanoscale Solvation Leads to Spontaneous Formation of a Bicarbonate Monolayer on Rutile (110) Under Ambient Conditions: Implications for CO_2 Photoreduction. *J. Chem. Phys. C* **2016**, *120*, 9326-9333.

[40] Greiner, M.; Kruse, P. Recrystallization of Tungsten Wire for Fabrication of Sharp and Stable Nanoprobe and Field-Emitter Tips. *Rev. Sci. Instrum.* **2007**, *78*, 026104.

[41] Schmucker, S. W.; Kumar, N.; Abelson, J. R.; Daly, S. R.; Girolami, G. S.; Bischof, M. R.; Jaeger, D. L.; Reidy, R. F.; Gorman, B. P.; Alexander, J.; *et al.* Field-Directed Sputter Sharpening for Tailored Probe Materials and Atomic-Scale Lithography. *Nat Commun* **2012**, *3*, 935.

[42] Hofmann, S. Auger- and X-ray Photoelectron Spectroscopy in Materials Science: A User-Oriented Guide; Springer: Heidelberg, 2013; pp 528.

[43] Diebold, U.; Madey, T. E. TiO_2 by XPS. *Surface Science Spectra* **1998**, *4*, 227-231.

[44] Hugenschmidt, M. B.; Gamble, L.; Campbell, C. T. The Interaction of H_2O With a $TiO_2(110)$ Surface. *Surf. Sci.* **1994**, *302*, 329-340.

[45] Metropolis, N.; Rosenbluth, A.; Rosenbluth, M. N.; Teller, A.; Teller, E. Equation of State Calculations By Fast Computing Machines. *J. Chem. Phys.* **1953**, *21*, 1087-1092.

[46] Jorgensen, W. J. Perspective on "Equation of State Calculations By Fast Computing Machines". *Theor. Chem. Acc.* **2000**, *103*, 225-227.

[47] Cacelli, I.; Cinacchi, G.; Prampolini, G.; Tani, A. Modeling Benzene With Single-Site Potentials From *Ab Initio* Calculations: A Step Toward Hybrid Models of Complex Molecules. *J. Chem. Phys.* **2004**, *120*, 3648-3656.

[48] Diebold, U. The Surface Science of Titanium Dioxide. *Surf. Sci. Reports* **2003**, *48*, 53-229.

[49] Kohn, W.; Sham, L. J. Self-Consistent Equations Including Exchange and Correlation Effects. *Phys. Rev.* **1965**, *140*, A1133-A1138.

[50] Perdew, J. P.; Burke, K.; Ernzerhof, M. Generalized Gradient Approximation Made Simple. *Phys. Rev. Lett.* **1996**, *77*, 3865-3868.

[51] Kresse, G.; Hafner, J. *Ab Initio* Molecular Dynamics for Liquid Metals. *Phys. Rev. B* **1993**, *47*, 558-561.

[52] Kresse, G.; Hafner, J. *Ab Initio* Molecular-Dynamics Simulation of the Liquid-Metal-Amorphous-Semiconductor Transition in Germanium. *Phys. Rev. B* **1994**, *49*, 14251-14269.

[53] Kresse, G.; Furthmüller, J. Efficiency of *Ab-Initio* Total Energy Calculations for Metals and Semiconductors Using a Plane-Wave Basis Set. *Comput. Mat. Sci.* **1996**, *6*, 15-50.

[54] Kresse, G.; Furthmüller, J. Efficient Iterative Schemes for *Ab Initio* Total-Energy Calculations Using a Plane-Wave Basis Set. *Phys. Rev. B* **1996**, *54*, 11169-11186.

[55] Grimme, S.; Antony, J.; Ehrlich, S.; Krieg, H. A Consistent and Accurate *Ab Initio* Parameterization of Density Functional Dispersion Correction (DFT-D) for the 94 Elements H-Pu. *J. Chem. Phys.* **2010**, *132*, 154104.

[56] Blöchl, P. E. Projector Augmented-Wave Method. *Phys. Rev. B* **1994**, *50*, 17953-17979.

[57] Kresse, G.; Joubert, D. From Ultrasoft Pseudopotentials to the Projector Augmented-Wave Method. *Phys. Rev. B* **1999**, *59*, 1758-1775.

[58] Kowalski, P. M.; Meyer, B.; Marx, D. Composition, Structure, and Stability of the Rutile $TiO_2(110)$ Surface: Oxygen Depletion, Hydroxylation, Hydrogen Migration, and Water Adsorption. *Phys. Rev. B* **2009**, *79*, 115410.

[59] Camellone, M. F.; Kowalski, P. M.; Marx, D. Ideal, Defective, and Gold-Promoted Rutile $TiO_2(110)$ Surfaces Interacting With CO, H_2, and H_2O: Structures, Energies, Thermodynamics, and Dynamics From PBE+*U*. *Phys. Rev. B* **2011**, *84*, 035413.

[60] Buchholz, M.; Xu, M.; Noei, H.; Wiedler, P.; Nefedov, A.; Fink, K.; Wang, Y.; Wöll, C. Interaction of Carboxylic Acids With Rutile $TiO_2(110)$: IR Investigations of Terphthalic and Benzoic Acid Adsorbed on a Single Crystal Substrate. *Surf. Sci.* **2016**, *643*, 117-123.

[61] Henderson, M. A.; Epling, W. S.; Peden, C. H. F.; Perkins, C. L. Insights Into Photoexcited Electron Scavenging Processes on TiO_2 Obtained From Studies of the Reaction of O_2 With OH Groups Adsorbed At Electronic Defects on $TiO_2(110)$. *J. Phys. Chem. B* **2003**, *107*, 534-545.

[62] Lira, E.; Hansen, J. Ø.; Huo, P.; Bechstein, R.; Galliker, P.; Lægsgaard, E.; Hammer, B.; Wendt, S.; Besenbacher, F. Dissociative and Molecular Oxygen Chemisorption Channels on Reduced Rutile $TiO_2(110)$: An STM and TPD Study. *Surf. Sci.* **2010**, *604*, 1945-1960.

[63] Papageorgiou, A. C.; Beglitis, N. S.; Pang, C. L.; Teobaldi, G.; Cabailh, G.; Chen, Q.; Fisher, A. J.; Hofer, W. A.; Thornton, G. Electron Traps and Their Effect on the Surface Chemistry of $TiO_2(110)$. *P. Natl. Acad. Sci. USA* **2010**, *107*, 2391-2396.

[64] Petrik, N. G.; Zhang, Z.; Du, Y.; Dohnálek, Z.; Lyubinetsky, I.; Kimmel, G. A. Chemical Reactivity of Reduced TiO$_2$(110): The Dominant Role of Surface Defects in Oxygen Chemisorption. *J. Phys. Chem. C* **2009**, *113*, 12407-12411.

[65] Dohnálek, Z.; Lyubinetsky, I.; Rousseau, R. Thermally-Driven Processes on Rutile TiO$_2$(110)-(1×1): A Direct View At the Atomic Scale. *Prog. Surf. Sci.* **2010**, *85*, 161-205.

[66] Wendt, S.; Sprunger, P. T.; Lira, E.; Madsen, G. K. H.; Li, Z.; Hansen, J. Ø.; Matthiesen, J.; Blekinge-Rasmussen, A.; Lægsgaard, E.; Hammer, B.; *et al.* The Role of Interstitial Sites in the Ti 3*d* Defect State in the Band Gap of Titania. *Science* **2008**, *320*, 1755-1759.

[67] Lira, E.; Wendt, S.; Huo, P.; Hansen, J. Ø.; Streber, R.; Porsgaard, S.; Wei, Y.; Bechstein, R.; Lægsgaard, E.; Besenbacher, F. The Importance of Bulk Ti^{3+} Defects in the Oxygen Chemistry on Titania Surfaces. *J. Am. Chem. Soc.* **2011**, *133*, 6529-6532.

[68] Grimme, S. Do Special Noncovalent π-π Stacking Interactions Really Exist? *Angew. Chem. Int. Ed.* **2008**, *47*, 3430-3434.

[69] Martinez, C. R.; Iverson, B. L. Rethinking the Term "Pi-Stacking". *Chem. Sci.* **2012**, *3*, 2191-2201.

[70] Massidda, V.; Hernando, J. Order-Disorder Transitions for a Two-Dimensional Lattice of Reorientable Quadrupoles in the Mean-Field Approximation. *Physica A* **1984**, *128*, 318-333.

[71] Chabal, Y. J. Surface Infrared Spectroscopy. *Surf. Sci. Reports* **1988**, *8*, 211-357.

[72] Clark, I. T.; Aldinger, B. S.; Gupta, A.; Hines, M. A. Extracting Maximum Information From Polarized Surface Vibrational Spectra: Application to Etched, H-Terminated Si(110) Surfaces. *J. Chem. Phys.* **2008**, *128*, 144711.

[73] Schnadt, J.; Schiessling, J.; O'Shea, J. N.; Gray, S. M.; Patthey, L.; Johansson, M. K.-J.; Shi, M.; Krempasky, J.; Åhlund, J.; Karlsson, P. G.; *et al.* Structural Study of Adsorption of Isonicotinic Acid and Related Molecules on Rutile TiO$_2$(110) I: XAS and STM. *Surf. Sci.* **2003**, *540*, 39-54.

Chapter 4

Molecular Insight into TiO$_2$ Photocatalysis in Ambient Conditions

4.1 Introduction

Titanium dioxide shows promise in a wide array of photocatalytic applications, such as carbon dioxide photoreduction,[1] water splitting[2] and degradation of pollutants.[3] Despite widespread effort, these reactions are not efficient enough for widespread adoption. Rational improvement of the photocatalytic performance of the materials used in these applications is stymied by a general lack of fundamental understanding of the reactions that occur on their surfaces, especially in technologically relevant environments such as air or aqueous solutions.

An ideal platform to study photocatalytic reactions between organic molecules and metal oxides is a self-assembled monolayer on an atomically flat surface. This provides a highly uniform system, in which essentially all molecules are bound in the same manner to the same type of surface site, greatly simplifying the interpretation of data. Figure 4.1 displays a highly homogeneous monolayer of phenylphosphinate on rutile TiO$_2$ that was prepared entirely in solution, where each individual protrusion is an adsorbed phenylphosphinate molecule. In fact, organic monolayers (and submonolayers) on single crystal TiO$_2$ have been used in many studies of metal oxide photoreactivity;[4-8] however, previous studies were all performed in ultrahigh vacuum or high vacuum conditions. These studies provided valuable information, yet fell short of representing the atmospheric pressure conditions where TiO$_2$ is typically applied.
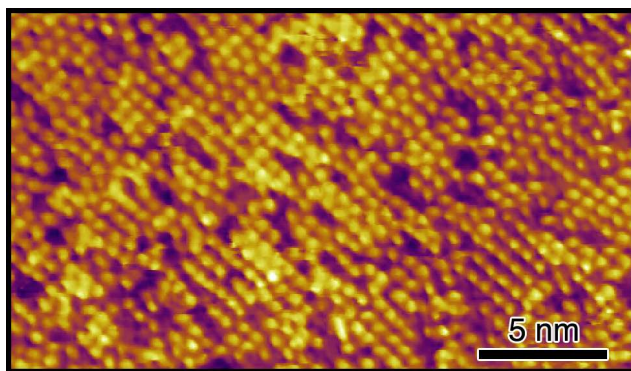
Figure 4.1: STM image of a solution-prepared monolayer of phenylphosphinate on rutile (110).

Here, we demonstrate a new approach to studying metal oxide photocatalysis: photoreactions of organic monolayers on well-controlled TiO_2 surfaces that are prepared and reacted in ambient environments. This provides atomic-scale insight into photoreactions under conditions that are directly applicable to those in which TiO_2 is applied. We combine *in-situ* infrared spectroscopy of the photodecomposition of organic monolayers in air, which provides quantitative and kinetic chemical information, with *ex-situ* scanning tunneling microscopy (STM), which provides atomic-scale information. Additionally, x-ray photoelectron spectroscopy (XPS) provides complementary chemical information.

In application, TiO_2 is often used as a mixture of highly faceted nanocrystals composed of both rutile and anatase TiO_2. The reactions that enable these applications occur on the surface of the nanocrystals. As such, it is important to understand the reactivity at surfaces of both phases of TiO_2. While high-quality single crystals of rutile are readily available, anatase is only thermodynamically stable at the nanoscale, making it difficult to obtain large, high-purity single crystals. To provide anatase substrates large enough for spectroscopic study, we developed a hydrothermal heteroepitaxial growth method, which produces high-quality epitaxial anatase (001) films on strontium titanate (100) substrates.

Using this approach we show that the photodecomposition of two different organic monolayers on both anatase and rutile shows unexpected biexponential reaction kinetics, where the photodecompostion rate decreases by approximately two orders of magnitudes after a fraction (typically ~1/4) of the molecules

have reacted. We propose that this behavior results from changes in band bending as a result of the photoreaction occurring on the surface.

4.3 Experimental Methods

All solution-phase preparations were performed using labware that had been cleaned with a modified RCA process.[9] Prior to each use, labware was immersed in a bath of 1:1:5 28% NH_4OH (aq, BDH, ACS grade): 30% H_2O_2 (aq, J.T. Baker, CMOS grade): H_2O (Milli-Q) for 10 min at 80°C. The labware was additionally cleaned in an acidic peroxide bath of 1:1:5 37% HCl (aq, BDH, ACS grade): H_2O_2 (aq, J.T. Baker, CMOS grade): H_2O (Milli-Q) if used to prepare a sample for analysis in UHV. Labware was thoroughly rinsed in flowing water before cleaning, in between each step, and as a final step.

Rutile TiO_2 samples were single crystals of rutile (110) (MTI, undoped). Fresh samples for use in STM were thermally reduced by heating them to ~700°C for 5 min in UHV to provide the conductivity necessary for STM, resulting in a light blue color of the crystal.

Heteroepitaxial anatase (001) TiO_2 films were hydrothermally grown on single-crystal $SrTiO_3$ (100) (MTI) substrates using two different sets of conditions. Prior to growth, $SrTiO_3$ samples were either annealed in air at 1000°C for 12 hr or etched in 1:1:5 H_2O_2:NH_4OH:H_2O for 40 min at 40°C, both of which provide an atomically smooth surface. If the anatase films were used for XPS and STM, they were grown on 0.05% Nb-doped crystals. These films were grown by immersing a Nb-doped $SrTiO_3$ crystal face down in an aqueous solution of 9 mM TiF_4, 2 mM HCl, and 0.1 M NaCl for 4 hr in a PTFE-lined acid digestion vessel (Parr) placed in a preheated 120°C oven. Anatase films for infrared spectroscopy were grown on undoped $SrTiO_3$ by immersing the substrate vertically in an aqueous solution of 0.70 mM TiF_4 for 5 hr in a PTFE-lined acid digestion vessel placed in a preheated 120°C oven. After growth, samples were heated at 350°C for 12 hr in air to remove trapped H_2O. Anatase films for use in STM were thermally reduced to provide conductivity, typically for 30 min at 650°C and sometimes sputtered at 500 eV with Ar^+ (5 min, 2 μA sputter current). If sputtered, the sample was annealed again to 650°C for 30 min.

Self-assembled monolayers of benzoate or phenylphosphinate were prepared on TiO_2 surfaces by immersion in aqueous solutions containing the respective organic acids.[10,11] Rutile samples were first etched and cleaned in a basic peroxide solution of 1:1:5 H_2O_2:NH_4OH:H_2O for 10 min at 80°C resulting in an atomically flat bicarbonate-terminated surface.[12] Anatase films were cleaned by rinsing in 28%NH_4OH, rinsing in H_2O, then heating to 350°C for 30 min in air. Benzoate or phenylphosphinate monolayers were prepared by immersing samples for 2 min in a 16 mM aqueous solution of benzoic acid (Sigma, >99%) or a 13 mM aqueous solution of phenylphosphinic acid (Sigma, >99%), respectively.

Infrared spectra were collected in the multiple-internal-reflection (MIR) geometry with a mercury-cadmium-telluride detector in a dry-air-purged spectrometer (Nicolet 670). Rutile samples for infrared spectroscopy were beveled at 45° along parallel edges from $10 \times 10 \times 0.5$ mm die to allow infrared light to make ~19 internal reflections along the $[1\overline{1}0]$ direction. Anatase films for infrared spectroscopy were hydrothermally grown on undoped $10 \times 10 \times 0.5$mm $SrTiO_3$ crystals, which were similarly beveled at 45° along parallel edges.

Photoreactions were studied in the dry-air-purged infrared spectrometer. Monolayers were prepared in solution on beveled samples, and then the monolayer was rinsed off from the bottom face. Rinsing was performed by pressing just the bottom of the crystal against an aliquot of water for ~5 sec. This was repeated 3 times each with 3 separate aliquots. This procedure was necessary because the MIR geometry probes both the upper and lower surfaces. Selectively rinsing the monolayer off the bottom surface ensured that all molecules received the same UV flux during top-down illumination. Spectra were collected from the cleaned sample before deposition, after deposition of the monolayer, after the bottom face was rinsed, and then after increasing doses of UV irradiation. During collection of each spectrum, the UV light was turned off. The UV light was generated by a 365 nm light emitting diode flashlight (Tektite) suspended 7 cm above the top of the sample at normal incidence to the TiO_2 surface. Flux at the sample was 1 mW/cm^2. All absorbance spectra were referenced to the either the cleaned sample or the initial solution-prepared monolayer.

Some photoreactions were performed in the infrared spectrometer with a controlled O_2 atmosphere instead of dry air. These experiments were performed with the same method as in dry air, except that the bottom side of the crystal was not rinsed and spectra were collected in *s*-polarization with a ZnSe wire grid polarizer (Molectron). Before the first exposure of UV light, the spectrometer was purged with O_2 (industrial) for a minimum of 2 hr.

Photoreactions were also studied *ex-situ* with scanning tunneling microscopy and x-ray photoelectron spectroscopy. Organic monolayers were prepared in solution on TiO_2 substrates and then loaded into UHV through an oil-free loadlock to be analyzed with STM and XPS. After a sample was loaded into UHV, the load lock was baked to attain UHV conditions, preventing contamination from adsorbed water or other species present after atmospheric exposure. The sample was then returned to the load lock, which was then filled to 1 bar O_2 (ultrahigh purity) and illuminated with UV light through a viewport at normal incidence for variable durations.

STM was performed with tips electrochemically etched from recrystallized tungsten.[13] Tips were cleaned and sharpened with electron bombardment and field-directed sputter sharpening.[14] X-ray photoelectron spectra were collected at variable takeoff angles with a non-monochromatic Mg Kα source. A Tourgaard baseline was subtracted from each spectrum, and a small energy offset (~0.05 eV) was applied to counteract small variations in band bending.[15] X-ray diffraction was performed on a Rigaku Smartlab.

4.5 Results

Rutile Photoreactions. Photoreactions of organic monolayers on rutile TiO_2 were analyzed with infrared spectroscopy. In addition to providing detailed insight into bonding geometry,[10,11,16] infrared spectroscopy can be used to quantify the coverage of molecules on a surface. Figure 4.2(a) shows absorbance spectra of the aromatic C−H stretch region of a benzoate monolayer on rutile TiO_2, where each spectrum has been referenced to the basic-peroxide-cleaned surface. In this region there were a number of vibrations resulting from C−H stretching modes of the phenyl ring of benzoate.[11,16] Absorbance in this case is defined as $A \equiv \log(I_0/I)$, where I and I_0 are the intensity of infrared radiation with and without the

absorbing species, respectively. The absorbance in the aromatic C−H stretch region decreased with increasing UV irradiation time indicating a loss of this species from the surface. By normalizing the integrated absorbance in the aromatic C−H stretch region to that of the initial monolayer, the surface coverage in monolayers of benzoate as a function of UV illumination time was obtained, as shown in Figure 4.2(b).

The observed reaction kinetics deviated significantly from the expected first-order behavior, as seen in Figure 4.2(c), which would result from a constant probability of photoreaction over the course of the reaction, Instead, the rate constant decreased by approximately two orders of magnitude after ~25% of the molecules had reacted. The reaction could be approximately described by a biexponential decay of the form

$$\theta = Ae^{-k_1 t} + (1-A)e^{-k_2 t} ,$$
(Eqn. 4.1)

where θ is surface coverage in monolayers, k_1 and k_2 are the initial and terminal reaction rates, A is the fraction of the species that reacted at rate k_1, and t is the UV illumination time. Increasing the complexity of the fit, such as with a multi-exponential could increase the agreement of the fit, yet we refrained from over-fitting our data without a physical basis for the additional parameters. The best fit of the surface coverage of benzoate on rutile as a function of UV dose to Eqn. 4.1 is shown in Figure 4.2(b). Best fit parameters are shown in Table 4.1. A comparison of the initial to terminal reaction rates shows that the reaction decreased in rate by a factor of 64 after approximately 25% of the monolayer was removed.
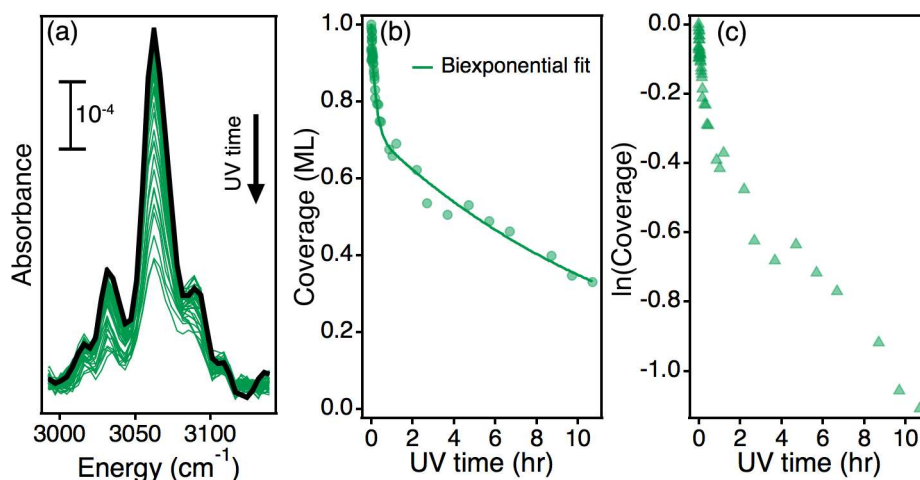
Figure 4.2: (a) Infrared spectrum of the aromatic C−H stretch region of initial benzoate monolayer on rutile (110) in black and as a function of increasing UV illumination time in green. The photoreaction was performed in dry air. (b) The normalized integrated absorbance of the aromatic C−H stretch region as a function of UV illumination time. The fit to a biexponential decay is shown with the solid line. (c) Natural logarithm of normalized integrated absorbance as a function of UV illumination time.

Substrate	Monolayer	Species	A (monolayers)	k_1 (hr^{-1})	k_2 (hr^{-1})	k_1/k_2
Rutile	Benzoate	C−H	0.28	4.6	0.072	64
Rutile	PhPH	C−H	0.34	34	0.10	340
Rutile	PhPH	P−H	0.59	25	0.39	64
Anatase	Benzoate	C−H	0.15	12	0.046	261
Anatase	PhPH	C−H	0.16	8.0	0.048	167
Anatase	PhPH	P−H	0.42	12	0.13	92

Table 4.1 A summary of reaction kinetics measured by *in-situ* infrared spectroscopy in dry air and fit to a biexponential (Eqn. 4.1). PhPH stands for phenylphosphinate.

There are number of possible explanations for the observed biexponential decay of benzoate on rutile. One possibility could be that this behavior results from a specific property of benzoate. Alternatively, this behavior could be explained by variations in the reactivity of molecules bound to different surface sites, for example, if molecules near step edges were more reactive than molecules in the middle of terraces. Another possibility could be that the biexponential reaction kinetics derive from a property of rutile or of TiO$_2$ in general.

To investigate if this biexponential reaction rate is unique to benzoate, the photodecompsition of a solution-deposited monolayer of phenylphosphinate on rutile was studied in the dry-air-purged infrared spectrometer. Figure 4.3(a,b) shows infrared spectra the of P–H and C–H stretching regions in black of

the solution-deposited monolayer of phenylphosphinate on rutile, where each spectrum has been referenced to the basic-peroxide-cleaned surface. The P–H region showed a single broad peak centered at 2376 cm^{-1} and the C–H regions showed several vibrations of H atoms bound to the phenyl ring of phenylphosphinate. Assignments were made based on previous experiments.[11] Both the P–H and C–H stretching vibrations decreased in size as a function of UV irradiation time, representing a loss of these moieties from the surface. Figure 4.3(c) shows the decay of the normalized integrated absorbance of these species, which, similar to benzoate, followed a biexponential trend. Fitting these data to Eqn. 4.1 yielded the rates shown in Table 4.1. A comparison of the initial to terminal rates for C–H and P–H showed that their reaction rates decrease by a factor of 340 and 64 respectively over the course of the reaction. Figure 4.3(c) shows the natural logarithm of the surface coverage of both C–H and P–H as a function of UV dose, where the deviation from linear behavior can be clearly seen. The P−H species reacted more quickly than C−H, with approximately 95% loss after 9.7 hours of UV illumination versus 70% for C−H.
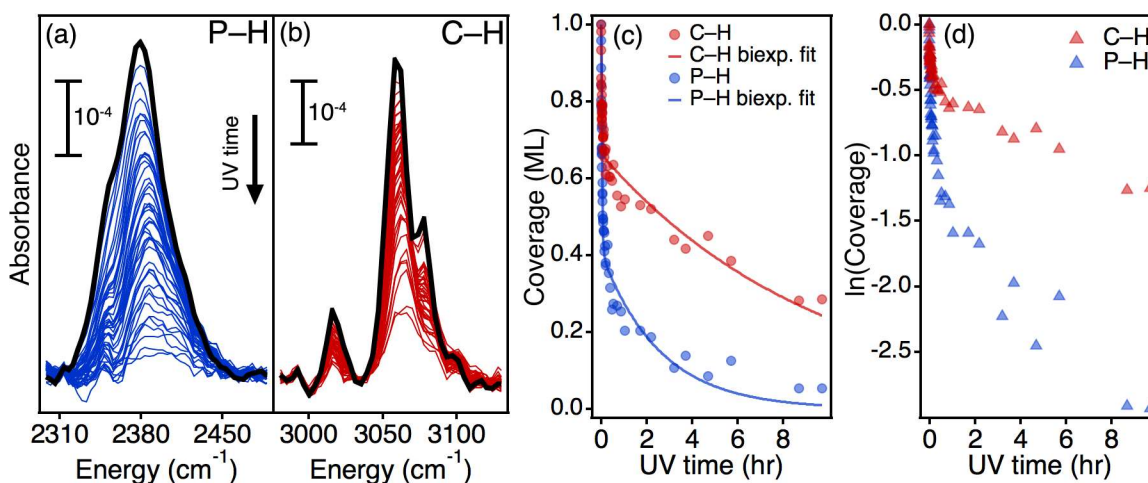
Figure 4.3: (a) Infrared spectrum of the P−H stretch region of initial phenylphosphinate monolayer on rutile (110) in black and as a function of increasing UV dose in blue. (b) Infrared spectrum of the aromatic C−H stretch region of initial phenylphosphinate monolayer on rutile (110) in black and as a function of increasing UV dose in red. (c) The normalized integrated absorbance of both regions as a function of UV illumination time with fits to a biexponential decay shown. (d) Natural logarithm of normalized integrated absorbance for both regions as a function of UV illumination time.

The chemical composition of a phenylphosphinate monolayer on rutile before and after UV illumination in air was characterized with XPS. Figure 4.4(b) shows a comparison of the P $2p$ region of the solution-

prepared monolayer before and after photoreaction in air. The transition at 133.6 eV was assigned to P in solution-deposited phenylphosphinate. After 12 hr UV in dry air the surface showed a P *2p* transition of comparable area, that was shifted 0.89 eV to higher binding energy, consistent most of the P remaining surface-bound and being oxidized to a species with four P–O bonds.[17] Figure 4.4(c) shows a similar comparison of the O 1*s* region, in which the strong transition at 530.4 eV was assigned to O in rutile,[18] and the shoulder that appeared after photoreaction was consistent with O in P–OH,[11] such as in phenylphosphonate or dihydrogen phosphate. The apparent change in size of the rutile O transition is unexpected. This may have resulted from inherent errors in the normalization of the spectra. The XPS spectra were normalized to the integrated intensity of the Ti 2*p* transition as an internal standard; however, the intensity of this transition is affected by the density of surface adsorbates. Different densities of surface adsorbates before and after photoreaction may have caused this apparent increase in the rutile O transition. Finally, Figure 4.4(a) shows a comparison of the C 1*s* region of the solution-prepared monolayer before and after photoreaction in air. The transition at 285.6 eV was assigned to C atoms in phenyl rings, and the satellite at 292.3 eV was assigned to a π-π* transition.[19] The spectrum after photoreaction showed a significantly smaller phenyl C peak and no π-π* transition, consistent with the photodecomposition of the phenyl rings. Additionally a new transition was observed at 289.2 eV, which was assigned to carboxylate or carbonyl C. This transition could be assigned to either bicarbonate formation at empty surface sites[12] – which was difficult to reconcile with lack of loss of P – or the formation of a carbonyl species by oxidation of the phenyl rings.[20] The asymmetry of the transition at 285.6 eV after photoreaction may indicate the formation of C–OH,[20] yet this could not be said conclusively.
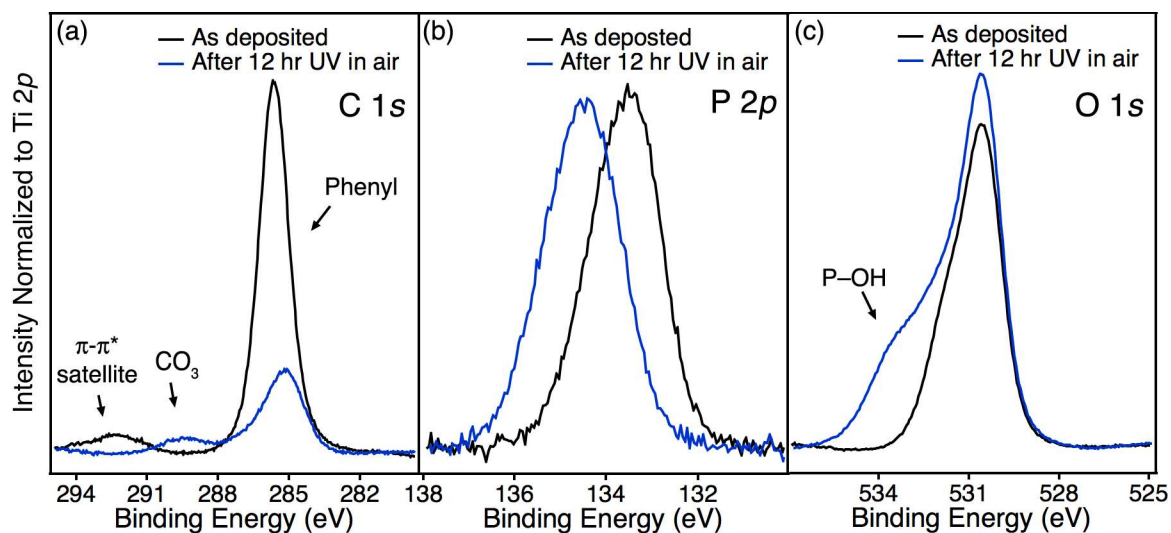
Figure 4.4: XPS spectra of the (a) C 1*s*, (b) P 2*p*, and (c) O 1*s* region for a solution-deposited monolayer of phenylphosphinate on rutile and an equivalently prepared monolayer after 12 hr of UV in air.

Additionally, the chemical composition of benzoate monolayers on rutile (110) before and after photoreaction in 1 bar O_2 was studied with XPS. Figure 4.5(a) shows a comparison the C 1*s* region of a solution-deposited monolayer of benzoate on rutile (110) and after increasing doses of UV irradiation. Based on our prior studies,[10] the transition at 285.5 eV was assigned to C in the phenyl rings, and the transitional at 298.2 eV was assigned to carboxylate C. After UV irradiation in 1 bar O_2 the phenyl C transition decreased in size, indicating the photodecomposition of the phenyl rings. The carboxylate C transition remained largely unchanged, indicating that a monolayer of a carboxylate species remained surface-bound. The small increase in intensity near 298 eV could indicate the formation of a carbonyl species from oxidation of the phenyl rings.[20] Figure 4.5(a) shows a similar comparison for the O 1*s* region. The large transition at 530.4 eV was assigned to O in rutile and the shoulder at 531.9 eV was assigned to carboxylate O. The increase in intensity around 535 eV after 2 hr UV was consistent with the formation of an aromatic C–OH from oxidation of the phenyl rings.[20]
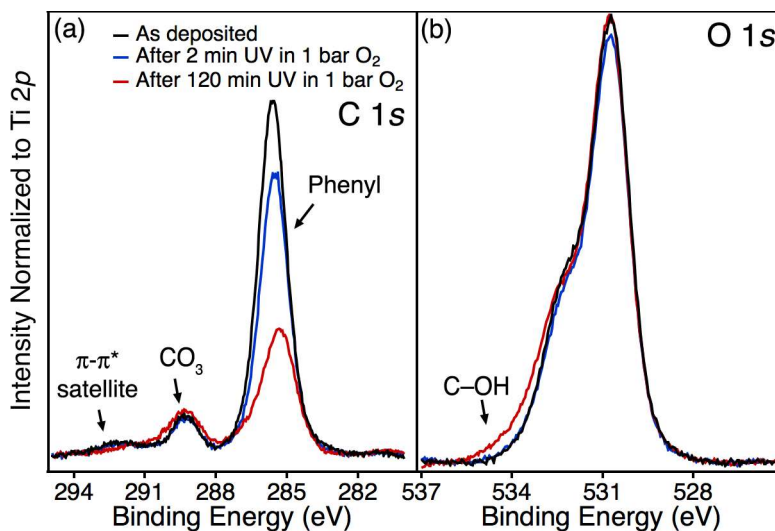
Figure 4.5: XPS spectra of the (a) C 1*s* and (b) O 1*s* region of a solution-deposited monolayer of benzoate on rutile (110) and after 2 and 120 min of UV irradiation in 1 bar O_2.

Anatase Growth. To test whether the biexponential reaction kinetics resulted from a property of rutile, the photoreactivity of organic monolayers on anatase (001) was also studied. Anatase TiO_2 is typically considered to be more reactive than rutile,[21] yet it is only thermodynamically stable at the nanoscale.[22] To provide high quality films of anatase that are both large enough for infrared spectroscopy (~1×1 cm^2) and compatible with surface science techniques such as STM, a hydrothermal heteroepitaxial growth method was developed.

X-ray diffraction (XRD) of the hydrothermally grown film proved that the material grown was anatase (001) and that it was crystallographically aligned with the $SrTiO_3$(100) substrate. The wide 2θ survey in Figure 4.6(a) showed only a peak from anatase (004) and peaks from $SrTiO_3$, where assignments were made by comparison to XRD data of the corresponding powder.[23,24] The absence of other peaks from anatase indicated that the [001] direction of the film was aligned with $SrTiO_3$ [100]. The $SrTiO_3$ substrate showed significantly narrower peaks than the film, indicating that the film is less ordered and aligned than the single crystal substrate. A high-resolution spectrum of $SrTiO_3$ (200) in Figure 4.6(b) showed that this peak occurred at 46.479° with a full width at half maximum (FWHM) of 0.090°. A rocking curve of $SrTiO_3$ (200) shown in Figure 4.6(c) had a FWHM of 0.063°. A high-resolution spectrum of anatase (004)

in Figure 4.6(d) showed that this peak was centered at 38.01° with a FWHM of 0.27°. A rocking curve of

anatase (004) shown in Figure 4.6(e) had a FHWM of 0.96°. The FWHM of these peaks were

representative of the crystallinity and alignment of the materials. The c lattice parameter of the

hydrothermally grown anatase was contracted by 0.52% compared to the lattice parameter of anatase

powder. This matched expectations based on the Poisson effect, where the larger unit cell of $SrTiO_3$

forced the anatase film to expand within the plane of the surface and contract normal to the surface.

 A rotational ϕ scan of the (101) peaks for both anatase and $SrTiO_3$ is shown in Figure 4.7. The alignment

of these peaks from the film and substrate shows that the film is epitaxial and that the {100} and {010}

directions of anatase are aligned with $SrTiO_3$ {010}.
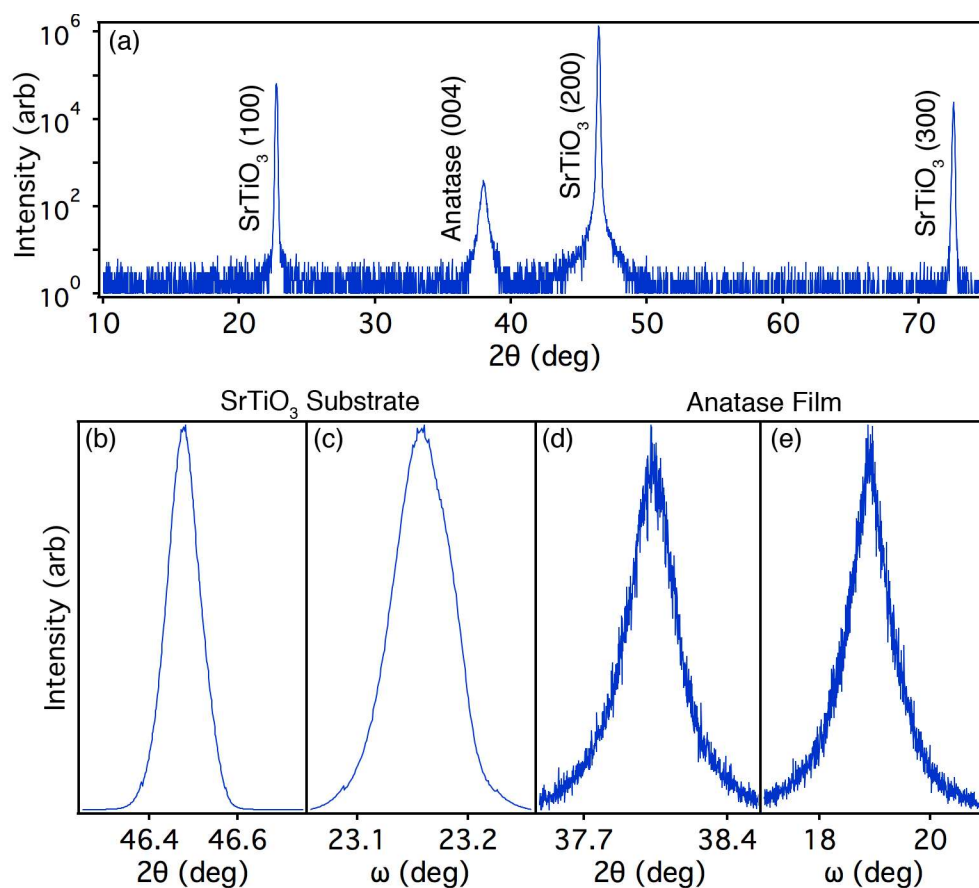
Figure 4.6: (a) Wide 2θ scan of hydrothermally grown anatase film on $SrTiO_3$ (100) substrate. (b) High resolution 2θ scan of substrate $SrTiO_3$ (200) peak and (c) corresponding rocking curve. (d) High resolution 2θ scan of anatase (004) peak and (e) corresponding rocking curve.
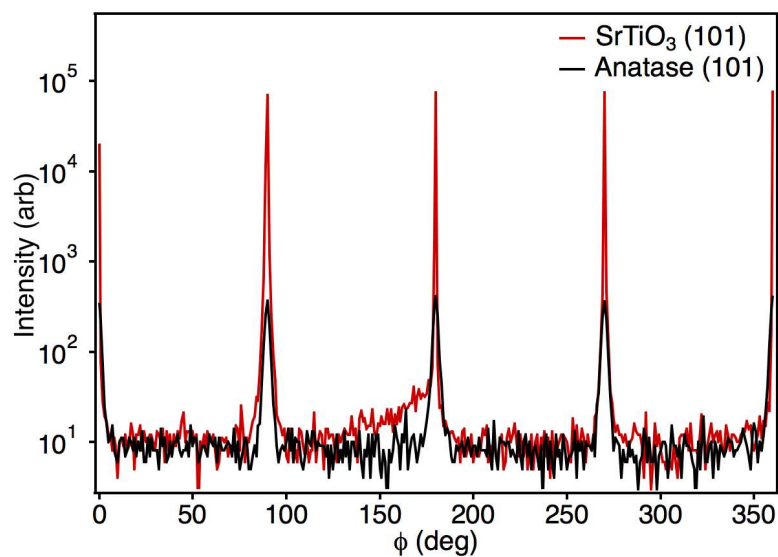
Figure 4.7: Rotational ϕ scan of the (101) peaks for a hydrothermally grown anatase film on a SrTiO$_3$ (100) substrate.

Hydrothermally grown anatase films were smooth and uniform over large length scales. This is demonstrated by the STM images of Figure 4.8, which show the atomically smooth surface of the etched SrTiO$_3$ before growth and an anatase film after solution-deposition of a benzoate monolayer. A high resolution STM of a benzoate monolayer on anatase (001) in Figure 4.9 shows that individual molecules could be resolved.
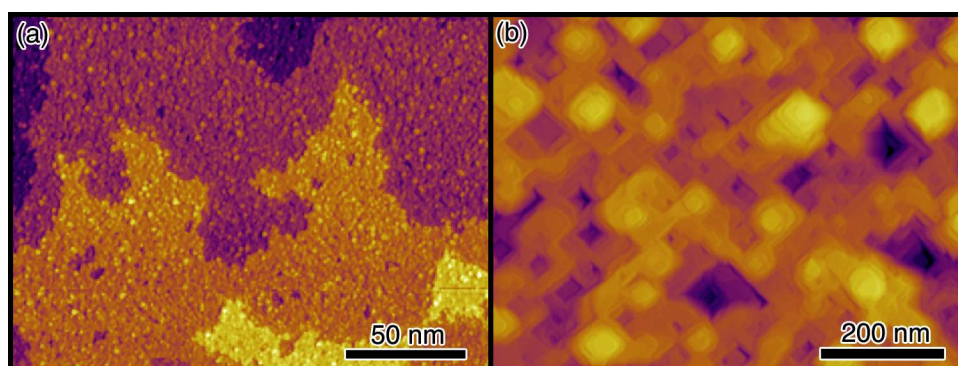
Figure 4.8: (a) STM image of SrTiO$_3$ (100) substrate after etching in basic peroxide. (b) Large scale STM image of anatase (001) film that was hydrothermally grown on SrTiO$_3$ (100) after sputter-and-annealing followed by solution deposition of a benzoate monolayer.
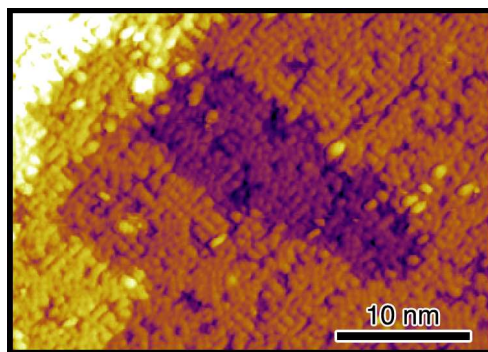
Figure 4.9: High resolution STM image of a solution-deposited monolayer of benzoate on hydrothermally grown anatase (001) film.

Anatase Photoreactions. The photodecomposition kinetics of both benzoate and phenylphosphinate monolayers on anatase in dry air showed biexponential behavior. Infrared spectra of the aromatic C–H and P–H stretch regions are shown for both monolayers referenced to the cleaned anatase surface in Figure 4.10(a-c). The peaks in the aromatic C–H stretch region resulted from H bound to phenyl rings in both monolayers, and the broad peak at 2380 cm^{-1} resulted from H bound to P in phenylphosphinate. The infrared peaks from all three of these species decreased in size as a function of UV irradiation, indicating their loss from the surface following photodecomposition of molecules in the monolayer. The surface coverage of all three species as a function of UV dose was well described by a biexponential decay, and the fits to Eqn. 5.1 are shown in Figure 4.10(d, e) for each case. The best fit parameters are shown in Table 4.1. A comparison of k_1 to k_2 as determined by the fit showed that the reaction rate for C–H in benzoate, C–H in phenylphosphinate, and P–H in phenylphosphinate decreased by a factor of 261, 167, and 92 respectively over the course of the reaction.
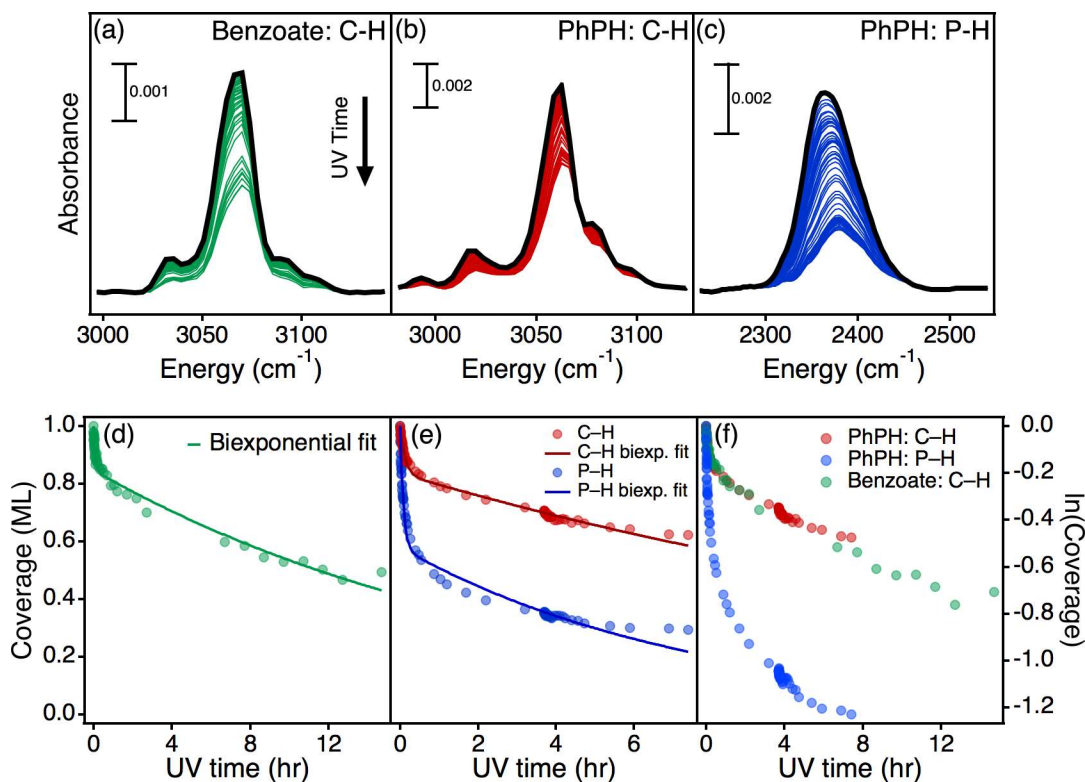
Figure 4.10: (a, b) Infrared spectrum of the aromatic C−H stretch region of initial benzoate (phenylphosphinate) monolayer on anatase (001) in black and as a function of increasing UV irradiation in green (red). (c) Infrared spectrum of the P−H stretch region of initial phenylphosphinate monolayer on anatase (001) in black and as a function of UV irradiation in blue. (d, e) The normalized integrated absorbance of benzoate C–H, phenylphosphinate C–H, and phenylphosphinate P–H as a function of UV illumination time with fits to a biexponential decay. (f) Natural logarithm of normalized integrated absorbance for all three species as a function of UV illumination time.

Controlled Atmosphere Photoreactions. No photodecomposition of benzoate on rutile or anatase was observed in UHV. This is demonstrated in Figure 4.11(a,b), which shows the C $1s$ region in XPS of benzoate monolayers on rutile (110) and anatase (001) before and after 60 and 42 min of UV illumination in UHV, respectively. The transition at 285.5 eV was assigned to phenyl carbon, the peak at 289.2 eV corresponded to carboxylate carbon, and the broad satellite at 292.3 eV was assigned to a π-π* shakeup transition.[19] Both XPS spectra remained largely unchanged after UV illumination, indicating a lack of reactivity in UHV conditions.

Additionally, XPS analysis of phenylphosphinate on rutile showed no detectable reaction after 43 min of UV irradiation in 5×10^{-6} mbar O_2.
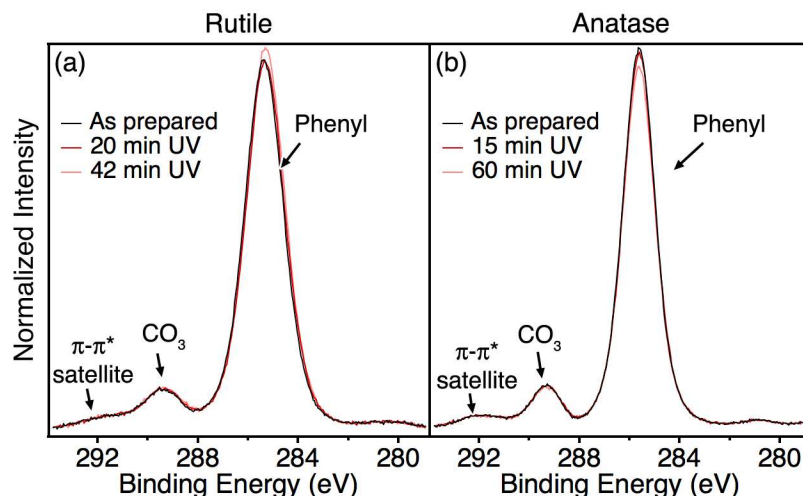
Figure 4.11: High-resolution XPS spectra of the C $1s$ region for a benzoate monolayer on (a) rutile (110) and (b) anatase (001) after increasing doses of UV illumination in UHV.

Performing photoreactions in the infrared spectrometer while purging with O_2 showed that the reaction rate increased with increasing O_2 concentration. Figure 4.12(a) shows the infrared spectra of benzoate on rutile referenced to the initial solution-prepared monolayer as a function of UV dose in either an air or O_2 purge. In these difference spectra, negative aromatic C–H peaks were observed to increase in size with increasing UV illumination time representing a loss of these species from the surface. Figure 4.12(b) shows that the reaction proceeded more quickly in O_2 than in air, with 41% of a monolayer reacted after 50 min UV in O_2 versus 6% after 50 min UV in air. The apparent lower reactivity in these controlled atmosphere experiments may have resulted from the benzoate molecules not being rinsed from the bottom side of the crystal. MIR is sensitive to both the top and bottom of the crystal, but only the molecules on the top were directly exposed to UV. The signal to noise ratio is lower in these spectra due to the data being collected at high resolution and in s-polarization.
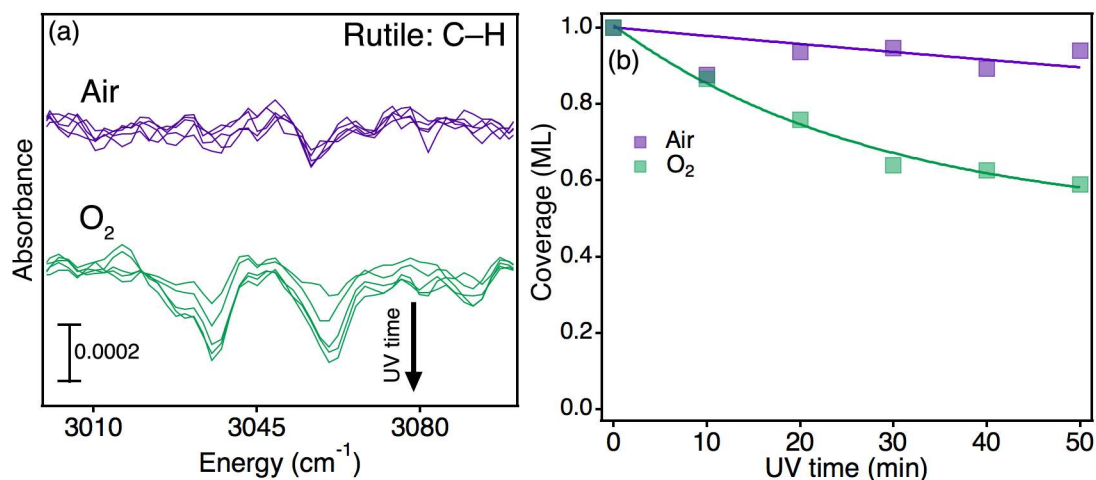
Figure 4.12: (a) Difference infrared spectra of a monolayer of benzoate on rutile referenced to the initial solution-prepared monolayer as a function of increasing UV dose over 50 min UV. Upper and lower spectra were reacted while purging with air or O_2, respectively. (b) Surface coverage of benzoate on rutile as a function of UV time in air or O_2. Single exponential fits are shown as a visual guide.

STM Analysis. In addition to *in-situ* analysis of photoreactivity in the infrared spectrometer, the reacted surface was studied at the molecular scale using STM. Figure 4.13(a) shows a molecular-resolution STM image of a nearly ideal solution-deposited benzoate monolayer as described in Chapter 3. Figure 4.13(b) shows an equivalently prepared benzoate monolayer on rutile, which was illuminated with UV light for 6 min in 1 bar of O_2 before being returned to UHV for imaging in STM. The surface after photoreaction in O_2 showed a number of sites that imaged ~0.3 nm lower in STM, indicating that the molecules in these sites have been either been removed or have photodecomposed to a product that appeared shorter in STM. As the UV dose was increased, the density of regions of lower height increased as seen in Figure 4.13(c, d).

Solution-deposited benzoate monolayer   ...after 6 min UV in 1 bar O$_2$

...after 18 min UV in 1 bar O$_2$ ...after 60 min UV in 1 bar O$_2$
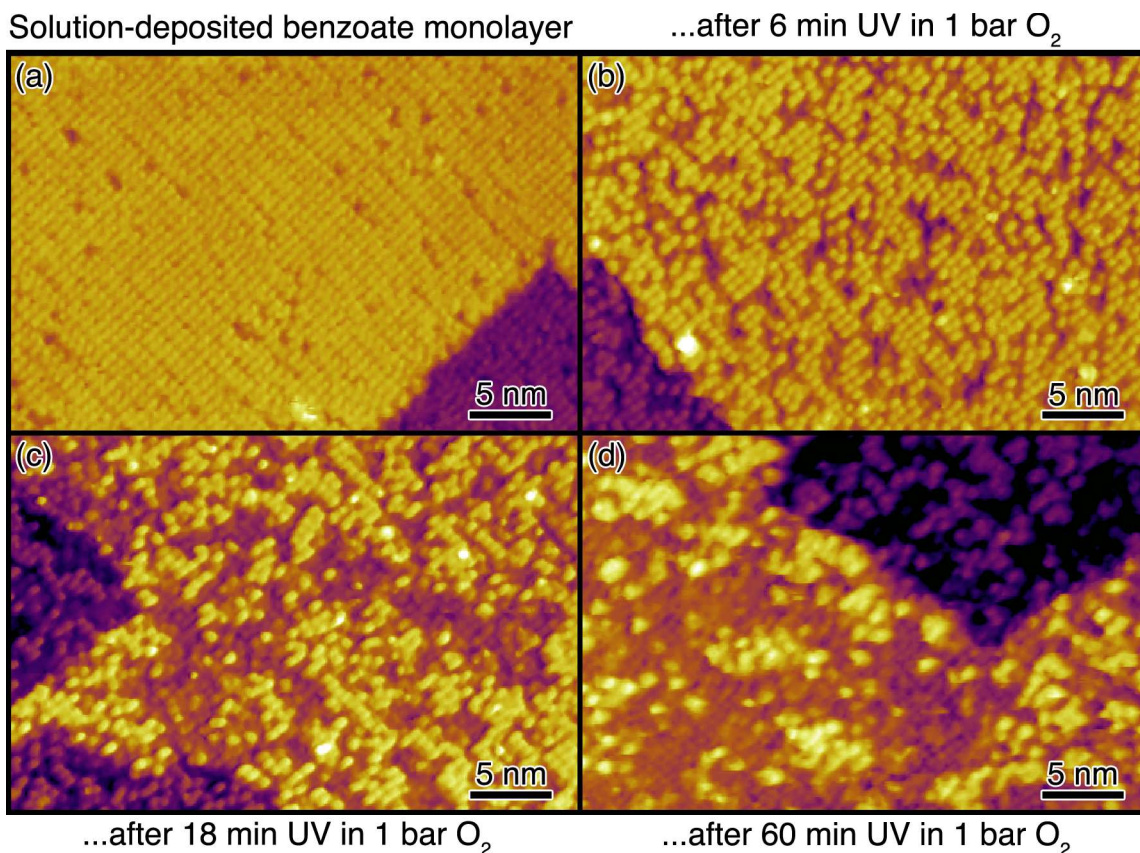
Figure 4.13 Scanning tunneling microscopy images of the photodecomposition of a benzoate monolayer on rutile (110). (a) The initial solution-deposited monolayer. (b-d). Equivalently prepared monolayers of benzoate after 6, 18, 60 min of UV illumination in 1 bar oxygen.

Statistical analysis of the distribution of photoreacted sites was consistent with the photoreaction occurring at random sites on the surface. Figure 4.14(a) shows a Poissonness plot[25] of the distribution of photoreacted benzoate sites after 6 minutes of UV illumination as obtained from Figure 4.14(b). This plot was generated by dividing the STM image of Figure 4.14(b) into 256 equal-sized regions and counting the number of photoreacted molecules in each region, m. The number of times regions were found to have m missing molecules, x_m, was totaled and used to generate the plot. This plotting method was developed by Hoaglin[25] as a way to visually analyze whether data are consistent with a Poisson distribution, which would be expected for an event occurring at random sites on a surface. Data that follow a Poisson distribution yield linear trends, whereas non-random data do not. The highly linear trend observed in Figure 4.14(a) is consistent with the photoreaction occurring at random sites on the surface.
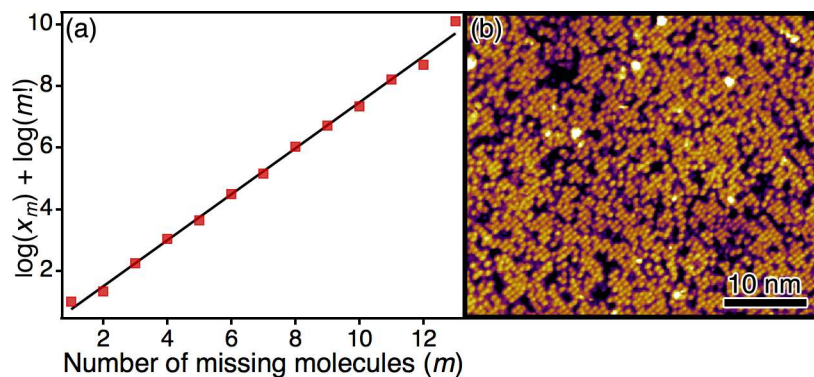
Figure 4.14 (a) Poissoness plot of the distribution of photoreacted sites generated by counting the number of missing molecules in 256 subregions of the STM image shown in (b). Data points shown in red and linear fit in black. (b) An STM image of a benzoate monolayer on rutile after 6 min of UV illumination in 1 bar O_2.

4.5 Discussion

These experiments show that the photodecomposition of organic monolayers on TiO_2 in air follow biexponential kinetics. Freshly deposited monolayers of benzoate or phenylphosphinate on rutile (110) or anatase (001) react quickly under UV illumination in air, but the rate decreases by approximately two orders of magnitude after a fraction of the molecules have reacted.

This phenomenon may represent an important obstacle to the performance of TiO_2 in photocatalytic applications. Many promising applications of TiO_2, such as carbon dioxide photoreduction, are currently too inefficient for widespread adoption. These experiments show that TiO_2 is an effective photocatalyst in the initial stages of a reaction, yet the reactivity of the material significantly decreases in the later stages. If the mechanism of this rate reduction is identified, it may be possible to mitigate or prevent it, in principle increasing the photoreactivity of TiO_2 by up to two orders of magnitude.

Multi-exponential reaction kinetics has been observed for photoreactions on TiO_2 in prior studies; however, previous experiments were performed on TiO_2 particles. [26, 27] The variety of exposed crystallographic faces, phases of TiO_2, and surface conditions made it difficult to determine if the multi-exponential kinetics resulted from multiple first-order reactions occurring simultaneously.

These experiments on well-controlled TiO_2 surfaces indicate that the observed biexponential kinetics likely result from a property of TiO_2 itself. The same biexponential behavior was seen on both benzoate

and phenylphosphinate monolayers reacted on both rutile (110) and antase (001) surfaces of TiO_2, which suggests that this is a ubiquitous property of photoreactions on TiO_2. Statistical analysis of the distribution of photoreacted sites seen in the STM data of benzoate on rutile (110) is consistent with the reaction occurring randomly across the surface. This implies that the cause of the biexponential kinetics is not specific sites on the surface that are inherently more reactive than others. Additionally, in the case of phenylphosphinate monolayers the change in reactivity of both P–H and C–H switches from the initial fast rate to the terminal slow rate concurrently, despite these species having very different initial reactivities. This suggests that the change in reactivity results from a concurrent change in the substrate.

We propose that changes in the magnitude of band bending at the surface of TiO_2 as a result of the photodecomposition of the organic monolayer are responsible for the observed biexponential kinetics. Band bending is a commonly observed phenomenon on semiconductor surfaces, which plays an important role in photoreactions at the surface.[28] The band bending occurs as a result of charge transfer to the surface, either to surface traps or adsorbates. TiO_2 is an *n*-type semiconductor,[29,30] which implies upward band bending at the surface. The accumulation of negative charge on the surface of TiO_2 generates an electric field, which bends the valence and conduction band upward in energy in the near-surface region. There are many previous studies of band bending on TiO_2,[28] and it has been shown that the magnitude of band bending is strongly dependent on the chemical identify of adsorbates.[31] Following absorption of a photon with energy greater than the bandgap, an electron-hole pair is generated. If absorption occurs in the near-surface region where the bands are bent, the electric field will drive the electron toward the bulk and the hole toward the surface as shown in Figure 4.15. Higher magnitudes of band bending indicate stronger electric fields, which increase the photoreactivity of the surface by bringing more holes towards the surface. Holes are believed to initiate oxidation reactions at the surface.[32] We propose that as a result of the partial photodecomposition of the monolayer, the magnitude of band bending decreases with a concomitant decrease in the photoreactivity of the surface. This could result

from photoreaction-induced changes in the energy levels of adsorbates, which allow less charge transfer to surface, decreasing the magnitude of band bending.
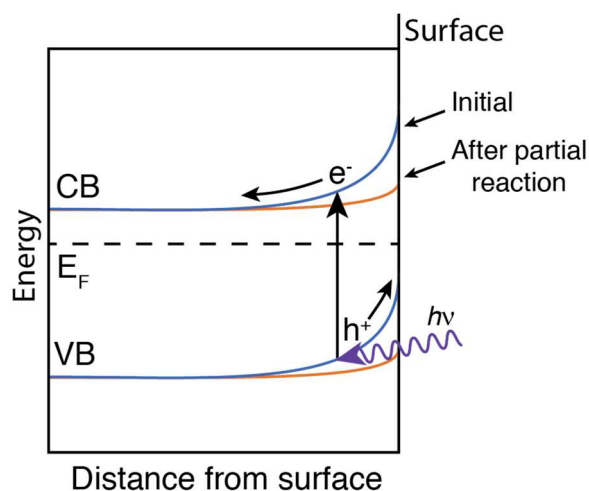
Figure 4.15: A representation of the bending of the valence band (VB) and conduction band (CB) in TiO$_2$ near the surface. The initial magnitude of the band bending is shown in blue and in orange after partial photoreaction. Photogenerated holes (electrons) are pushed towards the surface (bulk) by the electric field near the surface. The Fermi level is labeled by E_F.

Studies are currently underway to directly measure the magnitude of band bending as a function of photoreaction using scanning tunneling spectroscopy. This measurement is complicated by the fact that the electric field from the STM tip results in significant band bending,[33] making it nontrivial to determine the magnitude of unperturbed band bending.

Our data of benzoate photodecomposition are consistent with hole-induced oxidation, in which the final surface-bound product is possibly bicarbonate. The XPS data show that the phenyl rings are photodecomposed, yet a monolayer of carboxylate remains surface-bound. These species are shown in Figure 4.16, which shows the initial structure of benzoate on rutile (110)[10] and the possible surface-bound product of bicarbonate, which bonds to rutile (110) in the same geometry.[12] The role of photogenerated holes in the photodecomposition of organic molecules on TiO$_2$ has been established in previous studies.[32,34,35] The infrared spectroscopy data show that the absorbance in the aromatic C–H stretch region decreases with UV irradiation time, consistent with the photodecomposition of the phenyl rings. The decrease in height of the photoreacted regions observed on rutile is also suggestive of the partial or

complete removal of the phenyl moieties. Decomposition of the phenyl ring is consistent with previous studies of the photodecomposition of benzoate on particles of TiO_2 in an aqueous slurry.[36-38] The final carbonaceous product in these studies was identified by mass spectrometry to be CO_2, with intermediates of hydroxylated benzoic acid. If the benzoate molecules in our study fully decompose to CO_2, this product will not remain surface-bound at room temperature.[39] The resulting exposed surface sites will likely catalyze the formation of surface-bound bicarbonate molecules from CO_2 and H_2O in the air, as we recently demonstrated on rutile (110) surfaces exposed to ambient conditions.[12] Thus, the final surface-bound molecule following the photodecomposition of benzoate on rutile (110) in ambient conditions may be bicarbonate.

The lack of reactivity of benzoate in UHV is consistent with previous studies of the photoreactivity of benzoate on rutile (110) in UHV.[40]

Benzoate (ads)   Bicarbonate (ads)   PhPH (ads)   Dihydrogen phosphate (ads)
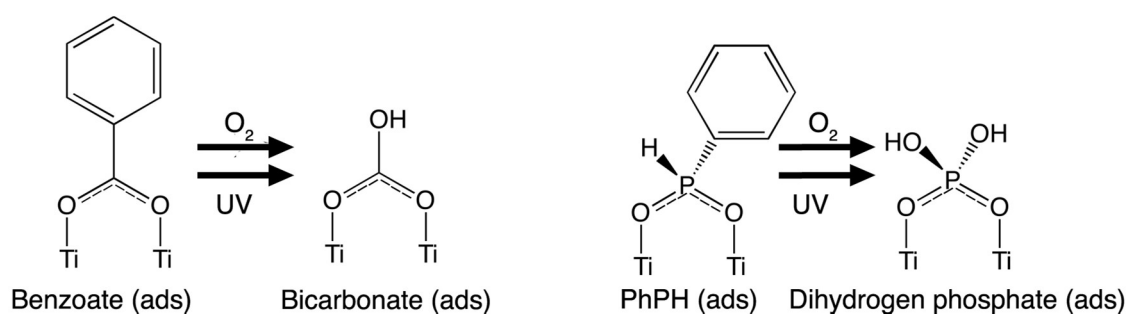
Figure 4.16 Representation of adsorbed benzoate or phenylphosphinate (PhPH) molecules as solution-deposited and the proposed products after UV irradiation in O_2, respectively.

Less is known about the photoreactivity of phosphinates. Our data are consistent with most phosphorous atoms remaining surface-bound and becoming more oxidized, consistent with the possible formation of surface-bound dihydrogen phosphate. Photoreacted phenylphosphinate monolayers on rutile show a P $2p$ transition of comparable integrated intensity to the solution-deposited monolayer, with a binding energy increase of 0.89 eV. This is consistent with most of P remaining on the surface, and becoming oxidized to a surface-bound species with four bonds to O.[17] XPS of the O $1s$ region after photoreaction show the formation of a species containing P–OH. Additionally, our previous studies of STM images of solution-

deposited phenylphosphinate monolayers show that phenylphosphonate (P–OH) species are an oxidative product of phenylphosphinate.[11] This can be seen in the STM image of a solution-deposited monolayer of phenylphosphinate in Figure 4.17, which shows molecules of two different heights. The taller molecules were assigned to phenylphosphonate on the basis of spectroscopic evidence and DFT simulations. On the basis of this data and the loss of both aromatic C–H and P–H seen in infrared spectroscopy, a possible final surface-bound product is dihydrogen phosphate. This possible product is shown in Figure 4.16, as well as the binding geometry of the solution-deposited phenylphosphinate.[11]
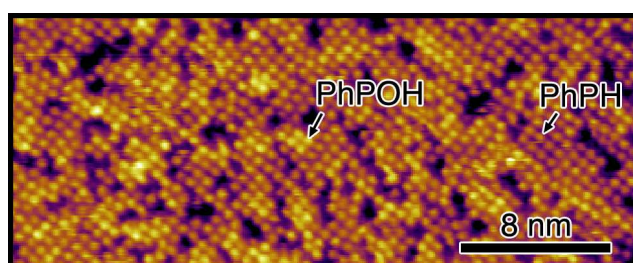
Figure 4.17 STM image of a solution-deposited monolayer of phenylphosphinate on rutile (110) in which some of the molecules were oxidized to phenylphosphonate during aqueous deposition. Phenylphosphonate (PhPOH) appears ~0.05 nm taller than phenylphosphinate (PhPH) in STM.

X-ray diffraction data of our hydrothermally grown anatase films show comparable quality to previous reported films of molecular-beam-epitaxy-grown anatase (001) on SrTiO$_3$ (100), yet we are the first to demonstrate a hydrothermal growth method that provides surfaces smooth enough for use with STM. Previous reports of anatase growth have used a variety of methods, such as molecular-beam epitaxy,[41,42] chemical vapor deposition,[43,44] or hydrothermal growth.[45,46] Our measured FWHM of the anatase (004) rocking curve at 0.96° falls within the range of previously reported values for anatase (001) films on SrTiO$_3$ (0.07 - 1.47°), indicating that the crystallinity and alignment of our films are comparable to other methods. Until now, the only prior reports of STM of anatase grown on SrTiO$_3$ were for films grown with molecular beam epitaxy inside of a UHV chamber.[42] Our demonstration of a hydrothermally grown anatase film that is compatible with STM provides an inexpensive and simple method for studying surface reactions on this material at the molecular scale in the ambient conditions relevant to application.

4.6 Conclusion

Solution-prepared organic monolayers provide an ideal platform for studying the reactivity of metal oxides in technologically relevant, ambient environments. The photodecomposition of benzoate and phenylphosphinate monolayers on rutile (110) and anatase (001) display unusual biexponential reaction kinetics, in which the reaction rates decrease by approximately two orders of magnitude after a fraction of the molecules react. Statistical analysis of the photoreacted benzoate monolayer on rutile (110) are consistent with the reaction occur randomly across the surface, suggesting that the biexponential kinetics does not result from variations in the reactivity of different surface sites. A model involving a decrease in the magnitude of band bending as a result of the photodecomposition of the monolayer is proposed to explain this phenomenon.

[1] Chanmanee, W.; Islam, M. F.; Dennis, B. H.; MacDonnell, F. M. Solar Photothermochemical Alkane Reverse Combustion. *PNAS* **2016**, *113* (10), 2579–2584.

[2] Fujishima, A.; Honda, K. Electrochemical Photolysis of Water at a Semiconductor Electrode. *Nature* **1972**, *238* (5358), 37–38.

[3] Hoffmann, M. R.; Martin, S. T.; Choi, W.; Bahnemann, D. W. Environmental Applications of Semiconductor Photocatalysis. *Chemical Reviews* **1995**, *95* (1), 69–96.

[4] Henderson, M. A.; Lyubinetsky, I. Molecular-Level Insights into Photocatalysis from Scanning Probe Microscopy Studies on $TiO_2(110)$. *Chem. Rev.* **2013**, *113* (6), 4428–4455.

[5] Henderson, M. A. A Surface Science Perspective on Photocatalysis. *Surface Science Reports* **2011**, *66* (6–7), 185–297.

[6] Quah, E. L.; Wilson, J. N.; Idriss, H. Photoreaction of the Rutile $TiO_2(011)$ Single-Crystal Surface: Reaction with Acetic Acid. *Langmuir* **2010**, *26* (9), 6411–6417

[7] Zehr, R. T.; Deskins, N. A.; Henderson, M. A. Photochemistry of 1,1,1-Trifluoroacetone on Rutile TiO_2 (110). *The Journal of Physical Chemistry C* **2010**, *114* (40), 16900–16908.

[8] Ohsawa, T.; Lyubinetsky, I.; Du, Y.; Henderson, M. A.; Shutthanandan, V.; Chambers, S. A. Crystallographic Dependence of Visible-Light Photoactivity in Epitaxial TiO_2 Anatase and Rutile. *Phys. Rev. B* **2009**, *79* (8), 85401.

[9] Kern, W.; Puotinen, D. A. Cleaning Solutions Based on Hydrogen Peroxide for Use in Silicon Semiconductor Technology. *RCA Rev.* **1970**, *31*, 187−206

[10] Skibinski, E. S.; Song, A.; DeBenedetti, W. J. I.; Ortoll-Bloch, A. G.; Hines, M. A. Solution Deposition of Self-Assembled Benzoate Monolayers on Rutile (110): Effect of π–π Interactions on Monolayer Structure. *J. Phys. Chem. C* **2016**, *120* (21), 11581–11589.

[11] Skibinski, E. S.; DeBenedetti, W. J. I.; Hines, M. A. Solution Deposition of Phenylphosphinic Acid Leads to Highly Ordered, Covalently Bound Monolayers on TiO_2 (110) Without Annealing. *J. Phys. Chem. C* **2017**, *121* (26), 14213–14221.

[12] Song, A.; Skibinski, E. S.; DeBenedetti, W. J. I.; Ortoll-Bloch, A. G.; Hines, M. A. Nanoscale Solvation Leads to Spontaneous Formation of a Bicarbonate Monolayer on Rutile (110) under Ambient Conditions: Implications for CO_2 Photoreduction. *J. Phys. Chem. C* **2016**, *120* (17), 9326–9333.

[13] Greiner, M.; Kruse, P. Recrystallization of Tungsten Wire for Fabrication of Sharp and Stable Nanoprobe and Field-Emitter Tips. *Review of Scientific Instruments* **2007**, *78* (2), 26104.

[14] Schmucker, S. W.; Kumar, N.; Abelson, J. R.; Daly, S. R.; Girolami, G. S.; Bischof, M. R.; Jaeger, D. L.; Reidy, R. F.; Gorman, B. P.; Alexander, J.; *et al*. Field-Directed Sputter Sharpening for Tailored Probe Materials and Atomic-Scale Lithography. *Nature Communications* **2012**, *3*, 935.

[15] Gleason-Rohrer, D. C.; Brunschwig, B. S.; Lewis, N. S. Measurement of the Band Bending and Surface Dipole at Chemically Functionalized Si(111)/Vacuum Interfaces. *J. Phys. Chem. C* **2013**, *117* (35), 18031–18042.

[16] DeBenedetti, W. J. I.; Skibinski, E. S.; Hinckley, J. A.; Nedessa, S. B.; Hines, M. A. Cartesian Decomposition of Infrared Spectra Reveals the Structure of Solution-Deposited, Self-Assembled Benzoate and Alkanoate Monolayers on Rutile (110). *J. Phys. Chem. C* **2016**, *120* (43), 24866–24876.

[17] Luschtinetz, R.; Frenzel, J.; Milek, T.; Seifert, G. Adsorption of Phosphonic Acid at the TiO_2 Anatase (101) and Rutile (110) Surfaces. *J. Phys. Chem. C* **2009**, *113* (14), 5730–5740.

[18] Diebold, U.; Madey, T. E. TiO_2 by XPS. *Surface Science Spectra* **1996**, *4* (3), 227–231.

[19] Rennie, E. E.; Kempgens, B.; Köppe, H. M.; Hergenhahn, U.; Feldhaus, J.; Itchkawitz, B. S.; Kilcoyne, A. L. D.; Kivimäki, A.; Maier, K.; Piancastelli, M. N.; *et al*. A Comprehensive Photoabsorption, Photoionization, and Shake-up Excitation Study of the C $1s$ Cross Section of Benzene. *The Journal of Chemical Physics* **2000**, *113* (17), 7362–7375.

[20] Gattrell, M.; Kirk, D. W. A Study of the Oxidation of Phenol at Platinum and Preoxidized Platinum Surfaces. *J. Electrochem. Soc.* **1993**, *140* (6), 1534–1540.

[21] Watanabe, T.; Nakajima, A.; Wang, R.; Minabe, M.; Koizumi, S.; Fujishima, A.; Hashimoto, K. Photocatalytic Activity and Photoinduced Hydrophilicity of Titanium Dioxide Coated Glass. *Thin Solid Films* **1999**, *351* (1), 260–263.

[22] Shannon, R. D.; Pask, J. A. Kinetics of the Anatase-Rutile Transformation. *Journal of the American Ceramic Society* **1965**, *48* (8), 391–398.

[23] Howard, C. J.; Sabine, T. M.; Dickson, F. Structural and Thermal Parameters for Rutile and Anatase. *Acta. Cryst. B*. **1991**, 47 (4), 462–468.

[24] Mitchell, R. H.; Chakhmouradian, A. R.; Woodward, P. M. Crystal Chemistry of Perovskite-Type Compounds in the Tausonite-Loparite Series, $(Sr_{1-2x}Na_xLa_x)TiO_3$. *Phys Chem Min* **2000**, *27* (8), 583–589.

[25] Hoaglin, D. C. A Poissonness Plot. *The American Statistician* **1980**, *34* (3), 146–149.

[26] Bahnemann, D.; Henglein, A.; Spanhel, L. Detection of the Intermediates of Colloidal TiO_2 -Catalysed Photoreactions. Faraday Discussions of the Chemical Society **1984**, 78 (0), 151–163.

[27] Yamakata, A.; Ishibashi, T.; Onishi, H. Kinetics of the Photocatalytic Water-Splitting Reaction on TiO_2 and Pt/TiO_2 Studied by Time-Resolved Infrared Absorption Spectroscopy. Journal of Molecular Catalysis A: Chemical **2003**, 199 (1), 85–94.

[28] Zhang, Z.; Yates, J. T. Band Bending in Semiconductors: Chemical and Physical Consequences at Surfaces and Interfaces. *Chem. Rev.* **2012**, *112* (10), 5520–5551.

[29] Breckenridge, R. G.; Hosler, W. R. Electrical Properties of Titanium Dioxide Semiconductors. *Phys. Rev.* **1953**, *91* (4), 793–802.

[30] Forro, L.; Chauvet, O.; Emin, D.; Zuppiroli, L.; Berger, H.; Lévy, F. High Mobility *n*-type Charge Carriers in Large Single Crystals of Anatase (TiO₂). *Journal of Applied Physics* **1994**, *75* (1), 633–635.

[31] Stevanovic, A.; Büttner, M.; Zhang, Z.; Yates, J. T. Photoluminescence of TiO_2: Effect of UV Light and Adsorbed Molecules on Surface Band Structure. *J. Am. Chem. Soc.* **2012**, *134* (1), 324–332.

[32] Fox, M. A. Organic Heterogeneous Photocatalysis: Chemical Conversions Sensitized by Irradiated Semiconductors. *Acc. Chem. Res.* **1983**, *16* (9), 314–321.

[33] Feenstra, R. M.; Dong, Y.; Semtsiv, M. P.; Masselink, W. T. Influence of Tip-Induced Band Bending on Tunneling Spectra of Semiconductor Surfaces. *Nanotechnology* **2007**, *18* (4), 044015.

[34] Kraeutler, B.; Bard, A. J. Heterogeneous Photocatalytic Synthesis of Methane from Acetic Acid - New Kolbe Reaction Pathway. *J. Am. Chem. Soc.* **1978**, *100* (7), 2239–2240.

[35] Henderson, M. A. Photooxidation of Acetone on TiO_2(110): Conversion to Acetate via Methyl Radical Ejection. *J. Phys. Chem. B* **2005**, *109* (24), 12062–12070.

[36] Ajmera, A. A.; Sawant, S. B.; Pangarkar, V. G.; Beenackers, A. C. M. Solar-Assisted Photocatalytic Degradation of Benzoic Acid Using Titanium Dioxide as a Photocatalyst. *Chem. Eng. Technol.* **2002**, *25* (2), 173–180.

[37] Izumi, I.; Fan, F.-R. F.; Bard, A. J. Heterogeneous Photocatalytic Decomposition of Benzoic Acid and Adipic Acid on Platinized Titanium Dioxide Powder. The Photo-Kolbe Decarboxylative Route to the Breakdown of the Benzene Ring and to the Production of Butane. *J. Phys. Chem.* **1981**, *85* (3), 218–223.

[38] Velegraki, T.; Mantzavinos, D. Conversion of Benzoic Acid during TiO_2-Mediated Photocatalytic Degradation in Water. *Chemical Engineering Journal* **2008**, *140* (1), 15–21.

[39] Thompson, T. L.; Diwald, O.; Yates, J. T. CO_2 as a Probe for Monitoring the Surface Defects on TiO_2 (110)Temperature-Programmed Desorption. *J. Phys. Chem. B* **2003**, *107* (42), 11700–11704.

[40] Landis, E. C.; Jensen, S. C.; Phillips, K. R.; Friend, C. M. Photostability and Thermal Decomposition of Benzoic Acid on TiO_2. *J. Phys. Chem. C* **2012**, *116* (40), 21508–21513.

[41] Ong, C. K.; Wang, S. J. *In-situ* RHEED Monitor of the Growth of Epitaxial Anatase TiO_2 Thin Films. *Applied Surface Science* **2001**, *185* (1), 47–51.

[42] Du, Y.; Kim, D. J.; Kaspar, T. C.; Chamberlin, S. E.; Lyubinetsky, I.; Chambers, S. A. *In-situ* Imaging of the Nucleation and Growth of Epitaxial Anatase TiO_2(001) Films on $SrTiO_3$(001). *Surface Science* **2012**, *606* (17), 1443–1449.

[43] Tokita, S.; Tanaka, N.; Saitoh, H. High-Rate Epitaxy of Anatase Films by Atmospheric Chemical Vapor Deposition. *Jpn. J. Appl. Phys.* **2000**, *39* (2B), L169.

[44] Chen, S.; Mason, M. G.; Gysling, H. J.; Paz-Pujalt, G. R.; Blanton, T. N.; Castro, T.; Chen, K. M.; Fictorie, C. P.; Gladfelter, W. L.; Franciosi, A.; *et al.* Ultrahigh Vacuum Metalorganic Chemical Vapor Deposition Growth and in Situ Characterization of Epitaxial TiO_2 Films. *Journal of Vacuum Science & Technology A: Vacuum, Surfaces, and Films* **1993**, *11* (5), 2419–2429.

[45] Zhang, Z. A Low-Temperature and Low-Cost Method to Produce High-Quality Epitaxial Anatase TiO_2 Thin Films. *Journal of Materials Research* **2005**, *20* (2), 292–294.

[46] Chan, K. Y. S.; Goh, G. K. L. Solution Epitaxy of TiO_2 Thin Films. *J. Electrochem. Soc.* **2009**, *156* (7), D231–D235.

Chapter 5

Frustrated Etching during H/Si(111) Methoxylation produces Fissured Fluorinated Surfaces, whereas Direct Fluorination Preserves the Atomically Flat Morphology[†]

Erik S. Skibinski,[1] William J. I. DeBenedetti,[1] Sara M. Rupich,[2] Yves J. Chabal,[2] and Melissa A.

Hines[1]

[1]Dept. of Chemistry and Chemical Biology, Cornell University, Ithaca NY 14853-1301 USA

[2]Dept. of Materials Science and Engineering, Univ. of Texas at Dallas, Richardson TX 75080

USA

5.1 Abstract

Two solution-based strategies for the preparation of partially fluorinated Si(111) surfaces from H/Si(111) were investigated using a combination of scanning tunneling microscopy, x-ray photoemission spectroscopy, infrared spectroscopy, and kinetic Monte Carlo simulations. Direct fluorination of H/Si(111) with HF (aq) produced atomically flat surfaces with 11% fluorination. A two-step reaction that first methoxylated the surface by reaction in methanol then converted the methoxy-termination to F-termination by reaction in HF (aq) produced atomically rough, fissured surfaces with 24% fluorination. The atomic-scale roughness was induced by the methoxylation reaction. Methanol was shown to react with H/Si(111) surfaces through two parallel mechanisms: an etching reaction and a methoxylation reaction. The methoxylation reaction locally inhibited or "frustrated" the etching reaction, leading to the development of a characteristic fissured morphology. The H and F atoms on the fluorinated surface were imaged with atomic resolution, and no evidence of the previously proposed nanopatterning mechanism was observed.

Keywords

scanning tunneling microscopy, methanol, silicon, etching, functionalization

5.2 Introduction

Silicon functionalization — the covalent attachment of a high density of organic molecules to a silicon surface — is a prerequisite for many envisioned and emerging technologies, including chemical and biological sensors and next-generation photovoltaics. Many of these applications require high electronic performance of the silicon/organic interface, which means that silicon oxidation must be scrupulously avoided during functionalization. As a result, an ideal functionalization reaction cannot oxidize even a small percentage of the surface.

The two most established techniques for the formation of robust, high quality monolayers start with an atomically flat, hydrogen-terminated Si(111) surface prepared by anisotropic etching in an aqueous solution.[1–3] The flat H/Si(111) surface is then functionalized by either direct reaction with a 1-alkene[4–10] or by a two-step reaction that uses a Grignard reagent to functionalize a pre-chlorinated surface.[11–17] While both approaches produce flat Si(111) surfaces terminated by high quality alkyl monolayers, the reactions have a limited scope and cannot be used to produce all desired organic terminations on unoxidized silicon.

Activating an atomically flat H/Si(111) surface by replacing all or most of the terminating H atoms with hydroxyl (–OH) groups would dramatically expand our repertoire of silicon functionalization reactions by enabling the use of a wide variety of condensation (dehydration) reactions developed for the functionalization of glass and silica surfaces. Despite many attempts, the preparation of an unoxidized, hydroxylated silicon surface outside of an ultrahigh vacuum chamber has proven elusive. For example, the reaction of (deoxygenated) H_2O with silicon simply etches the surface, regenerating the H-termination in the process.[18–21] Although more aggressive reagents, such as aqueous bases[22,23] or H_2O_2,[24] produce surface silanol groups, they also react with silicon backbonds and partially oxidize the underlying substrate.

Michalak *et al.*[25] recently filled this synthetic void with a three-step synthesis of a "nanopatterned" Si(111) surface in which 1/3 of the H atoms on an atomically flat H/Si(111) surface are replaced by –OH groups with no interfacial oxidation. The key to this reaction is the first step: the methoxylation of H/Si(111) by direct reaction with anhydrous methanol.[26,27] Michalak *et al.* proposed that the steric bulk of the adsorbed methoxy group (–OCH$_3$) prevents methoxylation of adjacent sites and favors the formation of a periodic "nanopattern" as shown in Figure 5.1. In the remaining two steps of the synthesis, the methoxy groups are first replaced with F by immersion in concentrated HF (aq), then the F atoms are replaced with OH by immersion in H$_2$O.
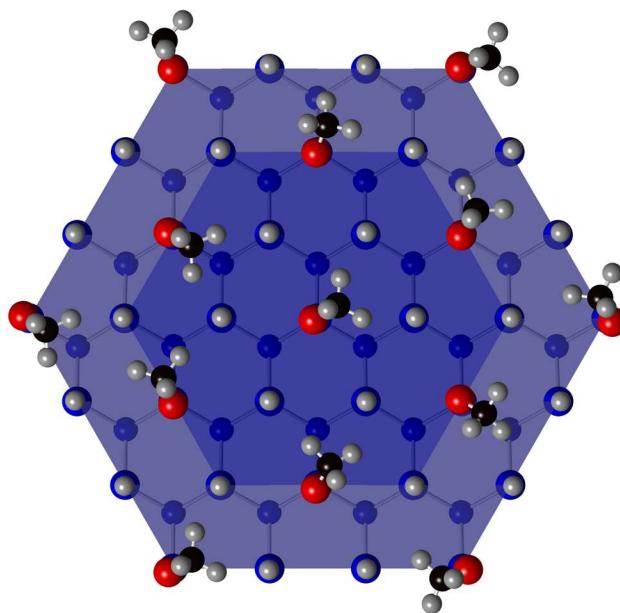
Figure 5.1: Nanopatterned arrangement of methoxy groups on H/Si(111) proposed by Michalak *et al.*[25] The steric bulk and near-free rotation of the methoxy groups around the vertical axis prevents the adsorption of methoxy groups at adjacent sites. In their model, each CH$_3$O/H group is surrounded by 6 nearest neighbor H/CH$_3$O groups, respectively. Si, H, C, and O atoms are represented by blue, gray, black, and red spheres, respectively.

Michalak *et al.* inferred the existence of a hexagonal nanopattern on their fluorinated surface from its infrared absorption spectrum, which reportedly showed "quantized" increases in the energy of the Si–H stretch vibration with increasing F coverage.[25,28] The energy of the Si–H stretch vibration is known to be sensitive to inductive effects.[29] Because of this, nearby electronegative atoms, such as O, Cl, or F, lead to readily detectable increases (or "blue shifts") in the energy of the Si–H stretch vibration.[30–32] DFT

calculations[25] suggest a linear relationship between the energy of the Si–H stretch vibration and the number of nearest-neighbor F atoms, with the calculated mode energy increasing by 15 cm^{-1} as the number of nearest neighbor F atoms increases from 0 to 3. Consistent with this prediction, the energy of the Si–H stretch mode increased from 2079.4 cm^{-1} on the initial H/Si(111) surface to 2092.4 cm^{-1} on the nanopatterned F/Si(111) surface.[25]

In this manuscript, we first show that silicon methoxylation is more complicated than initially realized, consisting of parallel etching and functionalization reactions. The functionalization reaction locally inhibits or "frustrates" the etching reaction. As a result, methoxylation transforms an initially flat H/Si(111) surface into a nanostructured surface characterized by relatively straight vicinal steps and fissured terraces. Fluorination of this surface by immersion in HF produces a surface with 24% F termination, somewhat less than the 33% reported by Michalak *et al.*;[25] however, the F atoms show no evidence of the proposed hexagonal nanopattern.

Second, we demonstrate a much faster and simpler means of fluorinating a H/Si(111) surface: immersion in concentrated HF at room temperature. This reaction leads to direct replacement of H by F with no surface etching or oxidation. The reaction occurs randomly across the surface and also does not form a nanopattern. The partially fluorinated surface is atomically flat and fluorination densities as high as 11% are demonstrated. Although this reaction produces somewhat less fluorination than the methanol pathway, the superior surface morphology may be advantageous for some applications. Further optimization of the reaction conditions (*e.g.,* temperature, concentration) may increase the fluorination density.

Once fluorinated by either strategy, Michalak, *et al.*[25] have shown that the F atoms can be replaced with hydroxyl groups by a H_2O immersion, producing an unoxidized, hydroxyl-terminated Si(111) surface that is an ideal starting point for a wide variety of functionalization reactions.

Like most silicon functionalization reactions, the reactions studied here do not functionalize every site on the surface, and the degree of functionalization is a point under study. In the following, we will follow

convention and refer to "methoxylated" or "fluorinated" surfaces, which will be abbreviated as CH$_3$O/Si(111) and F/Si(111); however, many of the surface sites will remain H-terminated.

5.3 Experimental and Computational

Experimental Methods. STM samples were diced from B-doped $0.5 - 5.0$ Ω cm Si(111) miscut by $0.45°$ towards $\langle 11\bar{2} \rangle$. Samples for infrared analysis were diced from float-zone Si(111) wafers miscut by $9°$ towards $\langle \bar{1}\bar{1}2 \rangle$.

Immediately prior to use, all labware underwent a modified RCA clean.[33] To remove organic contamination, the labware was immersed in an SC-1 bath consisting of 1:1:5 by volume of 30% H$_2$O$_2$ (aq, J.T. Baker, CMOS grade): 28% NH$_3$ (aq, BDH, ACS grade): ultrapure H$_2$O (Milli-Q) for 10 min at 80°C. The labware was thoroughly rinsed with ultrapure H$_2$O, then immersed in an SC-2 bath consisting of 1:1:5 by volume of 30% H$_2$O$_2$ (aq): 37% HCl (aq, BDH, ACS grade): ultrapure H$_2$O for 10 min at 80°C to remove metallic contamination.

Hydrogen-terminated samples were prepared in air using the following procedure. Silicon samples were cleaned with a fresh SC-1 solution for 10 min at 80°C, rinsed with ultrapure H$_2$O, then cleaned with another fresh SC-1 solution for 10 min at 80°C. To remove the oxide, silicon samples were immersed for 30 s in 5:1 buffered oxide etch (a solution of HF and NH$_4$F, J.T. Baker, CMOS grade) at room temperature. Following oxide removal, samples were rinsed in H$_2$O, then etched in 40% NH$_4$F (aq, J.T. Baker, CMOS grade) for 15 min to produce an atomically smooth H-terminated surface. Samples were rinsed twice in separate aliquots of H$_2$O for 3 s each. For the surfaces with a $9°$ miscut towards the $\langle \bar{1}\bar{1}2 \rangle$ direction, samples were cleaned in the same manner as above, but the etching process was modified. The samples were immersed in 25% HF for 30 s, immediately followed by a 20 s immersion in 40% NH$_4$F. Samples were rinsed twice in separate aliquots of H$_2$O for 3 s each.

Methoxylated samples were prepared in an oxygen-free glovebox by immersing a smooth H-terminated surface in anhydrous methanol (99.8%, Sigma Aldrich) contained in a sealed Teflon vial heated to 65°C in

a dry heat bath. For studies of short reaction times ($\leq$ 30 min), silicon samples were transferred into preheated vials of methanol, whereas longer reactions started with room temperature methanol. After methoxylation, samples were removed from solution and allowed to dry in air before further use. To test for possible side reactions with dissolved O_2,[34,35] some experiments were performed with methanol that was pre-sparged with ultrahigh purity N_2; however, no effect was observed.

Fluorination was performed by immersing H-terminated or methoxylated samples into 49% HF (aq, J.T. Baker, CMOS grade) for varying times. Dissolved oxygen in the HF (aq) was removed by storing the HF (aq) in ultrahigh purity N_2 without agitation for 7 hr immediately prior to use.

Once prepared, samples were quickly transferred (within approximately 5 min) to an oil-free load lock on an ultrahigh vacuum chamber for characterization with scanning tunneling microscopy (STM) and X-ray photoemission spectroscopy (XPS, Supporting Information). The STM tips were electrochemically etched from recrystallized tungsten[36] and prepared with field-directed sputter sharpening.[37] Alternatively, the samples were transferred to a dry-air-purged infrared spectrometer where unpolarized radiation incident at 74° from the surface normal was used to obtain a transmission spectrum at 4 cm^{-1} resolution. The reported spectra are either referenced to an oxidized sample prepared by an SC-1 clean or presented as differential spectra.

Kinetic Monte Carlo Model. The simultaneous etching and methoxylation reactions were modeled using the atomistic, chemically realistic kinetic Monte Carlo (KMC) model described in Refs. [38] and [39]. To match STM experiments, the initial surface was assumed to be entirely H-terminated with equally spaced, atomically straight vicinal steps corresponding to a miscut of 0.5° in the $\langle 11\bar{2} \rangle$ direction, a miscut that yields monohydride-terminated vicinal steps. Simulated surfaces were typically ~200 nm × 200 nm in extent, containing ~10^6 Si atoms. Screw bounds were used to simulate an infinite surface.

The model reported here allowed for two site-specific reactions of H-terminated silicon atoms: etching (removal of the Si atom) and methoxylation. Any "dangling bonds" created by the etching reaction were

assumed to be immediately terminated by hydrogen. Once methoxylated, a surface site became unreactive; it would not etch or de-methoxylate. (This assumption could be relaxed to enable testing of alternate mechanisms.) Diffusion of silicon atoms and methoxylate adsorbates, redeposition of etched silicon from solution, and undercutting reactions were forbidden. The latter three assumptions are well justified for aqueous etching in the presence of alcohol as discussed in Refs. 38–40.

The rates of the site-specific reactions were user-controlled parameters that were determined by comparison to experimental morphologies.[3,39,41] On the basis of previous investigations of the reactivity of H/Si(111) in a variety of solutions,[3,38,40] five different reactive sites were included in the simulation: kinks, points, dihydride-terminated steps, monohydride-terminated steps, and terrace sites. Two additional reactive sites which must exist at least transiently during etching, trihydrides and strained horizontal dihydrides, have never been observed experimentally and were assumed to etch immediately upon formation.

During the simulation, random sites were either etched or methoxylated in accordance with the user-specified, site-specific reaction rates using the previously described algorithm.[38] Because the methoxylation reaction was irreversible, and methoxylated sites could not etch, the reaction continued until all sites on the surface were methoxylated then stopped. The final morphologies are reported.

Simulations of STM Images. STM images of isolated F and CH_3O adsorbates on otherwise H-terminated Si(111) surfaces were modeled using 2×2 periodically repeating slabs consisting of 4 silicon bilayers terminated by H on the backside and separated by a 13 Å vacuum spacing (Supporting Information). During geometric optimization, the positions of the bottommost Si bilayer and its terminating H atoms were fixed.

Calculations were performed using density functional theory (DFT) within the generalized-gradient-approximation[42] (GGA) with the Perdew, Burke, and Ernzerhof (PBE) exchange-correlation functional,[43] as implemented in the Vienna *ab initio* simulation package (VASP).[44–47] The electron-ion interaction was described using the projector augmented wave (PAW) method of Blöchl.[48,49] Electronic states were

expanded in plane waves with a kinetic energy cutoff of 400 eV and a $7 \times 7 \times 1$ Monkhorst-Pack grid of k points. Brillouin-zone integration was performed using the tetrahedron method with Blöchl corrections.[50]

STM images were modeled within the Tersoff-Hamann approximation[51] as isosurfaces of constant local density of states at an energy equal to the tip-surface bias measured with respect to the surface Fermi energy as implemented in bSkan.[52,53]

5.4 Results

Methoxylation of H/Si(111) with CH$_3$OH. Comparison of STM images before and after reaction with methanol showed that the methoxylation reaction etched the surface. The initial H-terminated surfaces were characterized by atomically smooth terraces separated by atomically straight steps, as shown in Figure 5.2(a). Two changes were observed after reaction in methanol for 30 min as shown in Figure 5.2(b). (Complete methoxylation requires a ~12 hr immersion.[27]) First, the atomically straight steps became ragged with numerous indentations. Second, the initially flat terraces became pockmarked with both shallow "depressions" and monolayer-deep etch pits with irregular edges. We attributed the shallow depressions to individual methoxy groups due to the insulating nature of the methoxy group (*vide infra*).
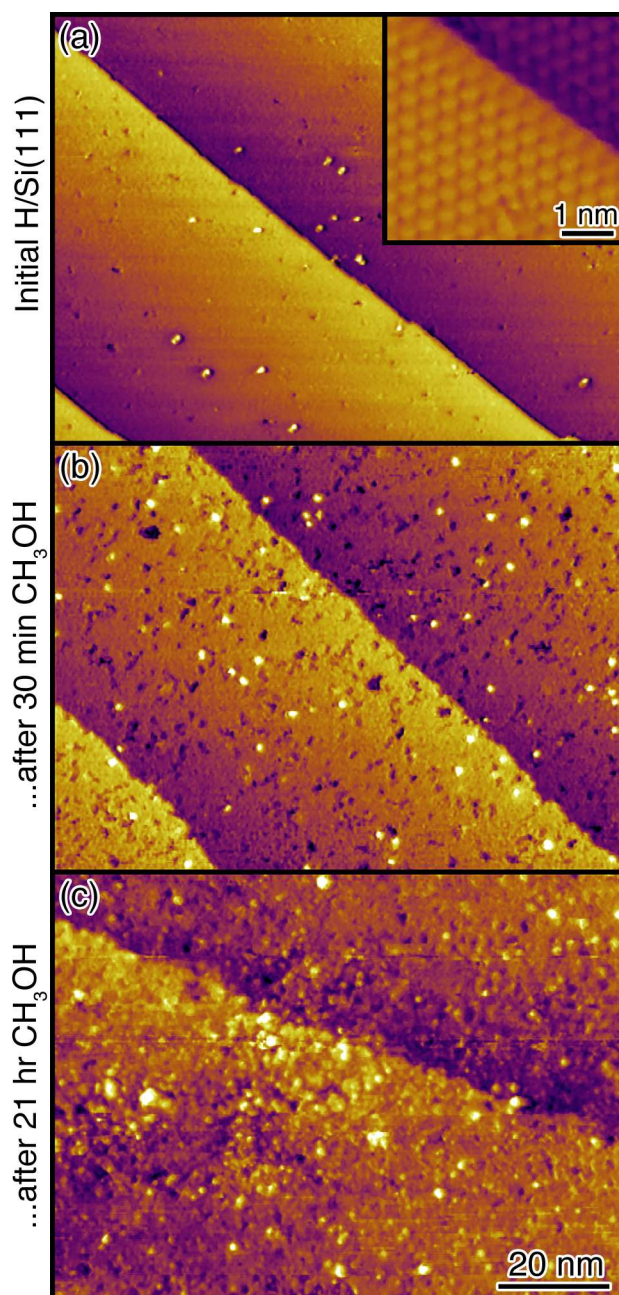
Figure 5.2: (a) STM image of H/Si(111) surface displaying atomically smooth terraces with atomically straight, single-atom-high steps. The inset shows a high-resolution view of the step edge. Images of H/Si(111) surfaces after immersion in methanol at 65°C for (b) 30 min and (c) 21 hr.

Most of the step etching was observed in the first 30 min of reaction with methanol, as can be seen by comparing the surfaces in Figure 5.2(b) and Figure 5.2(c), which were reacted for 30 min and to nominal completion (21 hr), respectively. Few morphological changes were observed after 30 min of reaction. Detailed morphological comparisons were not possible; however, as fully methoxylated surfaces were

difficult to image, and atomic resolution was never obtained. This difficulty is consistent with our DFT simulations (*vide infra*), the expected rapid rotation of the methoxy group at room temperature,[25] and the intuitive expectation that tunneling is hindered by the methoxy group.

Further evidence of methanol-induced etching was obtained from an analysis of the Si–H stretch region of the infrared absorption spectrum of the initial and methoxylated surfaces as shown in Figure 5.3. On surfaces miscut by 9° towards the $\left\langle \overline{1}\,\overline{1}2 \right\rangle$ direction, the NH$_4$F etch used to prepare the H-terminated Si(111) surfaces produces near-atomically straight steps with the dihydride termination sketched in Figure 5.3.[2] As a result, the infrared spectrum displays one transition at 2084 cm^{-1} that is assigned to the terrace mode and three intense step modes at 2094 cm^{-1}, 2101 cm^{-1}, and 2135 cm^{-1} that correspond to the C_1, C_2, and C_3 step vibrations, respectively, which are also sketched in Figure 5.3.[2,54] These four modes were clearly resolved in the initial spectrum. A small shoulder at 2071 cm^{-1} corresponding to the B_1 monohydride step mode[2] was also observed, which was consistent with the etch-induced formation of a low density of monohydride steps on two-dimensional hillocks.[55]

Figure 5.3: The Si–H stretch region of transmission infrared spectra of functionalized, highly miscut surfaces taken with the light incident in the "upstairs" and "downstairs" orientations as sketched at top. The 9° miscut on these surfaces resulted in a high density of initially dihydride-terminated steps. The spectra are presented 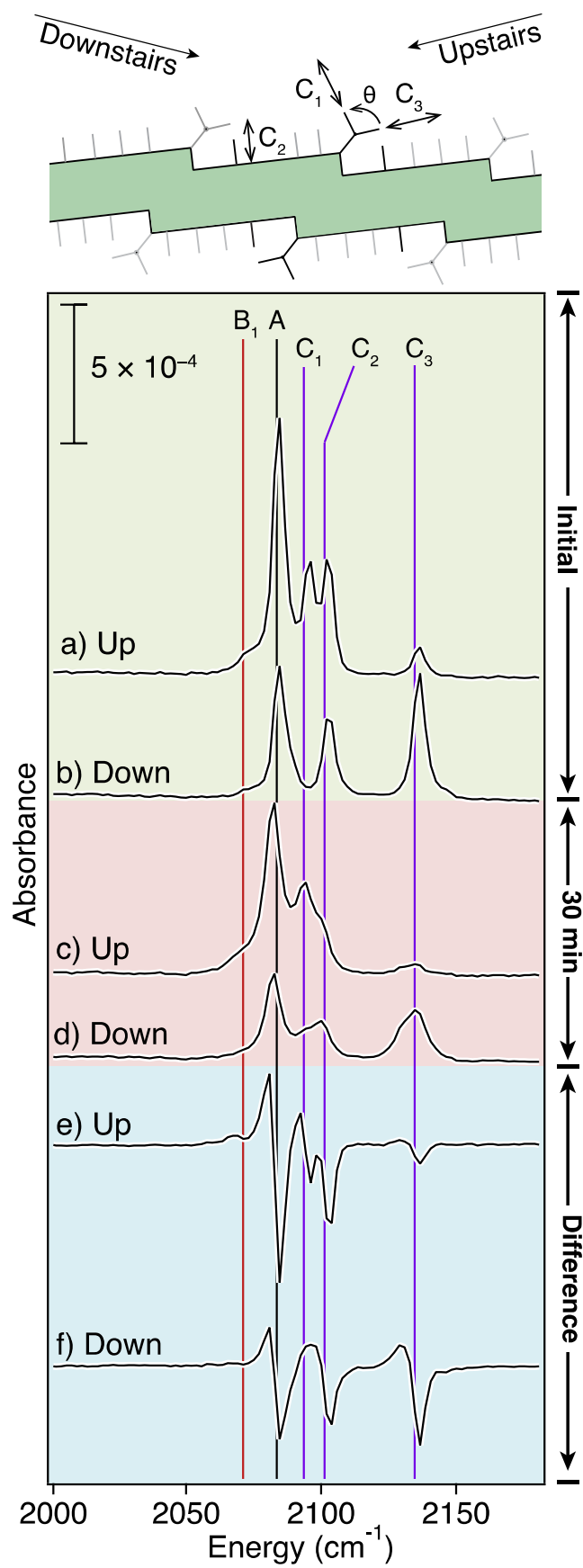in pairs representing (a, b) the initial H-terminated surface, (c, d) the surface after reaction in 65°C methanol for 30 min, and (e, f) the difference spectrum where positive intensity indicates a net increase after methoxylation and negative a net decrease. Vertical lines denote the step and terrace modes listed in Table 5.1.

Name	Energy (cm^{-1})	Description
B_1	2071	Monohydride step vibration
A	2084	Terrace vibration
C_1	2094	Dihydride step vibration[a]
C_2	2101	Dihydride step vibration[a]
C_3	2135	Dihydride step vibration[a]

[a]The dihydride modes are sketched in Figure 3.

Table 5.1: Assignments of the Si–H stretch modes[2] observed on H/Si(111) and denoted by vertical lines in Figure 5.3.

The infrared spectrum was significantly different after 30 min in 65°C methanol, with all modes showing broadening, a small red shift in energy, and a decrease in intensity. The first two effects, line broadening and red shifting, have been studied extensively on flat[56,57] and stepped[58] H/Si(111) and are well known consequences of reduced coverage. The net decrease of intensity across all modes indicates that a reaction has taken place, and is consistent with etching-induced loss of H from both terrace and step sites. Quantification of the relative rates of H loss from step and terrace modes is not possible from these data.

XPS analysis of the chemical state of the methoxylated surfaces was consistent with previous reports. The methoxylation reaction proceeded without concomitant oxidation, as confirmed by high resolution scans of the Si $2p_{3/2}$ transition. Silicon oxidation leads to the appearance of characteristic transitions at binding energies 1-3 eV above the Si^0 transition,[59] so the near-indistinguishability of the Si $2p_{3/2}$ spectra before and after methoxylation, as seen in Figure 5.4, confirmed the absence of oxidation. Methoxylation was confirmed using the C $1s$ transition (Supporting Information).
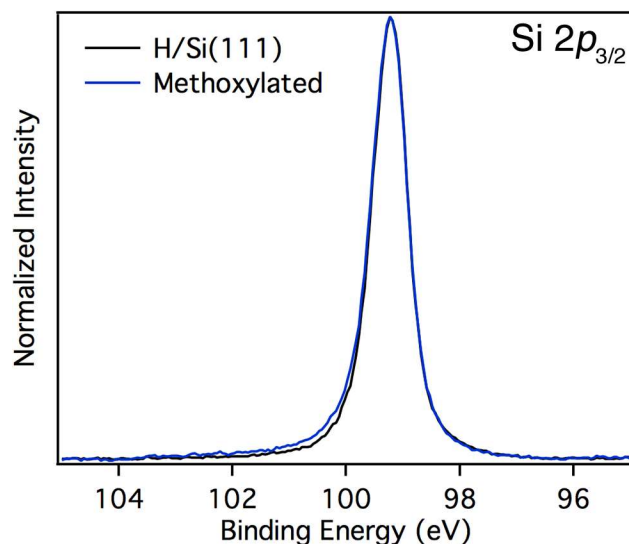
Figure 5.4: The Si *2p*~3/2~ region of XPS spectra of the H/Si(111) surface before and after 21 hr reaction in 65°C methanol. The Si $2p_{1/2}$ component was removed computationally[59] for clarity.

Direct Fluorination of H/Si(111) with HF. Directly immersing H-terminated Si(111) in deoxygenated HF (aq) led to significant surface fluorination, as confirmed both spectroscopically and microscopically. Fluorine was undetectable on the initial H/Si(111) surface, as shown by XPS analysis of the F 1*s* transition in Figure 5.5. Quantitative analysis of the F 1*s* transition (Supporting Information) showed that a 3 min immersion in HF produced a 6.8% monolayer (ML) fluorine coverage, whereas a 15 min immersion produced a 11% ML coverage.
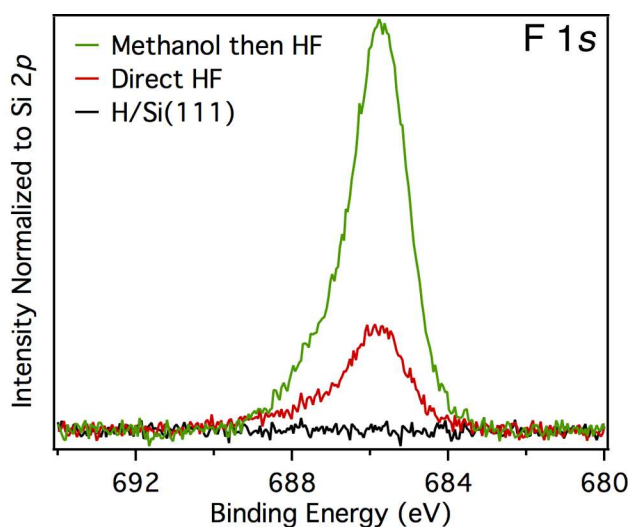
Figure 5.5: The F 1*s* region of XPS spectra of the H/Si(111) surface (black) before reaction, (red) after immersion in HF for 3 min, and (green) after 22 hr methoxylation and subsequent immersion in HF for 3 min. The intensities are normalized to the integrated intensity of the Si *2p* transition.

STM images of H/Si(111) surfaces after immersion in HF show that F atoms directly replaced H atoms with no concomitant etching, as shown by Figure 5.6. After fluorination, the surface was decorated by an apparently random distribution of "dark" or "depressed" sites. These sites typically imaged as depressions in both empty- and filled-state images, but occasionally imaged as protrusions in filled-state images depending on the tip condition. To confirm that these sites corresponded to individual F atoms, a directly fluorinated surface was analyzed with both STM and XPS. The STM analysis found that 5.8% of the sites were dark, in good agreement with XPS analysis of the F 1*s* transition which yielded a F density of 6.8% ML. The good agreement between the two strongly suggested that the dark sites were individual F atoms.

Direct HF
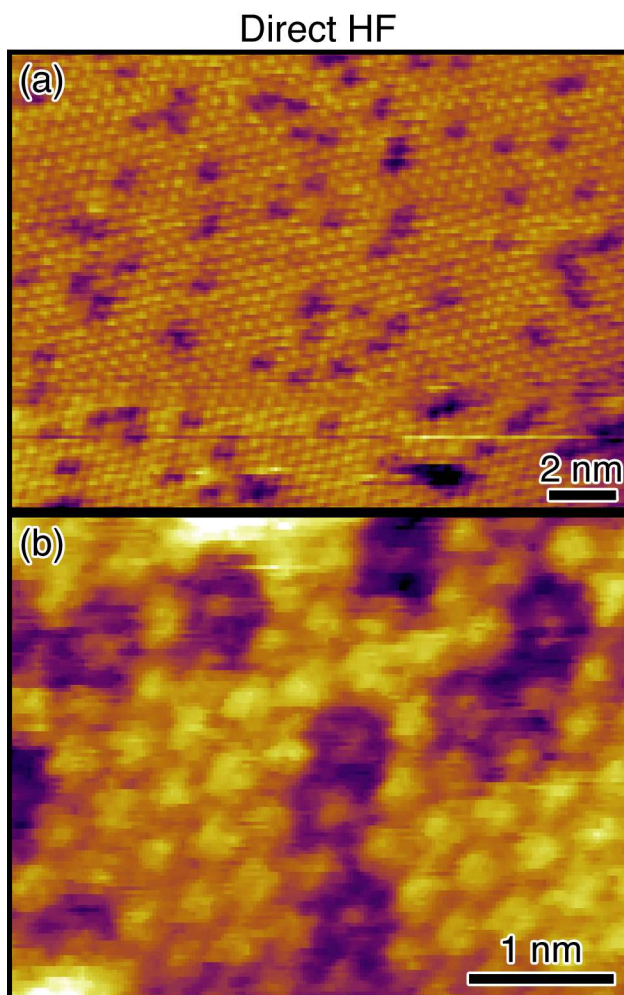
Figure 5.6: STM images of a H/Si(111) surface after immersion in HF (aq) for 3 min. The bright sites are individual H atoms, whereas the dark sites are individual F atoms.

Fluorination of CH₃O/Si(111) with HF. Immersing a methoxy-terminated Si(111) surface in deoxygenated HF (aq) for 3 min removed all traces of the methoxy-termination while partially fluorinating the surface. After methoxylation and HF immersion, XPS analysis of the F $1s$ transition, shown in Figure 5.5, yielded a 24% ML F coverage (Supporting Information). This coverage is approximately 70% of that expected for the nanopattern in Figure 5.1. Analysis of the C $1s$ and O $1s$ regions (Supporting Information) confirmed complete removal of the methoxy groups.

STM images of methoxylated surfaces after fluorination in HF, such as those in Figure 5.7, showed no evidence of the proposed nanopattern,[25] but instead bore similarities to images of the methoxylated surface. The images were characterized by three distinct terrace features. First, the majority of the sites

were "bright," which we attributed to H termination in analogy to Figure 5.6. Second, many deep, fissure-like regions were observed. Tip convolution effects prevented definitive depth measurements on the narrowest fissures; however, wider fissures were confirmed to be 1 ML in depth. The fissures were therefore attributed to meandering etch pits. Finally, Figure 5.7(b) shows that some terrace sites imaged darker than the majority species but significantly lighter than the monolayer-deep etch pits. These features were assigned to individual F atoms in analogy to Figure 5.6. Importantly, both isolated and adjacent F atoms were observed, as seen in Figure 5.7(b), which did not support the proposed nanopatterning mechanism. A nanopatterned surface would display isolated functionalized sites surrounded by six H atoms as shown in Figure 5.1. In addition to the terrace features, the step edges showed clear evidence of etching and were similar to those observed after methoxylation, as seen in Figure 5.2(b) and Figure 5.2(c).
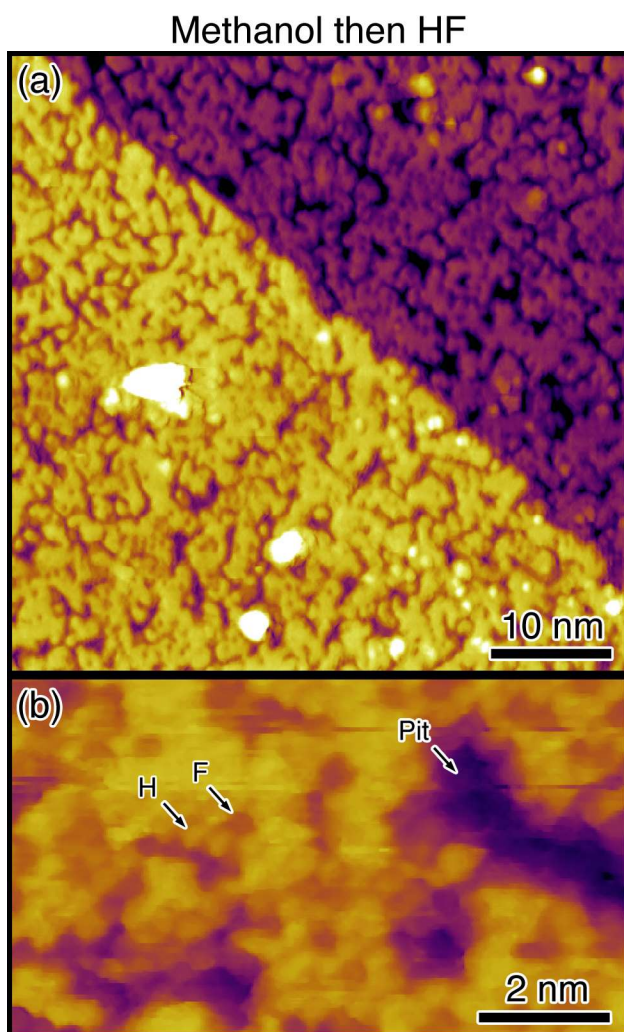
Methanol then HF

Figure 5.7: STM images of methoxylated Si(111) surfaces after immersion in HF (aq) for 3 min. Three features are observed: bright H-terminated sites, darker F-terminated sites, and irregular monolayer deep etch pits.

KMC Model of H/Si(111) Methoxylation. STM images of the methoxylated H/Si(111) surface before and after fluorination displayed two characteristic but puzzling morphological features: unstructured meandering pits and step edges that were relatively straight on the tens-of-nm length scale but jagged at the atomic length scale. These features are not characteristic of simple etching reactions. Within a step-terrace-kink model, atomically straight steps are the hallmark of highly site-specific surface etching (*i.e.,* high kink site reactivity), whereas compact (not meandering!) unstructured pits are characteristic of isotropic step-kink reactivity.[40, 60] However, two additional effects complicate this reaction. First, the initial H/Si(111) surface had atomically straight steps, so the final morphology may have been influenced by the starting morphology. Second, the morphological effects of the etching reaction may have been influenced by the methoxylation reaction.

To understand the origins of these morphological features and their mechanistic implications, we performed kinetic Monte Carlo simulations. These simulations were based on three observations. First, the experimental data could only be explained by parallel etching and methoxylation reactions, so both were included in the simulation. Second, the most dramatic morphological changes, particularly at the step edges, occurred in the early stages of the reaction (~first 30 min). Little evolution was observed after a few hours of reaction, and etching appeared to stop. Third, a wide variety of etchants, including NH_4F,[3] KOH,[61,62] H_2O,[18,19] and isopropanol,[39] have been shown to attack H/Si(111) surfaces anisotropically following the general pattern of kink sites being orders of magnitude more reactive than step sites which are in turn orders of magnitude more reactive than terrace sites.

The KMC simulations were based on three assumptions that are consistent with these observations. First, the etching reaction was assumed to be highly anisotropic. For concreteness, we used the site-specific etch rates appropriate for the best studied H/Si(111) etching reaction, NH_4F etching in air.[3] Second, the methoxylation reaction was assumed to attack random sites on the surface, not a particular type of site. This assumption is consistent with the randomly distributed dark sites in Figure 5.2(b). Finally, a

methoxylated site was assumed to be unreactive; it would neither etch nor de-methoxylate. This assumption stopped morphological evolution once all sites were methoxylated.

The KMC simulations had a single adjustable parameter, the relative rate of methoxylation, which determined the final morphology. If the rate of methoxylation was zero (see Supporting Information), the simulation would etch forever, yielding a morphology characterized by straight steps and triangular etch pits. If the rate of methoxylation was finite, the surface would etch until all sites were methoxylated, then the reaction would stop. Depending on the relative rates of etching and methoxylation, a range of morphologies were observed as shown by Figure 5.8. When the rate of methoxylation was much faster than the etch rate — the fast methoxylation limit — the surface would become fully methoxylated with little to no etching. As a result, the final morphology was quite similar to the initial morphology. When the rate of methoxylation was slow compared to the etch rate — the slow methoxylation limit — the surface would etch extensively before the reaction would stop. Importantly, the randomly distributed methoxylated sites blocked the highly anisotropic etching reaction. In doing so, the random blocking prevented the highly anisotropic etching reaction from producing straight steps and triangular etch pits. Instead, etching produced a very rough morphology as seen in Figure 5.8.
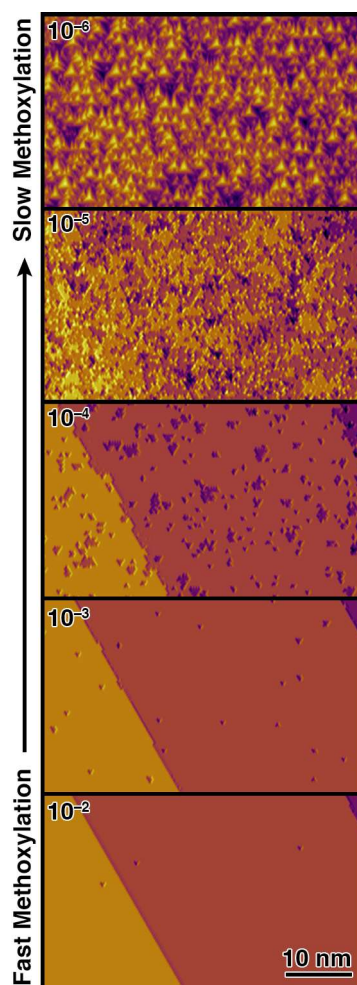
Figure 5.8: The range of final morphologies produced by KMC simulations of parallel etching and methoxylation reactions. The ratio of the rates of methoxylation to kink site etching ranged from 10^{-6} (slow methoxylation) to 10^{-2} (fast methoxylation) as indicated in the upper left of each image. All of the surfaces are fully methoxylated.

The best match between the experimentally observed morphologies, such as Figure 5.7, and this simple model is shown in Figure 5.9. In this intermediate regime, the overall rate of methoxylation was comparable to the overall rate of etching, and the morphology shows clear evidence of both reactions. The atomically straight steps on the initial morphology resulted in steps that were nominally straight on the tens-of-nm length scale, but rough on the atomic scale. Similarly, the meandering, unstructured nature of the etch pits was a result of site blocking by the methoxylation reaction.
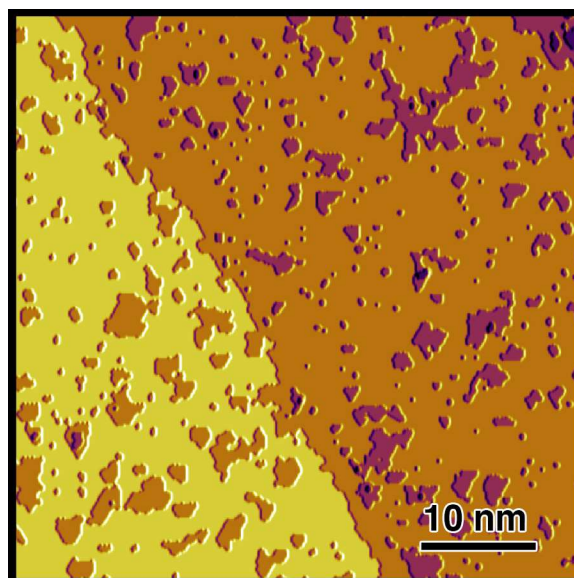
Figure 5.9: Best match KMC simulation to experimental images of methoxylated surface after fluorination. See Supporting Information for details.

DFT Simulations of STM Images. The high degree of correlation between the density of atomic-scale "depressions" in images of fluorinated H/Si(111) and the F coverage calculated from x-ray photoemission spectra suggested that the dark features were individual fluorine atoms. To confirm this assignment, we simulated STM images of isolated fluorine atoms on H/Si(111), such as the one shown in Figure 5.10. The good agreement between simulation and experiment confirmed this assignment.
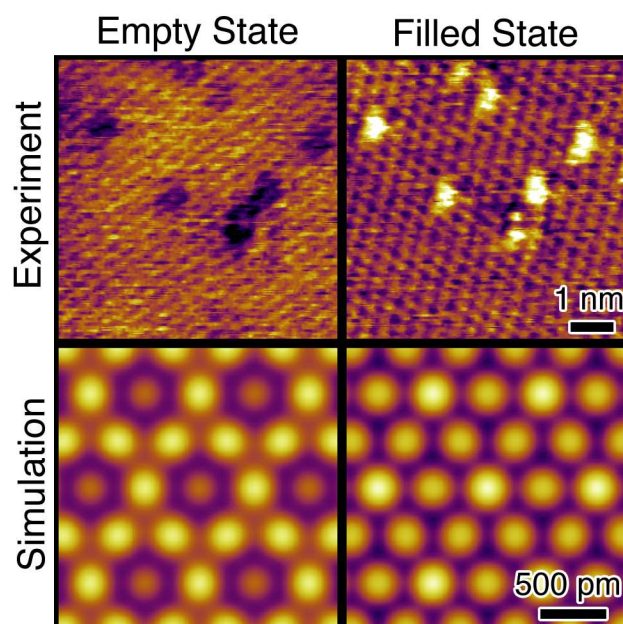
Figure 5.10: Comparison of experimental and simulated empty- and filled-state STM images of isolated F atoms on a H/Si(111) surface. The F sites typically imaged as depressions in both empty- and filled-state images, but occasionally (as shown here) imaged as protrusions in filled-state images depending on the tip condition.

In contrast to the case of adsorbed F, simulations of isolated methoxy groups on H/Si(111) predicted much lower tunneling currents at comparable tip-surface distances. This low conductance explained our inability to obtain high resolution images of the methoxylated surface.

5.5 Discussion

Implications for Si Functionalization. These experiments investigated two promising strategies for the fluorination of Si(111): a 15 min single-step reaction that produced atomically flat surfaces with 11% fluorination and a ~20 hr, two-step reaction that produced rougher surfaces with 24% fluorination. The experimental results are summarized in Figure 5.11. As demonstrated by Michalak *et al.,*[25] replacement of the F atoms by hydroxyl groups without concomitant oxidation can be achieved through a brief immersion in H_2O.
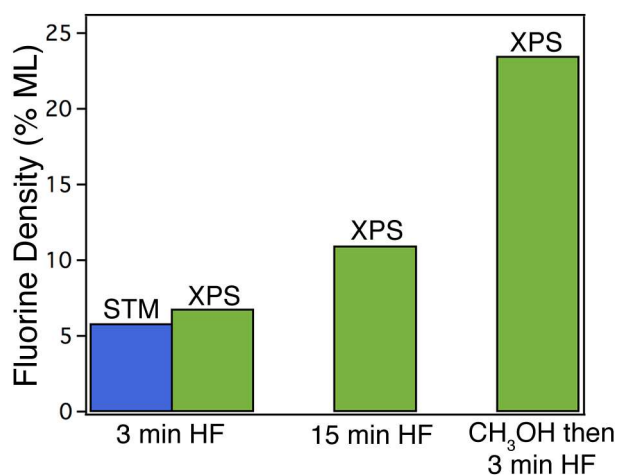
Figure 5.11: The F atom density produced by different fluorination strategies.

From the standpoint of Si functionalization, the direct fluorination reaction bears further investigation. Although this approach will produce fewer attachment points for subsequent functionalization reactions, the atomically smooth morphology may offset this disadvantage by improving the homogeneity of any grown films and suppressing the formation of electronic defects.[63]

Reaction of CH₃OH with Si(111). These experiments and simulations, taken together, show that methanol reacts with H/Si(111) surfaces through two parallel mechanisms: an etching reaction and a methoxylation reaction. STM images of the methoxylated surface before and after fluorination provide incontrovertible evidence of etching. Two additional pieces of evidence suggest that the etching reaction is highly anisotropic, occurring much more rapidly at step sites than at terrace sites. First, STM images show a dramatic roughening of the surface steps after only 30 min of reaction. Second, kinetic Monte Carlo simulations of parallel etching and methoxylation produce morphologies that are in good agreement with STM experiments.

The fissured morphologies produced by the methanol reaction suggest that methoxylation of a silicon site blocks (or drastically slows) subsequent etching of that site. In other words, methoxylation frustrates etching. This hypothesis is supported by three pieces of evidence. First, step edge morphologies undergo significant changes during the first 30 min of reaction but then show little further evolution, suggesting that the step edges are rapidly passivated. Second, the "fissured" appearance of the etch pits is not consistent with a simple etching reaction; site blocking reactions are needed to produce these morphologies. Finally, a continuous etching reaction would lead to very rough surfaces after extended reaction, which was not observed.

In hindsight, slow etching of silicon by warm methanol is not surprising. Warm H_2O is a slow but highly anisotropic Si(111) etchant that produces flat H/Si(111) much like NH_4F (aq).[18–21] The initial step in this reaction is thought to be attack by OH^- produced by the autodissociation of H_2O. Methanol and H_2O are both weak acids with similar dissociation constants, so etching may be initiated by the methoxide ion, OCH_3^-, which is produced by autodissociation of CH_3OH. A similar reaction scheme has previously been proposed for the reaction of isopropoxide with H/Si(111) in isopropanol solutions.[39]

Despite intensive effort over a period of one year and a demonstrated ability to image H and F atoms with atomic resolution, we observed no evidence of the proposed hexagonal nanopattern.[25] The original evidence for nanopatterning was the apparent preponderance of H atoms with three nearest neighbors as

estimated from blue shifts in the Si–H stretch vibration; however, this argument assumed that the initial atomically flat morphology was preserved during subsequent reactions. These experiments show that this is not the case, and the actual morphology is much more complicated.

Direct Fluorination of H/Si(111) with HF. The mechanism of the direct fluorination of H/Si(111) by HF is not known. STM images suggest the reaction does not proceed through an etching mechanism, as the fluorinated surfaces display atomically straight steps and an apparently random distribution of F atoms. If HF were etching H/Si(111) and producing a mixture of H- and F-terminated sites, then STM images of the fluorinated surface taken before complete reaction (*i.e.,* before one monolayer of etching) would show no fluorination at the upper step edge but full fluorination at the lower edge. (This effect is clearly seen in the production of "denuded zones" in Br_2 (g) etching of Si(111).[64]) This was not observed.

The protons on H/Si(111) are not labile, so direct fluorination is unlikely to proceed by an autoionization mechanism. For example, deuterium exchange is not observed when H/Si(111) surfaces are immersed in D_2O. Instead, deuteration proceeds through an etching mechanism.[65]

Based on these data, we cannot rule out a photoinduced reaction. The mechanism of direct fluorination deserves further study.

5.6 Conclusions

Two promising strategies for the fluorination of H/Si(111) were examined: a 15 min single-step reaction that produced atomically flat surfaces with 11% fluorination and a ~20 hr, two-step reaction that produced atomically rough, fissured surfaces with 24% fluorination. The atomic-scale roughness observed after the two-step strategy was attributed to the initial methoxylation reaction. Methanol was shown to react with H/Si(111) surfaces through two parallel mechanisms: an etching reaction and a methoxylation reaction. The methoxylation reaction locally inhibited or "frustrated" the etching reaction, leading to the development of a characteristic fissured morphology. No evidence of the previously proposed nanopatterning mechanism was observed.

Author Information

Corresponding Author

Melissa.Hines@cornell.edu, +1-607-255-3040

Notes

The authors declare no competing financial interest.

Supporting Information Available: Text describing the XPS analysis, KMC simulations, and the STM image simulations. This material is available free of change on the Internet at http://pubs.acs.org.

References

[1] Higashi, G. S.; Chabal, Y. J.; Trucks, G. W.; Raghavachari, K. Ideal Hydrogen Termination of the Si(111) Surface. *Appl. Phys. Lett.* **1990**, *56*, 656-658.

[2] Jakob, P.; Chabal, Y. J. Chemical Etching of Vicinal Si(111): Dependence of the Surface Structure and the Hydrogen Termination on the *p*H of the Etching Solutions. *J. Chem. Phys.* **1991**, *95*, 2897-2909.

[3] Hines, M. A. In Search of Perfection: Understanding the Highly Defect-Selective Chemistry of Anisotropic Etching. *Annu. Rev. Phys. Chem.* **2003**, *54*, 29-56.

[4] Linford, M. R.; Chidsey, C. E. D. Alkyl Monolayers Covalently Bonded to Silicon Surfaces. *J. Am. Chem. Soc.* **1993**, *115*, 12631-12632.

[5] Linford, M. R.; Fenter, P.; Eisenberger, P. M.; Chidsey, C. E. D. Alkyl Monolayers on Silicon Prepared From 1-Alkenes and Hydrogen-Terminated Silicon. *J. Am. Chem. Soc.* **1995**, *117*, 3145-3155.

[6] Boukherroub, R.; Morin, S.; Bensebaa, F.; Wayner, D. D. M. New Synthetic Routes to Alkyl Monolayers on the Si(111) Surface. *Langmuir* **1999**, *15*, 3831-3835.

[7] Cicero, R. L.; Chidsey, C. E. D.; Lopinski, G. P.; Wayner, D. D. M.; Wolkow, R. A. 1-Olefin Additions on H−Si(111): Evidence for a Surface Chain Reaction Initiated At Isolated Dangling Bonds. *Langmuir* **2002**, *18*, 305-307.

[8] Eves, B. J.; Sun, Q.-Y.; Lopinski, G. P.; Zuilhof, H. Photochemical Attachment of Organic Monolayers on H-Terminated Si(111): Radical Chain Propagation Observed Via STM Studies. *J. Am. Chem. Soc.* **2004**, *126*, 14318-14319.

[9] Colavita, P. E.; Sun, B.; Tse, K.-Y.; Hamers, R. J. Photochemical Grafting of *n*-Alkenes Onto Carbon Surfaces: The Role of Photoelectron Ejection. *J. Am. Chem. Soc.* **2007**, *129*, 13554-13565.

[10] Wang, X.; Ruther, R. E.; Streifer, J. A.; Hamers, R. J. UV-Induced Grafting of Alkenes to Silicon Surfaces: Photoemission Versus Excitons. *J. Am. Chem. Soc.* **2010**, *132*, 4048-4049.

[11] Bansal, A.; Li, X.; Lauermann, I.; Lewis, N. S.; Yi, S. I.; Weinberg, W. H. Alkylation of Si Surfaces Using a Two-Step Halogenation/Grignard Route. *J. Am. Chem. Soc.* **1996**, *118*, 7225-7226.

[12] Royea, W. J.; Juang, A.; Lewis, N. S. Preparation of Air-Stable, Low Recombination Velocity Si(111) Surfaces Through Alkyl Termination. *Appl. Phys. Lett.* **2000**, *77*, 1988-1990.

[13] Webb, L. J.; Lewis, N. S. Comparison of the Electrical Properties and Chemical Stability of Crystalline Silicon(111) Surfaces Alkylated Using Grignard Reagents or Olefins With Lewis Acid Catalysts. *J. Phys. Chem. B* **2003**, *107*, 5404-5412.

[14] Yu, H.; Webb, L. J.; Ries, R. S.; Solares, S. D.; Goddard, III, William A.; Heath, J. R.; Lewis, N. S. Low-Temperature STM Images of Methyl-Terminated Si(111) Surfaces. *J. Phys. Chem. B* **2005**, *109*, 671-674.

[15] Yu, H.; Webb, L. J.; Heath, J. R.; Lewis, N. S. Scanning Tunneling Spectroscopy of Methyl- and Ethyl-Terminated Si(111) Surfaces. *Appl. Phys. Lett.* **2006**, *88*, 25211-25211.

[16] Li, Y.; Calder, S.; Yaffe, O.; Cahen, D.; Haick, H.; Kronik, L.; Zuilhof, H. Hybrids of Organic Molecules and Flat, Oxide-Free Silicon: High-Density Monolayers, Electronic Properties, and Functionalization. *Langmuir*. **2012**, *28*, 9920-9929.

[17] Wong, K. T.; Lewis, N. S. What a Difference a Bond Makes: The Structural, Chemical, and Physical Properties of Methyl-Terminated Si(111) Surfaces. *Acc. Chem Res.* **2014**, *47*, 3037-3044.

[18] Watanabe, S.; Shigeno, M.; Nakayama, N.; Ito, T. Silicon-Monohydride Termination of Silicon-111 Surface Formed By Boiling Water. *Jpn. J. Appl. Phys.* **1991**, *30*, 3575-3579.

[19] Watanabe, S.; Sugita, Y. The Role of Dissolved Oxygen in Hot Water During Dissolving Oxides and Terminating Silicon Surfaces With Hydrogen. *Surf. Sci.* **1995**, *327*, 1-8.

[20] Faggin, M. F.; Green, S. K.; Clark, I. T.; Queeney, K. T.; Hines, M. A. Production of Highly Homogeneous Si(100) Surfaces By H_2O Etching: Surface Morphology and the Role of Strain. *J. Am. Chem. Soc.* **2006**, *128*, 11455-11462.

[21] Skibinski, E. S.; Hines, M. A. Molecular Mechanism of Etching-Induced Faceting on Si(100): Micromasking is Not a Prerequisite for Pyramidal Texturing. *J. Phys. Chem. C* **2015**, *119*, 14490-14498.

[22] Pietsch, G. J.; Chabal, Y. J.; Higashi, G. S. Infrared-Absorption Spectroscopy of Si(100) and Si(111) Surfaces After Chemomechanical Polishing. *J. Appl. Phys.* **1995**, *78*, 1650-1658.

[23] Allongue, P. Molecular Imaging and Local Density of States Characterization At the Si(111)/NaOH Interface. *Phys. Rev. Lett.* **1996**, *77*, 1986-1989.

[24] Chabal, Y. J.; Higashi, G. S.; Small, R. J. Surface Chemical Composition and Morphology. **2008**, *Handbook of Semiconductor Wafer Cleaning Technology*, 523-618.

[25] Michalak, D. J.; Amy, S. R.; Aureau, D.; Dai, M.; Estéve, A.; Chabal, Y. J. Nanopatterning Si(111) Surfaces as a Selective Surface-Chemistry Route. *Nature Materials* **2010**, *9*, 266-271.

[26] Michalak, D. J.; Rivillon, S.; Chabal, Y. J.; Estéve, A.; Lewis, N. S. Infrared Spectroscopic Investigation of the Reaction of Hydrogen-Terminated, (111)-Oriented Silicon Surfaces With Liquid Methanol. *J. Phys. Chem. B* **2006**, *110*, 20426-20434.

[27] Michalak, D. J.; Amy, S. R.; Estéve, A.; Chabal, Y. J. Investigation of the Chemical Purity of Silicon Surfaces Reacted With Liquid Methanol. *J. Phys. Chem. C* **2008**, *112*, 11907-11919.

[28] The term "quantized" was also set in quotes in Ref. 25.

[29] Lucovsky, G. Relation of Si-H Vibrational Frequencies to Surface Bonding Geometry. *J. Vac. Sci. Technol.* **1979**, *16*, 1225-1228.

[30] Zhang, X.; Chabal, Y. J.; Christman, S. B.; Chaban, E. E.; Garfunkel, E. Oxidation of H-Covered Flat and Vicinal Si(111)-1 × 1 Surfaces. *J. Vac. Sci. Technol. A* **2001**, *19*, 1725-1729.

[31] Estève, A.; Chabal, Y. J.; Raghavachari, K.; Weldon, M. K.; Queeney, K. T.; Rouhani, M. D. Water-Saturated Si(100)-(2 × 1): Kinetic Monte Carlo Simulations of Thermal Oxygen Incorporation. *J. Appl. Phys.* **2001**, *90*, 6000-6005.

[32] Ferguson, G. A.; Rivillon, S.; Chabal, Y.; Raghavachari, K. The Structure and Vibrational Spectrum of the Si(111)-H/Cl Surface. *J. Phys. Chem. C* **2009**, *113*, 21713-21720.

[33] Kern, W.; Puotinen, D. A. Cleaning Solutions Based on Hydrogen Peroxide for Use in Silicon Semiconductor Technology. *RCA Rev.* **1970**, *31*, 187-206.

[34] Wade, C. P.; Chidsey, C. E. D. Etch-Pit Initiation By Dissolved Oxygen on Terraces of H-Si(111). *Appl. Phys. Lett.* **1997**, *71*, 1879-1881.

[35] Garcia, S. P.; Bao, H.; Hines, M. A. Understanding the *p*H Dependence of Silicon Etching: The Importance of Dissolved Oxygen in Buffered HF Etchants. *Surf. Sci.* **2003**, *541*, 252-261.

[36] Greiner, M.; Kruse, P. Recrystallization of Tungsten Wire for Fabrication of Sharp and Stable Nanoprobe and Field-Emitter Tips. *Rev. Sci. Instrum.* **2007**, *78*, 026104.

[37] Schmucker, S. W.; Kumar, N.; Abelson, J. R.; Daly, S. R.; Girolami, G. S.; Bischof, M. R.; Jaeger, D. L.; Reidy, R. F.; Gorman, B. P.; Alexander, J.; *et al*. Field-Directed Sputter Sharpening for Tailored Probe Materials and Atomic-Scale Lithography. *Nat. Commun.* **2012**, *3*, 1-8.

[38] Flidr, J.; Huang, Y.-C.; Newton, T. A.; Hines, M. A. Extracting Site-Specific Reaction Rates From Steady State Surface Morphologies: Kinetic Monte Carlo Simulations of Aqueous Si(111) Etching. *J. Chem. Phys.* **1998**, *108*, 5542-5553.

[39] Newton, T. A.; Huang, Y.-C.; Lepak, L. A.; Hines, M. A. The Site-Specific Reactivity of Isopropanol in Aqueous Silicon Etching: Controlling Morphology With Surface Chemistry. *J. Chem. Phys.* **1999**, *111*, 9125-9128.

[40] Hines, M. A. The Picture Tells the Story: Using Surface Morphology to Probe Chemical Etching Reactions. *Int. Reviews in Phys. Chem.* **2001**, *20*, 645-672.

[41] Skibinski, E. S.; Hines, M. A. Finding Needles in Haystacks: Scanning Tunneling Microscopy Reveals the Complex Reactivity of Si(100) Surfaces. *Acc. Chem. Res.* **2015**, *48*, 2159-2166.

[42] Kohn, W.; Sham, L. J. Self-Consistent Equations Including Exchange and Correlation Effects. *Phys. Rev.* **1965**, *140*, A1133-A1138.

[43] Perdew, J. P.; Burke, K.; Ernzerhof, M. Generalized Gradient Approximation Made Simple. *Phys. Rev. Lett.* **1996**, *77*, 3865-3868.

[44] Kresse, G.; Hafner, J. *Ab Initio* Molecular Dynamics for Liquid Metals. *Phys. Rev. B* **1993**, *47*, 558-561.

[45] Kresse, G.; Hafner, J. *Ab Initio* Molecular-Dynamics Simulation of the Liquid-Metal-Amorphous-Semiconductor Transition in Germanium. *Phys. Rev. B* **1994**, *49*, 14251-14269.

[46] Kresse, G.; Furthmüller, J. Efficiency of *Ab-Initio* Total Energy Calculations for Metals and Semiconductors Using a Plane-Wave Basis Set. *Comput. Mat. Sci.* **1996**, *6*, 15-50.

[47] Kresse, G.; Furthmüller, J. Efficient Iterative Schemes for *Ab Initio* Total-Energy Calculations Using a Plane-Wave Basis Set. *Phys. Rev. B* **1996**, *54*, 11169-11186.

[48] Blöchl, P. E. Projector Augmented-Wave Method. *Phys. Rev. B* **1994**, *50*, 17953-17979.

[49] Kresse, G.; Joubert, D. From Ultrasoft Pseudopotentials to the Projector Augmented-Wave Method. *Phys. Rev. B* **1999**, *59*, 1758-1775.

[50] Blöchl, P. E.; Jepsen, O.; Andersen, O. K. Improved Tetrahedron Method for Brillouin-Zone Integrations. *Phys. Rev. B* **1994**, *49*, 16223-16233.

[51] Tersoff, J.; Hamann, D. R. Theory of the Scanning Tunneling Microscope. *Phys. Rev. B* **1985**, *31*, 805-813.

[52] Hofer, W. A.; Redinger, J. Scanning Tunneling Microscopy of Binary Alloys: First Principles Calculation of the Current for Pt*X* (100) Surfaces. *Surf. Sci.* **2000**, *447*, 51-61.

[53] Hofer, W. A. Challenges and Errors: Interpreting High Resolution Images in Scanning Tunneling Microscopy. *Prog. Surf. Sci.* **2003**, *71*, 147-183.

[54] Hines, M. A.; Chabal, Y. J.; Harris, T. D.; Harris, A. L. Measuring the Structure of Etched Silicon Surfaces With Raman Spectroscopy. *J. Chem. Phys.* **1994**, *101*, 8055-8072.

[55] Flidr, J.; Huang, Y.-C.; Hines, M. A. An Atomistic Mechanism for the Production of Two- and Three-Dimensional Etch Hillocks on Si(111) Surfaces. *J. Chem. Phys.* **1999**, *111*, 6970-6981.

[56] Jakob, P.; Chabal, Y. J.; Raghavachari, K. Lineshape Analysis of the Si–h Stretching Mode of the Ideally H-Terminated Si(111) Surface: The Role of Dynamical Dipole Coupling. *Chem. Phys. Lett.* **1991**, *187*, 325-333.

[57] Newton, T. A.; Boiani, J. A.; Hines, M. A. The Correlation Between Surface Morphology and Spectral Lineshape: A Re-Examination of the H-Si(111) Stretch Vibration. *Surf. Sci.* **1999**, *430*, 67-79.

[58] Jakob, P.; Chabal, Y. J.; Raghavachari, K.; Christman, S. B. Discrete Nature of Inhomogeneity on Stepped H/Si(111) Surfaces: Spectroscopic Identification of Individual Terrace Sizes. *Phys. Rev. B* **1993**, *47*, 6839-6842.

[59] Himpsel, F. J.; McFeely, F. R.; Taleb-Ibrahimi, A.; Yarmoff, J. A. Microscopic Structure of the SiO_2/Si Interface. *Phys. Rev. B* **1988**, *38*, 6084-6096.

[60] Song, A.; Jing, D.; Hines, M. A. Rutile Surface Reactivity Provides Insight Into the Structure-Directing Role of Peroxide in TiO_2 Polymorph Control. *J. Phys. Chem. C* **2014**, *118*, 27343-27352.

[61] Wind, R. A.; Hines, M. A. Macroscopic Etch Anisotropies and Microscopic Reaction Mechanisms: A Micromachined Structure for the Rapid Assay of Etchant Anisotropy. *Surf. Sci.* **2000**, *460*, 21-38.

[62] Garcia, S. P.; Bao, H.; Hines, M. A. Etchant Anisotropy Controls the Step Bunching Instability in KOH Etching of Silicon. *Phys. Rev. Lett.* **2004**, *93*, 166102.

[63] Peng, W.; DeBenedetti, W. J. I.; Kim, S.; Hines, M. A.; Chabal, Y. J. Lowering the Density of Electronic Defects on Organic-Functionalized Si(100) Surfaces. *Appl. Phys. Lett.* **2014**, *104*, 241601.

[64] Pechman, R. J.; Wang, X.-S.; Weaver, J. H. Interactions of Br With Si(111)-7 × 7: Chemisorption, Step Retreat, and Terrace Etching. *Phys. Rev. B* **1995**, *52*, 11412-11423.

[65] Luo, H.; Chidsey, C. E. D. D-Si(111)(1 × 1) Surface for the Study of Silicon Etching in Aqueous Solutions. *Appl. Phys. Lett.* **1998**, *72*, 477-479.